

INFORMATION TO USERS

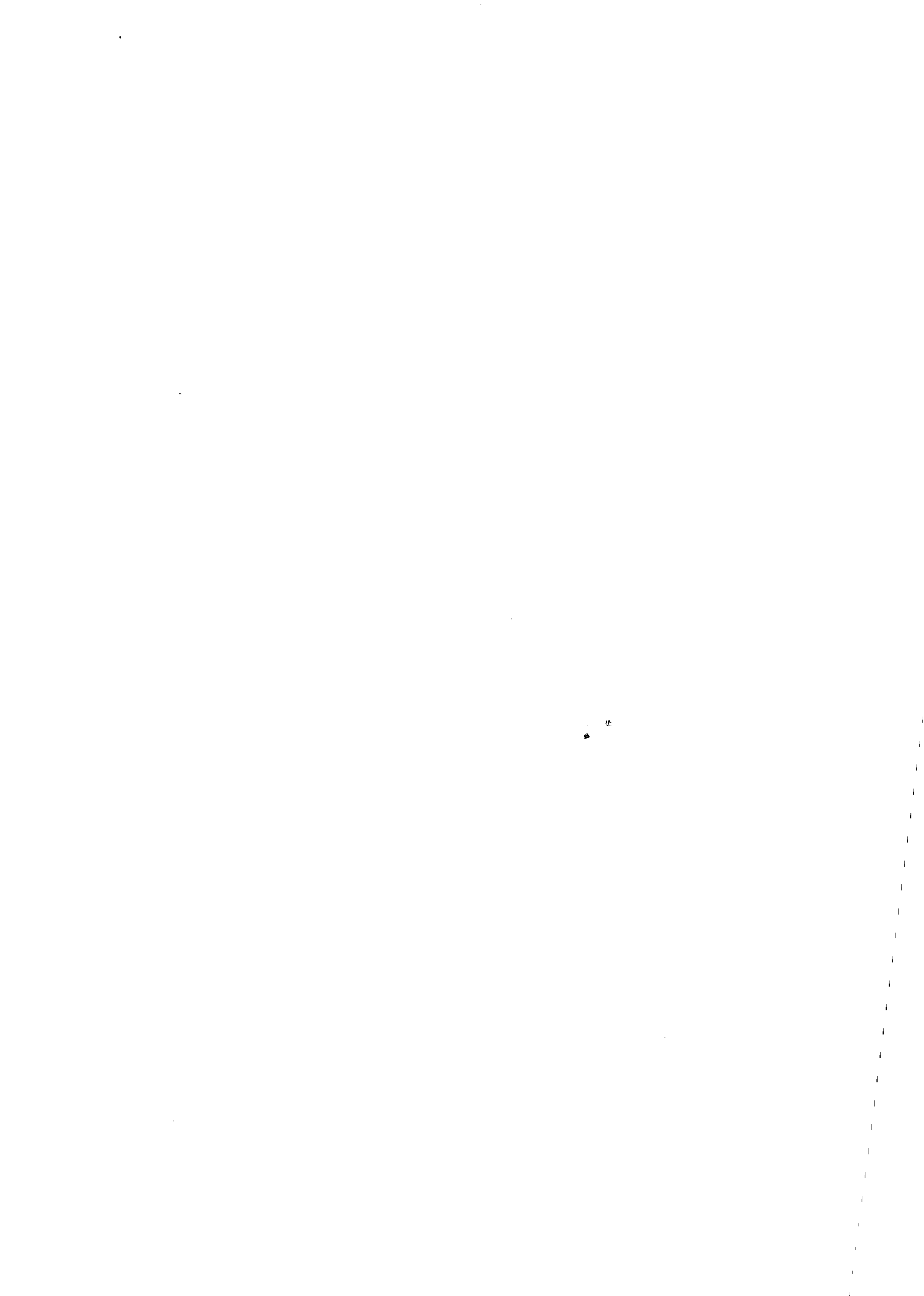
This was produced from a copy of a document sent to us for microfilming. While the most advanced technological means to photograph and reproduce this document have been used, the quality is heavily dependent upon the quality of the material submitted.

The following explanation of techniques is provided to help you understand markings or notations which may appear on this reproduction.

1. The sign or "target" for pages apparently lacking from the document photographed is "Missing Page(s)". If it was possible to obtain the missing page(s) or section, they are spliced into the film along with adjacent pages. This may have necessitated cutting through an image and duplicating adjacent pages to assure you of complete continuity.
2. When an image on the film is obliterated with a round black mark it is an indication that the film inspector noticed either blurred copy because of movement during exposure, or duplicate copy. Unless we meant to delete copyrighted materials that should not have been filmed, you will find a good image of the page in the adjacent frame. If copyrighted materials were deleted you will find a target note listing the pages in the adjacent frame.
3. When a map, drawing or chart, etc., is part of the material being photographed the photographer has followed a definite method in "sectioning" the material. It is customary to begin filming at the upper left hand corner of a large sheet and to continue from left to right in equal sections with small overlaps. If necessary, sectioning is continued again—beginning below the first row and continuing on until complete.
4. For any illustrations that cannot be reproduced satisfactorily by xerography, photographic prints can be purchased at additional cost and tipped into your xerographic copy. Requests can be made to our Dissertations Customer Services Department.
5. Some pages in any document may have indistinct print. In all cases we have filmed the best available copy.

University
Microfilms
International

300 N. ZEEB RD., ANN ARBOR, MI 48106



8217457

Schroeder, Larry Carl

PHYSICAL METALLURGY AND PROCESS IMPROVEMENT OF THERMITE
RAIL WELDS

The University of Arizona

PH.D. 1982

University
Microfilms
International 300 N. Zeeb Road, Ann Arbor, MI 48106

PLEASE NOTE:

In all cases this material has been filmed in the best possible way from the available copy. Problems encountered with this document have been identified here with a check mark .

1. Glossy photographs or pages
2. Colored illustrations, paper or print _____
3. Photographs with dark background
4. Illustrations are poor copy _____
5. Pages with black marks, not original copy _____
6. Print shows through as there is text on both sides of page _____
7. Indistinct, broken or small print on several pages
8. Print exceeds margin requirements _____
9. Tightly bound copy with print lost in spine _____
10. Computer printout pages with indistinct print _____
11. Page(s) _____ lacking when material received, and not available from school or author.
12. Page(s) _____ seem to be missing in numbering only as text follows.
13. Two pages numbered _____. Text follows.
14. Curling and wrinkled pages _____
15. Other _____

University
Microfilms
International



PHYSICAL METALLURGY AND PROCESS IMPROVEMENT
OF THERMITE RAIL WELDS

by

Larry Carl Schroeder

A Dissertation Submitted to the Faculty of the
DEPARTMENT OF METALLURGICAL ENGINEERING
In Partial Fulfillment of the Requirements
For the Degree of
DOCTOR OF PHILOSOPHY
WITH A MAJOR IN METALLURGY
In the Graduate College
THE UNIVERSITY OF ARIZONA

1 9 8 2

THE UNIVERSITY OF ARIZONA
GRADUATE COLLEGE

As members of the Final Examination Committee, we certify that we have read
the dissertation prepared by Larry Carl Schroeder

entitled PHYSICAL METALLURGY AND PROCESS IMPROVEMENT OF THERMITE
RAIL WELDS

and recommend that it be accepted as fulfilling the dissertation requirement
for the Degree of Doctor of Philosophy in Metallurgy.

<u>K. L. Kattar</u>	<u>13 April 1982</u>
Date	
<u>DR Duvier</u>	<u>12 April 1982</u>
Date	
<u>L J Berven</u>	<u>12 April 1982</u>
Date	
_____	_____
Date	
_____	_____
Date	

Final approval and acceptance of this dissertation is contingent upon the
candidate's submission of the final copy of the dissertation to the Graduate
College.

I hereby certify that I have read this dissertation prepared under my
direction and recommend that it be accepted as fulfilling the dissertation
requirement.

<u>DR Duvier</u>	<u>12 April 1982</u>
Dissertation Director	Date

STATEMENT BY AUTHOR

This dissertation has been submitted in partial fulfillment of requirements for an advanced degree at The University of Arizona and is deposited in the University Library to be made available to borrowers under rules of the Library.

Brief quotations from this dissertation are allowable without special permission, provided that accurate acknowledgement of source is made. Requests for permission for extended quotation from or reproduction of this manuscript in whole or in part may be granted by the head of the major department or the Dean of the Graduate College when in his judgment the proposed use of the material is in the interests of scholarship. In all other instances, however, permission must be obtained from the author.

SIGNED: 

ACKNOWLEDGEMENTS

Gratitude is extended to the following individuals and organizations for their support during this study:

The A.T. & S.F. Ry Co., Mr. Ted Mason and Mr. C.R. Kaelin and the Department of Technical Research and Development of that organization for the leave of absence and financial and technical support which made the author's participation in this study possible.

The Department of Transportation, Dr. R.K. Steel and others at the FAST facility for their technical and financial support and the production of the rail welds.

The Chemetron Corporation, Mr. R. Frost and Mr. G. Schmolke for providing materials and advice for producing the rail and plate welds.

Dr. G.H. Geiger and the Department of Metallurgical Engineering of The University of Arizona for initiating the study and for financial support.

Mr. D. VanReeth of the College of Mines of The University of Arizona for the machining of test specimens.

Dr. P.H. Wirsching, the author's minor advisor, of the Department of Aerospace and Mechanical Engineering of The University of Arizona for his advice and support during the study.

The author's mother and to the many others for their support.

A special note of thanks goes to Dr. David R. Poirier, the author's advisor, for the encouragement, advice and assistance needed to complete this study.

TABLE OF CONTENTS

	Page
LIST OF FIGURES.	vi
LIST OF TABLES	xi
ABSTRACTxiii
1. INTRODUCTION	1
1.1 Statement of the Problem.	2
1.2 Objectives of This Study.	3
2. REVIEW OF RELATED STUDIES.	5
2.1 Applications of the Aluminothermic Process.	5
2.2 Alternative Reductants to Aluminum.	5
2.3 Additives that Affect the Aluminothermic Process.	6
2.4 Thermite Rail Welds	9
2.5 Effects of Microstructure on Mechanical Properties	13
2.6 Residual Stresses in Welds.	31
3. EXPERIMENTAL PROCEDURES.	36
3.1 Rail Welds.	36
3.2 Plate Welds	48
4. RESULTS AND DISCUSSION	53
4.1 Mechanical Properties of the Rail Welds	53
4.1.1 Hardness Profiles.	53
4.1.2 Impact Properties.	61
4.1.3 Tensile Properties	63
4.1.4 Fractography of Impact and Tensile Specimens	69
4.1.4.1 Charpy V-Notch Specimens in the HAZ.	69
4.1.4.2 Charpy V-Notch Specimens in the Weld Metal	72
4.1.4.3 Tensile Specimens in the HAZ.	77
4.1.4.4 Tensile Specimens in the Weld Metal.	83

TABLE OF CONTENTS--Continued

	Page
4.2 Structural Analyses of Rail Welds	92
4.2.1 Macrostructures.	92
4.2.2 Microstructures.	96
4.2.3 Inclusion Evaluation in Rail Welds	103
4.3 Thermal Measurements.	106
4.4 Residual Stresses	116
5. RESULTS AND DISCUSSION OF PLATE WELDS.	122
5.1 The Effects of Filtering.	122
5.2 Mechanical Properties of Plate Welds and the Effects of Normalizing	126
5.2.1 Hardness Profiles.	126
5.2.2 Tensile Properties	131
5.2.3 Fractography of Tensile Specimens.	137
5.3 Structural Analyses of the Plate Welds.	142
5.3.1 Macrostructures.	142
5.3.2 Microstructures.	142
CONCLUSIONS.	150
APPENDIX A: LINEAR REGRESSION EQUATIONS FOR FIGURES	157
APPENDIX B: MICROSTRUCTURAL CHARACTERIZATION OF THERMITE RAIL WELDS	161
REFERENCES	177

LIST OF FIGURES

<u>Figure</u>		<u>Page</u>
1	Residual stresses in a nonreinforced rail weld; weld gap - 24 mm, 50 kg/m rail. From Dohse (77).	34
2	Mold configuration and flow pattern of the molten steel for the thermite rail welds.	40
3	Thermocouple locations for welds 1, 2 and 4. For weld 3, all thermocouples were 3 mm closer to the rail end. Numbers identify the thermocouples and the dimensions are in mm. The rail is 68 kg/m (136 lb/yd RE).	41
4	Locations of thermocouples in the weld metal of weld 9. Thermocouples were centered longitudinally in the 24 mm gap. A-Head, B-Web, C-Base. Dimensions in mm.	43
5	Locations of tensile and impact specimens, hardness profiles and microstructure specimens in welds. Fusion zones and outer edges of the HAZs are indicated	45
6	Locations of strain gage rosettes for residual stress measurements. Letters identify locations and the dimensions are in mm.	47
7	Mold configuration and steel flow pattern for plate welds	50
8	Hardness profiles of welds 1, 4 and 7	54
9	Hardness variations in the HAZs of alloy rails relative to the hardness of parent rail. Numbers in parentheses are the numbers of respective rails	56
10	Hardness variations in the HAZs of standard and of head-hardened rail relative to the hardness of parent rail. Numbers in parentheses are the numbers of respective rails.	57

<u>Figure</u>		<u>Page</u>
11	Hardness of the weld metal as a function of preheat time and distance from the weld centerline. Numbers in parentheses are the numbers of respective rails	60
12	Tensile properties of weld metal as a function of hardness. *From Ref. (24); not included in linear regression analyses.	67
13	Fracture of impact specimen through the region of minimum hardness in heat-affected zone. Fractograph is from the CrMo side of weld 1. 17X	71
14	Fracture surface of Figure 13; (a) original rail side; (b) HAZ side. 280X.	73
15	Fracture of impact specimen through the region of minimum hardness in the HAZ of the HH rail of weld 8. (a) original rail side; (b) HAZ side. 280X	74
16	Delamination of the HAZ side (region of minimum hardness) of the impact specimen from the CrV rail of weld 4. Bottom of the photo micrograph is the side opposite the V-notch. 52X	75
17	Fractures of impact specimens from the weld metal. (a) weld 1, alloy weld metal; (b) weld 8, st'd. weld metal. 280X	76
18	Low ductility tensile fractures in the region of minimum hardness. (a) weld 1-Cr rail; (b) weld 4-st'd. rail. 24X	78
19	"Cup and Cone" tensile fractures in the region of minimum hardness. (a) weld 1-CrMo rail, 23X; (b) weld 8-HH rail, 28X.	79
20	"Cup and Cone" tensile fractures with radial features in the region of minimum hardness. (a) weld 4-CrV rail, 25X; (b) weld 8-CrMo rail, 29X	80
21	Tensile fractures in the region of minimum hardness. (a) weld 4-st'd. rail, 240X; (b) weld 4-CrV rail, 250X	84

<u>Figure</u>		<u>Page</u>
22	Tensile fractures of the weld metal. (a) weld 3-alloy weld metal; (b) weld 4-st'd. weld metal. 25X.	85
23	Fracture of the tensile specimen from the standard weld metal of weld 6. (a) 50X; (b) 270X.	87
24	Macrostructure of the head area of weld 6. 1X.	88
25	Tensile fracture of the alloy weld metal of weld 10 showing microporosity. 290X.	91
26	Macrostructure of weld 2-alloy weld metal. Note the thermocouple locations. Approximately one-half size.	93
27	Macrostructure of weld 10 showing the effect of a long preheat. Approximately one-half size.	94
28	Hardness as a function of the percent of transitional pearlite and bainite at various locations in the rail welds	97
29	Proeutectoid ferrite in the weld metal of weld 6. 450X	98
30	Alumina (with silica) inclusions in the CrV fusion zone of weld 6. The weld metal is to the right of the inclusions. 32X	99
31	Pearlitic structure (a) and transitional pearlite and bainite (b) in weld metal of weld 14. 4500X	100
32	Very fine transitional pearlite in the HAZ of the Cr rail of weld 1. 4500X.	101
33	Spheroidite and degenerative pearlite in the outer edge of the HAZ of the HH rail of weld 7. 4500X	102
34	Temperature as a function of time and position in the rail during the welding process for weld 1. Refer to Figure 3 for the locations of the thermocouples	107

<u>Figure</u>	<u>Page</u>
35	Temperature as a function of time and position in the weld metal of weld 9. Refer to Figure 4 for the locations of the thermocouples 108
36	Rail temperature distributions at the end of preheat. Curves are extrapolated to the rail end. 110
37	Peak temperatures as a function of distance from the rail end: (a) weld 1; (b) weld 2. Standard preheats. The numbers in parentheses identify the thermocouple locations shown in Figure 3 112
38	Peak temperatures as a function of distance from the rail end: (a) rail 4-standard preheat; (b) weld 3-long preheat. The numbers in parentheses identify the thermocouple locations shown in Figure 3. 113
39	Principal residual stresses in weld 11. The lengths of the vectors are proportional to the magnitude of the stresses. The letters correspond to the locations of the rosettes shown in Figure 6. 119
40	Cross-sections of the filter system for weld 9-X. From top to bottom: filter A before use; filter B after use; vertical section showing remnants of filter A, the beads and filter B 123
41	Hardness profiles of welds 1-X, 2-X and 7-X. 129
42	Hardness profiles of welds 1-X.3 and 2-X.5 with the hardness of the weld metal in welds 7-X.3 and 8-X.5. 130
43	Hardness of the plate weld metal as a function of cooling rate through the transformation range. 133
44	Tensile properties of plate weld metal in the as-cast and heat-treated conditions. 136
45	Tensile properties as a function of hardness for various groups of welds. 138
46	Reduction of area as a function of hardness for all welds. 139

<u>Figure</u>		<u>Page</u>
47	Fracture of the tensile specimen from weld 7-X. (a) 30X; (b) 310X	140
48	Fracture of the heat-treated weld tensile specimen 9-X.5. (a) 23X; (b) 240X.	141
49	Macrostructure of weld 4-X. 0.96X.	143
50	Proeutectoid ferrite in as-cast plate welds. (a) 1-X, 0.44 percent carbon; (b) 7-X, 0.59 percent carbon. 150X	144
51	Effects of heat treatment on (a) 0.46 percent carbon weld, 4-X.4; (b) 0.59 percent carbon weld, 7-X.4. 150X.	146
52	Pearlite and transitional pearlite in weld 9-X. (a) 4500X; (b) 22,000X.	147
53	Bainite in weld 3-X. (a) 4500X; (b) 22,000X.	148

LIST OF TABLES

<u>Table</u>		<u>Page</u>
1	Mechanical Properties from Bend Tests on Rail and on Welded Rail.	12
2	Experimental Conditions for Rail Welds.	37
3	Nominal Composition of Rails and of Weld Metal.	39
4	Experimental Conditions for Plate Welds	49
5	Hardnesses of the Heat-Affected Zones in the Rail Welds.	58
6	Impact Energies of the Rail Welds at 20°C	62
7	Tensile Properties of the Rail Welds.	64
8	Fracture Characteristics of Tensile Specimens of the Heat-Affected Zones in the Rail Welds.	81
9	Fracture Categories of Tensile Specimens in the Region of Minimum Hardness.	82
10	EDS Analyses of the Surface of the As-Cast Columnar Grains in Standard Weld Metal.	89
11	EDS Analyses of the Surfaces of Dendrites in Alloy Weld Metal.	90
12	Inclusion Content of the Weld Metal in the Rail Welds.	105
13	Time in the Transformation Range During Cooling	115
14	Principal Residual Stresses in Weld 11.	117
15	Inclusion Content of the Weld Metal in the Plate Welds	125
16	Hardness and Dimensions of Plate Welds.	127
17	Hardness of Plate Welds After Normalizing	128

<u>Table</u>		<u>Page</u>
18	Composition of Weld Metal in Plate Welds.	132
19	Tensile Properties of the Plate Welds	134

ABSTRACT

This study was an evaluation of thermite rail welding with the goal of the development of welds with improved mechanical properties.

The first part of the study involved an in-depth evaluation of 14 thermite rail welds produced by the Department of Transportation using current production practices. These welds were produced using CrMo, CrV and Cr alloy rails, AREA CC rails (i.e., standard rails) and head-hardened rails which were welded with weld metal produced by the aluminothermic reaction of "standard" and "alloy" thermite charges. Temperature at various locations was measured during welding for both the rails and the weld metal. After welding, mechanical properties, macro- and microstructure, inclusion levels and residual stresses induced by the welding operation were all determined. Low impact properties and ductility (2-6 percent reduction of area) were observed in the thermite rail weld metal. These low properties were attributed to microstructure and, to a lesser extent, inclusion content. In order to improve the process by reducing the inclusion content, attempts were made to filter the molten thermite steel by passing it through zirconia/mullite filters. This was included in the second part of the study in which 9 plate welds were made using "standard" thermite charges. Filtering, at best, was only partly successful. However, it was observed that a 30 percent increase in yield strength and hardness was achieved in weld metal containing approximately 0.55 percent carbon and 0.06

percent vanadium. Normalization of the plate welds resulted in a significant improvement in the tensile ductility of as-cast weld metal. Weld metal of 0.55 percent carbon and 0.06 percent vanadium had ductilities in the range of 10-20 percent when the cooling rate exceeded 37 K°/min. through the transformation range. At cooling rates of four times this level, tensile properties equivalent to those of the "alloy" weld metal were obtained along with the enhanced tensile ductility.

It was concluded that it is possible to produce a thermite weld with both improved strength and ductility by the judicious control of composition, the addition of microalloying elements and the application of an appropriate post-weld heat treatment, such as normalization.

1. INTRODUCTION

The aluminothermic process is credited to Goldschmidt for his development in 1898 of a process for reducing iron and other metals from their oxides by igniting mixtures of the oxides and powdered aluminum (1, 2). The first, and still the most common, application of the aluminothermic process is the thermite welding of railroad rails (3). As early as 1908, Goldschmidt (4) mentioned the existence of 200,000 thermite rail welds in Europe. Thermite rail welds were not introduced to the U.S. railways until the 1930's when the continuous-welded rail (CWR) was developed as a means for higher speeds and car loadings on rail.

Typical CWR consists of rail "strings", 439 meters (1440 feet) in length, that are fabricated by electric-flash butt (EFB) welding of individual rail "sticks". The sticks are steel mill products, which are hot rolled from ingots or continuously cast billets, and are typically 12 meters (39 feet) in length. The fabricated strings are transported to the track site and layed at an ambient temperature that avoids excessive thermal stresses which can arise from fluctuations of the ambient temperature. The joining of the strings requires a thermite weld every 439 meters (1440 feet); the welds are staggered on the parallel rails of a track to avoid simultaneous or harmonic loading. Also, CWR is repaired by removing damaged or worn segments of rail and by thermite welding the repair sections in place.

1.1 Statement of the Problem

Since the development of the rail systems in this country, the sizes of the rolling stock and of the trains have been steadily increasing. Today, for example, 124 MN (14,000 ton) unit coal trains with 0.9 MN (100 ton) cars are not uncommon. However, the basic design of the track and roadbed system has not changed significantly since the early 1900's. The net effect is a substantial increase in the service stresses to which rails, welds and related components are subjected.

Based on a summary of the status of thermite welding of rail by Hauser (5, 6) and on an evaluation of mechanical properties by Myers (7), it has been shown that the weld metal in thermite welds exhibits low ductility, low impact energy and low fatigue strength. Typical properties are only 1-3 percent reduction in area and 2.7-5.4 J (2-4 ft-lb_f) in Charpy impact energy at room temperature (7). These low mechanical properties were attributed to undesirable microstructures and to a high concentration of nonmetallic inclusions in the weld metal.

According to Hauser (5, 6), the most common mode of weld failure in service is due to fatigue cracks that nucleate in sites of porosity and/or inclusions in the weld metal and in regions which do not completely fuse the parent rail. Current data do not allow indisputable comparisons of failure rates for various types of rail welds although it appears that the expected life of a thermite weld is only half that of an EFB weld (5, 6). Also, since thermite welds in rails

have remained almost unchanged since their development, it is thought that the high stresses associated with current service have significantly reduced the fatigue life and critical flaw size of thermite rail welds.

1.2 Objectives of This Study

Although there are alternatives to the thermite process for in-track welding of rails (such as in-track EFB, gas-pressure welding, arc and electroslag welding and variations thereof), the thermite process is widely used, and will probably continue to be so, in spite of its shortcomings. This is due primarily to the low costs of the equipment and to the ease and speed of installations of on-site thermite welds (5, 6). Thus, the overall objectives of this study are to evaluate the properties of thermite welds in rails and to determine means by which thermite rail welds can be improved.

The study involves the evaluation of 14 thermite rail welds produced at the DOT-FAST* facility in Pueblo, CO and 9 thermite plate welds produced at The University of Arizona. The rail welds include variations in rail and weld chemistry, length of preheat period and method of postcooling. Time-temperature data at various locations in the rail were obtained for the complete cycles of several welds. In addition, thermal data were obtained for the filler-metal for one of the welds. Impact energy, tensile properties and hardness were measured for the weld metal and the heat-affected zones for 13 of the welds.

*DOT-FAST is the acronym for Department of Transportation Facility for Accelerated Service Testing.

One weld was evaluated for residual stresses produced by the welding operation, and macro- and microstructures from representative welds were studied.

The plate welds were produced using one weld chemistry and various zirconia filter systems in an attempt to reduce the inclusion level of the weld metal. This resulted in a significant increase in the yield strength of the filtered welds. Several heat treatments were also applied to weld samples in order to obtain significant increases in tensile ductility with no or little sacrifice in hardness, yield strength and ultimate tensile strength.

Thus, the study can be considered as an evaluation of the current state of the art of thermite welding with the introduction of a means of improving the properties of these welds.

2. REVIEW OF RELATED STUDIES

2.1 Applications of the Aluminothermic Process

Since its inception, the most widespread use of the aluminothermic process has been the thermite welding of ferrous alloys (3). There have been many applications in the extraction of refractory metals and in steel castings as a riser and feeding aid (1, 2). A process has been developed by Mehra et al. (1) for the production of molybdenum from calcium molybdate by aluminothermic reduction; molybdenum has also been reduced from its oxide by aluminum (8). The aluminothermic reaction has also been applied to the production of ferrochrome, ferrocolumbium, ferrotungsten and other ferroalloys (9-11). If not economically competitive themselves, these processes appear as valuable aids in optimizing ore, reducing agent and flux combinations for large scale reduction operations (8-10). With suitable fluxing agents, binders and excess aluminum, the aluminothermic reaction can be used to produce refractory linings (2). Only enough iron oxide is used to initiate the reaction, and once initiated, the aluminum reacts with the atmosphere to produce the refractory alumina. The fluxing agents aid in binding the alumina into the shape of a refractory vessel or mold.

2.2 Alternative Reductants to Aluminum

Studies on the use of reducing agents, other than aluminum, were made by Belitkus (12). One of the factors involved in the selection of a reductant for a particular metal oxide, is the requirement

that the reaction have a free energy change amenable to a high yield of the reaction products. The reaction should also be exothermic in order to produce the superheat necessary to sustain the reaction and to minimize oxide and reductant contamination in the metal produced. Some alternative reductants to aluminum are calcium, magnesium, silicon, carbon and hydrogen (12, 13). For the latter three, the heat of reaction is insufficient to sustain a reaction without external heat. The relatively low boiling points of calcium and of magnesium (1482°C and 1103°C, respectively) coupled with the high melting points of their oxides (2480°C and 2800°C, respectively) require that the reactions be conducted in pressure-tight vessels and at high temperatures to insure complete reaction and metal-slag separation. Aluminum, while having a lower heat of formation of the oxide than do calcium and magnesium, is the optimum choice as a reductant because it has a boiling point of 2467°C, an oxide melting point of 2045°C and a heat of formation of the oxide which is adequate for sustaining the reactions.

2.3 Additives that Affect the Aluminothermic Process

Aluminothermic charges for producing iron or iron-alloy welds are composed of aluminum powder, a finely divided ore or iron oxide, usually a flux, and often a thermal booster. Alloy elements are usually introduced in the form of ferroalloy pellets dispersed throughout the charge. Relatively pure iron pellets may also be present to reduce the amount of superheat produced.

The most common reactions used in formulating thermite rail weld mixtures involve the reduction of Fe_3O_4 and/or Fe_2O_3 to produce

the molten iron filler-metal (5, 14); mixtures of these oxides and FeO may also be used (15). The reduction of Fe_3O_4 by aluminum liberates 79.9 kcal per mole of iron produced for an adiabatic reaction temperature (ART) of 3088°C, and the reduction of Fe_2O_3 produces 90.8 kcal per mole of iron produced for an ART of 2960°C, whereas Delachaux (15) gives the ART for Fe_3O_4 reduction as 2590°C. In view of these discrepancies, the ART and energy liberated were calculated for the Fe_3O_4 reaction. Utilizing data from Kubaschewski and Alcock (16), U.S. Steel Corp. (17) and the JANAF tables (18), the ART for the reduction of Fe_3O_4 by aluminum was determined as 2697°C with the energy liberated as 89.2 kcal per mole of iron produced.

The amount of aluminum is usually 10-15 percent in excess of the stoichiometric amount for completion of the reaction. This has been found to result in the highest yield of the desired metal product (1, 8, 9, 12, 19). The need for excess aluminum is attributed to mechanical segregation of the oxide and aluminum particles prior to ignition and to the desirability of producing weld metal with about 0.4 percent aluminum (20).

The metal product of an aluminothermic reaction should be free of the alumina-rich slag which forms. The metal-slag separation requires time, and time available for separation is directly related to the amount of heat available from the aluminothermic reaction. If the reaction proceeds too slowly, then there is more heat-loss to the surroundings, and the reaction temperature is too low, thereby producing a molten metal with little superheat. The rate of the reaction is most

noticeably affected by changes in the particle size and the amount of excess aluminum (9).

When very fine aluminum particles (less than 3-5 μ radius) are used, the reaction proceeds the most rapidly due to a high reactant surface area. These reactions closely approach adiabatic conditions and yield the highest peak reaction temperature. However, it has been demonstrated that these reactions do not yield the highest purity of metal product (9). It is thought that the aluminum reacts so rapidly that secondary reactions, such as reaction of the alumina with the fluxing agent or of the thermal booster (if present), do not have time to go to completion during the brief period the maximum superheat is available for the metal-slag separation. It is also thought that the violence of the reaction blows much of the fine aluminum out of the reaction vessel, thus reducing the amount available for reduction of the oxide (20).

Reactions involving aluminum particles of greater than 500 μ radius result in a product which contains slag since the reaction rate is slow enough that heat losses result in a low peak temperature. For good metal-slag separation, a high peak temperature and adequate time at that temperature are required. The optimum condition occurs with aluminum particles with a mean radius in the range of 3-500 μ (9).

A commonly used flux is calcium oxide, CaO. It is usually added in quantities to produce a 70-80 percent alumina slag with a melting point of 1800°C (12). While the use of flux lowers the melting point of the slag, heat is absorbed from the reaction to raise the CaO to the reaction temperature of the alumina. This reduces the amount of

superheat available to the metal product. If the heat of reaction is insufficient to produce good metal-slag separation, a thermal booster such as sodium chlorate may be added to the charge. The sodium chlorate reacts with excess aluminum to yield about 2,200 kcal per kg of reactants. An additional product of this reaction is sodium chloride which separates into the slag phase. An alternative to a thermal booster is preheating of the aluminothermic charge.

2.4 Thermite Rail Welds

The adiabatic reaction temperature (ART) of iron oxide and aluminum powder is in the range of 2600-3100°C, as discussed above; the most reliable estimate for the ART is 2700°C. Regardless of the reaction employed, heat losses reduce the temperature of the molten iron to about 2000°C before the weld is actually poured (6). Flux and alloy additions further reduce this temperature. In practice, weld charges are designed to produce a molten weld metal with a superheat of 400-500°C (14).

According to Ashton (20), precise control of the composition of a thermite charge is necessary so that, after the reaction, about 0.4 percent excess aluminum is in the molten weld metal. Not enough aluminum can cause the oxidation and loss of the alloying elements, carbon and manganese, resulting in a weld with poor wear properties. This condition can also result in a very violent reaction due to the evolution of carbon monoxide. Typically, a large portion of the manganese from ferromanganese pellets is lost to the slag; however, an excess of aluminum increases the recovery of manganese significantly. On the other

hand, discretion must be exercised since excessive aluminum can lead to weld embrittlement.

Another critical factor in the production of an acceptable thermite weld is the "taptime" or the interval from ignition of the reaction until the crucible is tapped (i.e., when the weld is poured). Ashton (20) summarizes the sequence of events as: ignition to 15 seconds, vigorous reaction occurs; 15-25 seconds, vigorous reaction ceases and slag rises; 25 seconds on, slag separation nearing completion and loss of superheat is beginning. The optimum taptime is thus 20-25 seconds. Data on the failure load of a bend test of welded rail sections versus taptime support this; the failure load shows a maximum at a taptime of about 22 seconds (20).

In addition to these factors, the production of a good weld also involves the mechanics of proper rail cutting and surface preparation, rail alignment, mold placement and proper preheating. But, even though a thermite weld is installed according to recommend procedures, its mechanical properties are usually lower than those of the parent rail. From Sonon et al. (21), control-cooled (CC) standard rail has an average yield strength of 483 MPa (70 ksi), a tensile strength of 910 MPa (132 ksi), an elongation of 11 percent (2.54 cm or 1 in. gage) and a reduction of area of 14 percent. Note that these properties vary considerably within the AREA compositional specification for CC rail. The data of Sonon et al. (21) for yield and ultimate strength, have a standard deviation of 41 MPa (6 ksi). By comparison, typical values for thermite welds are a tensile strength of 793 MPa (115 ksi), an

elongation of 1-3 percent (12.7 cm or 5 in. gage length) and a reduction of area of 1-3 percent as reported by Myers (7) and Geiger (22).

Specimens used in the latter two works (2, 22) were removed from the weld metal. However, mechanical properties of welds in rail are usually reported in terms of the results of bend tests conducted on rather long lengths of welded rail. Results collected by Hauser (5) and made available by the A.T. & S.F. Railway Company (23) are given in Table 1. These include properties of rail, thermite welds and electric flash butt (EFB) welds. EFB welds are plant welds and are included in the table because such welds are considered to be more reliable in service than thermite welds. The data collected from Hauser (5) are from four point bend tests with a 122 cm (48 in.) span; the loads are applied symmetrically at points 15 cm (6 in.) on both sides of the weld. The data of A.T. & S.F. are from a three point bend test, 122 cm (48 in.) span, in which one load is applied at the weld itself. In all cases, the rail is so-called "CC standard rail".

The scatter that was noted for the bend test results reported by Hauser (5) for thermite welded rails appeared to offset the effect of loading with the head or base down. However, the method of loading, 4-point or 3-point, does affect the results, particularly for thermite welds. The 4-point method subjects the weld to pure bending, whereas the 3-point method introduces a shear stress in the weld. In any case, the conclusion is that, even though a thermite welded rail may sometimes sustain a load greater than a rail or an EFB weld, it does not have the ductility necessary to deflect significantly before failure.

Table 1. Mechanical Properties from Bend Tests on Rail and on Welded Rail

Rail Size Kg/m (lb/yd)		Weld	Loading	Max. Load		Max. Deflection		Reference
				KN	(kip)	cm	(in)	
65	(131)	None	Head down	1334	(300)	5.3	(2.1)	5
65		EFB	Head down	1401	(315)	6.4	(2.5)	5
65		Thermite	Head down	1148- 1757	(258- 395)	1.0- 3.6	(0.4- 1.4)	5
68	(136)	None	Base down	1334	(300)*	13.7	(5.4)	23
68		EFB	Base down	890- 1334	(200- 300)	1.8- 7.6	(0.7- 3.0)	23
68		Thermite	Base down	712- 979	(160- 220)	1.3- 2.5	(0.5- 1.0)	23
68	(136)	None	Lateral	445	(100)*	22.6	(8.9)	23
68		EFB	Lateral	445	(100)*	19.8	(7.8)	23
68		Thermite	Lateral	178- 298	(40- 67)	1.0- 3.8	(0.4- 1.5)	23

* Did not fracture.

This fact is significant because thermite welds are placed in track in the span between two ties. The net effect is that thermite welds do not have base support and are subject to the high flexural loads and deflections that occur in service.

2.5 Effects of Microstructure on Mechanical Properties

Much of what follows is a review of the literature on factors which contribute to embrittlement, cracking and/or lack of toughness and ductility in steel and in steel welds. To adequately cover these topics, the scope of this discussion is not restricted to thermite welds because there is a paucity of literature on the mechanical properties and microstructures of such welds.

The most extensive work on the metallurgical structure and mechanical properties of thermite welds in rails is that reported by Myers et al. (24). Their study included macrostructures and microstructures of welds, as well as mechanical properties which consisted of hardness traverses across welds and tensile properties and Charpy impact energies of the weld metal. The major conclusions of that study follow:

1. The weld metal exhibited low tensile ductility and low impact energy. The fractures of the tensile and impact specimens were almost completely brittle.
2. The microstructures of the weld metal in some of the welds showed intragranular Widmanstätten ferrite and upper bainite in

other welds. These constituents were thought to be at least partly responsible for the brittle behavior of the weld metal.

3. Columnar dendrites aligned in the direction of heat flow (i.e., the axial direction of the rail) comprised the cast structure of the weld metal. Microporosity and numerous inclusions were observed, and these heterogeneities were significant contributing factors for the low tensile ductility and impact energy of the weld metal.

4. Grain boundary precipitates were not observed on extraction replicas when viewed under a transmission electron microscope so that the brittleness of the weld metal could not be attributed to grain boundary embrittlement due to such precipitates. However, grain boundary segregation without precipitation could not be eliminated as a contributing factor.

Ezhov (25) studied the welding of steel castings of variable thickness (100-400 mm) with a parent structure of very fine pearlite and tempered martensite in which transgranular cracking was encountered in the heat-affected zones (HAZ) of the welds in the thickest sections. The cracks occurred in the martensitic structure of greatest hardness of the HAZ. Further, inclusions were noted and were found to be of the same type in both thick and thin areas (MnS, sulfides with aluminates, silicates and oxides) but the inclusions were coarser and more populous in the thicker sections. Crack initiation was influenced by the presence of the inclusions, but this did not fully explain why the

structure of highest strength (martensite) failed preferentially. Ezhov (25) also observed that martensite, tempered or untempered, was much more susceptible to hydrogen embrittlement than was very fine pearlite. Given the same concentration of diffused hydrogen, the fracture strength of the former was about half that of the latter. For welds in the thick sections of the castings, the concentration of hydrogen was greater in the martensite structure of the HAZ than in the parent material or the weld metal. Hydrogen was not detected in welds in the thin sections of the castings. Ezhov (25) concluded, therefore, that the primary cause of weld failure was contamination of the martensite structures in the HAZ by diffused hydrogen encountered in the welding process (such as from moisture).

Heller and Beck (26), in a study of flame cutting and welding of rails, found that the element which deleteriously influenced tensile and impact properties of the HAZ and fusion zone the most was carbon, followed by manganese. In addition, microsegregation that occurs in rail banding was found to have significant influence on the transformation products in the HAZ, particularly adjacent to the fusion zone. This segregation is detrimental in that it promotes the formation of martensite in this region.

Another degrading factor is the grain coarsening that occurs in the HAZ just adjacent to the weld. Grain coarsening was noted by Heller and Beck (26) only for welding and not for flame cutting. When it occurs, the grain coarsening increases the tendency to brittle fracture. The high austenitizing temperatures from the welding operation promote

formation of the coarse grains and, coupled with rapid cooling rates in the region, promote the formation of brittle martensite (26, 27).

Heller and Beck (26) also observed hydrogen absorption in some thermite welds. After weld solidification, the concentration of hydrogen was approximately equal to the maximum solubility in austenite (26). If the cooldown rate is too rapid, i.e., the weld metal does not have time to give up sufficient hydrogen to the rail steel, cold cracking of the weld may occur (26, 28). On the other hand, diffusion of hydrogen into the HAZ of the rail steel may result in exceeding the critical content; this can produce cold cracking in this region of the HAZ which is adjacent to the fusion zone (26). Heller and Beck (26) strongly recommend that the thermite kits be moisture free and the welds cool slowly enough to allow hydrogen, if present, to diffuse extensively so that a critical concentration does not occur in any one area of the weld or rail.

In a study of welds in medium-alloy steels, Makara and Sarzhetskii (29) conclude that the HAZ near the fusion zone has a region with columnar type grains whose boundaries form as a result of the fusion of nonmetallic inclusions and microsegregated elements in the base metal. They found that the impact energy at the fusion zone is affected by the size of these columnar grains, and the austenitic grains therein, and the conditions of their boundaries with respect to both chemical inhomogeneity and inclusions at the grain boundaries. The width of this region and the size of these columnar grains largely determine the resistance to hot- and cold cracking and the susceptibility to brittle fracture. To reduce the influence of this region on the

probability of weld failure, the width of this region and the size of the grains therein must be restricted. This can be achieved by using highly concentrated weld heat sources (such as an electron beam) with the simultaneous reduction of heat input, using refined parent steels with low levels of finely divided and uniformly distributed inclusions and by the use of filler-metals with reduced melting points. In the case of pressure welds, such as EFB welds, these low strength regions are expelled as flash, resulting in a greater strength of the welded joint.

According to Borland (30, 31), there is a "brittle temperature" range during solidification of weld metal in which strength and ductility are very low. Solidification cracking during welding most likely initiates in this brittle temperature range because the developing bridges of dendritic solid have insufficient strength to resist the contraction of the weld and parent metal. In some cases, the cracking may occur by a separation of a thin film of liquid which remains at the end of solidification. Elements that lower the ratio of the solid-liquid interfacial energy to the grain boundary energy promote crack initiation and propagation by retarding the growth of the solid bridges during the dendritic solidification. Severe cracking is attributed to the combined effect of expansion strain at the front and contraction strain at the rear of the solidifying pool. Local preheating and post-heating can reduce or inhibit cracking if applied correctly at proper locations.

For welds in low carbon steels, Lebedev (32) observed grain boundary segregation of sulfur and phosphorus in the weld metal and the extent of the segregation was controlled by the solidification cooling

rate of the weld metal. For cooling rates less than 250 C°/s, sulfur and phosphorus diffused to the grain boundaries so that the compositions of these elements were greater at the grain boundaries than at the center of the grains. For cooling rates greater than 250 C°/s, the diffusion process was sufficiently inhibited to the extent that the distribution of sulfur and of phosphorus was uniform within the grains. A reduction in the level of segregation resulted in welds with an increased resistance to solidification or hot cracking and a greater weld strength.

In the welding of high-strength steels with weld metal of similar composition, Makarov (32) observed cold cracking in the weld metal. When the steels had martensitic structure, these cracks were located on the prior austenitic grain boundaries (33). Resistance to cold cracking depended on the shape, dimensions and chemical inhomogeneity of these boundaries. Makarov (33) found that additions of elements such as Mo, W (<1%), Ni (>3.5%), and Si and Cu increased the resistance to cold cracking whereas C, Mn, Cr and Co reduced it. In welds which resisted cold cracking, the solidification structure of the weld metal was equiaxed and had a small austenitic grain size with minimum segregation at the grain boundaries. Molybdenum had the most pronounced effect on promoting an equiaxial solidification structure and, thereby, improving resistance to cold cracking.

Boniszewski (34) found effects of inclusion level and certain alloying additions on grain boundary strength with respect to the susceptibility of welds in ferritic steels to reheat cracking during post weld heat treatment. Reheat cracking is a form of creep-rupture

which occurs at the prior austenitic grain boundaries. Steels containing Cr, Mo and V, individually or in combination, were found to be most susceptible to reheat cracking. Impurities such as P, residual elements (Cu, As, Sb) and some deoxidants (Al) were also detrimental; other deoxidants such as Ti, Zr, Ca and Ce were beneficial or neutral. Steels with lower inclusion contents had a decreased susceptibility to reheat cracking.

Boniszewski (34) and McPherson (35) in separate studies have shown that grain boundary segregation in prior austenite and residual stresses cause reduced impact energy, lower fracture toughness and reheat cracking during stress-relief for welds in ferritic steels. Welds in steels containing small amounts of vanadium appear particularly susceptible to HAZ reheat cracking (35). Similarly, Joshi and Stein (36) and Marcus et al. (37) have attributed the temper embrittlement of low alloy steels to grain boundary segregation in prior austenite; impurities such as Sb, P, Sn and As as well as the alloying elements, Ni and Cr, segregated to the boundaries. The Cr may form grain boundary carbides, and the combined presence of Cr and Ni leads to more extensive grain boundary segregation of Sb, Sn and P. Joshi (38) attributed the segregation of grain boundaries to the lowering of the energy of high-energy grain boundaries by segregates and precipitates. In quenched steels, these are the prior austenitic boundaries. In some cases, tempering results in more grain boundary segregation and embrittlement of these boundaries.

Kiessling and Lange (39) state that inclusions have a detrimental effect on fatigue life and on the tensile and impact properties

of steels. For fatigue life, spherical nondeformable oxide inclusions; such as calcium-aluminates and alumina, are the most detrimental. Sulfides, being easily deformed, are least harmful. During steel deformation, sharp edged cavities may develop around the nondeforming inclusions; also, alumina inclusions often exist in angular form. These cavities and sharp edged inclusions serve as the nuclei of fatigue cracks. Kiessling and Lange (39) also state that there is a critical size of these nondeforming inclusions which must exist before the inclusions reduce fatigue life. This size is a function of depth below the steel surface; this critical size is 10 microns just below the surface to 30 microns at a depth of 100 microns. For smaller inclusions, no effects of fatigue life were observed. Further, the tensile properties of sintered compacts of pure iron containing alumina particles of 15-35 microns size and 1-7 volume percent have been compared to the properties of pure sintered iron (39). While this inclusion content is higher than the normal content found in steels, the results indicate the trend of the effects of inclusion on tensile properties. As inclusion content increased, the yield strength, elastic limit, ultimate tensile strength and ductility all decreased. Particle size was noted as less important than the volume fraction of the particles. Also, impact strength tended to decrease with increasing inclusion content, but the transition temperature did not change.

According to Farrar and Dolby (40), lamellar tearing in welded steel plate is related to the short transverse ductility of the plate, and, in turn, the short transverse ductility is inversely related to the inclusion content of the plate. If the volume fraction of inclusions is

0.01, the percent reduction of area is 10 percent or less for short transverse specimens, whereas to achieve a percent reduction in area of 50 percent, the volume fraction of inclusions must be less than 0.002. The percent reduction in area approaches zero as the volume fraction of inclusions exceeds 0.015. The ductility is also a function of the strength level of the steel; smaller defects become more significant in high-strength steels.

Aydinceren and Kondic (41) studied the effects of sulfide inclusions on the mechanical properties of low carbon steels, 0.22-0.27 percent carbon. They found that yield strength was mainly dependent on the ferrite-pearlite composition of the microstructure and was essentially independent of sulfide content. Ultimate strength did decrease slightly as sulfur content increased, but was still governed by microstructure. The elongation, reduction of area and impact properties, however, were governed by sulfide content as compared to microstructure. For as-cast and normalized tensile specimens, reduction of area decreased from 35 percent for a sulfur level of 0.03 percent to an asymptotic value of about 6 percent at a sulfur content of 0.1 percent and above.

Norring et al. (42) extended these effects to include oxides for HSLA (high-strength low-alloy) steels. In order to prevent lamellar tearing, increase ductility and improve transverse impact properties, oxide and sulfide levels must be minimized. Assuming that the inclusions are either alumina or silica, the reduction of area increases significantly for volume fractions of less than 6×10^{-4} for pure

alumina or 7×10^{-4} for pure silica. Above these volume fractions, reduction of area is unaffected by changes in inclusion level.

Rittinger and Fehervari (43) found that welds of microalloyed steels were more sensitive to lamellar tearing than silicon-killed steels. This is attributed to the presence of low-melting sulfides and sulfonitride eutectics as inclusions. It was noted that an excess of microalloy elements in solid solution reduced weld toughness and that the best results were obtained when these elements were combined as nitrides.

Anisotropy effects become noticeable where nonspherical, preferentially oriented inclusions, such as MnS inclusions in rolled products, are present (44). Oono et al. (45) have shown that the addition of calcium to rolled steel products changes the shape of the sulfide inclusions from elongated to spherical. This results in almost isotropic properties, significantly improved resistance to lamellar tearing and improved toughness of the HAZ in welds of this material.

In studies of billets of AISI 4340 (a low-alloy steel), Hauser and Wells (46) demonstrated that transverse reduction of area, transverse impact energy and longitudinal and transverse fracture toughness all increase with decreased inclusion content and inclusion size. Fracture toughness improved linearly with a reduction in inclusion level to a certain value, at which point it became essentially constant. The percent reduction in area appeared to be the most sensitive to the inclusion content. Similar studies by Blake (47), Volchok et al. (48), and those reported at the Port Chester Symposium (44), support these conclusions.

Gladman et al. (49) have related the tensile and impact properties of medium to high carbon steels (0.4-0.8% C) to the proportions of ferrite and pearlite and the pearlite morphology. For tensile properties, yield strength was directly proportional to ferrite grain size for 0.4% C steels and to the inverse square root of pearlite interlamellar spacing for 0.6-0.8% C steels. In 0.6% C steels, yield strength decreased linearly with increasing pearlite interlamellar spacing when the hypoeutectoid ferrite present was discontinuous. However, if this ferrite was continuous, yield strength was constant at a low value and independent of lamellar spacing. For 0.6% C steels, ultimate strength was inversely proportional to the pearlite interlamellar spacing. In general, ultimate strength increased with increasing volume fraction of pearlite.

For impact properties, the temperature at which the impact energy was 27.1 J (20 ft-lb_f) increased linearly with volume fraction of pearlite and, for 0.6% C steels, with the pearlite colony size (49).

In addition, the effects of austenitic grain size and grain refining alloy elements on ferrite grain size and pearlite interlamellar spacing and volume fraction and, indirectly, mechanical properties were studied. Vanadium was found to be the most beneficial with regard to effects on mechanical properties (49).

Nolan et al. (50) made similar correlations for high strength pressure vessel steels with structures ranging from untempered martensite to tempered lower bainite. The tempered bainite had the lowest strength and highest ductility, and untempered martensite, the highest

strength and lowest ductility, with both structures having low impact properties. Tempered martensite was the best compromise structure.

From Krauss (51), as carbon content goes from 0.4 to 0.5 percent for steel with ferrite-pearlite microstructures, yield strength increases from 414 MPa (60 ksi) to 434 MPa (63 ksi) or 200 MPa/(percent carbon), whereas for a carbon increase from 0.5 to 0.6 percent, yield strength increases from 545 MPa to 448 MPa (65 ksi) or 140 MPa/(percent carbon). Above 0.6 percent carbon, yield strength decreases slightly. Over the carbon range of 0.4 to 0.6 percent, ultimate strength increases linearly from 670 MPa (100 ksi) to 758 MPa (110 ksi) and changes very little above 0.6 percent carbon. Over the same carbon range, reduction of area (RA) decreases from 44 percent at 0.4 percent carbon at a rate of 30 percent RA/(percent carbon); impact energy also decreases proportionately. In a different study, it was observed that with a transformation temperature of 675°C (1250°F), a carbon increase from 0.4 to 0.6 percent gives an increase of hardness of about 12 R_C points (52). From 0.6 to 0.8 percent carbon, the increase of hardness is 6 R_C points.

The effects of carbon on mechanical properties are highly dependent on the microstructure. For a fully martensitic microstructure in steel with a range of carbon from 0.4 to 0.6 percent, there is an increase of hardness of about 6 R_C points (53). Above 0.6 percent carbon to about 0.8 percent, hardness increases slightly until a maximum of R_C 67 is reached at about eutectoid composition, beyond which, hardness decreases with increasing composition of carbon. For the fully martensitic structure, the rate of increase of yield strength is about 2700 MPa/(percent carbon).

Sato (54) studied the effects of microstructure on fatigue and impact properties of welds in high-carbon (0.68 percent) rail steels. Welds were produced in rail with structures of pearlite and tempered martensite. The pearlitic structure had tensile properties of 456 MPa (66 ksi) yield strength and 848 MPa (123 ksi) ultimate strength compared to strengths of 767 MPa (111 ksi) and 1099 MPa (159 ksi) in the martensitic condition. Reductions of area were 23 and 49 percent respectively. Welds were of the enclosed arc variety using low carbon (0.06 percent) Cr-Mo-Ni rods. Since fatigue strength varies with hardness and ultimate strength which, in turn, vary across the weld deposit, a correlation was observed between fatigue strength and ultimate strength as a function of position in the weld. Fatigue strength was obtained from smooth rotating bend specimens, in which a fatigue limit of 0.37 of the ultimate strength was observed for the pearlitic material and 0.39 for the martensitic. These fatigue limits correspond to ferrite-pearlite structures with the higher fatigue limit material having a finer structure. For notched rotating-bend specimens, fatigue limit was constant and independent of ultimate strength.

Sato (54) also observed, in all cases, that the fatigue limit of the region of highest hardness, the fusion zone, was about 10 percent less than for any other region of the welds. This was attributed to the precipitation of coarse proeutectoid ferrite at the fusion zone. In welds of a tempered martensite structure, tensile strength and fatigue strength were superior to those in pearlitic structures, and again, the fusion zone had the lowest fatigue limit. Tempered martensite and

fine pearlite resulting from fine prior austenite grains displayed impact properties which were superior to coarse pearlite. The welds in the parent structure of tempered martensite displayed the former structures, thus accounting for their overall superior properties. Proeutoid ferrite at prior austenite grain boundaries deteriorated impact properties in all cases.

Houin et al. (55) found similar correlations between carbon composition and pearlite structure and how they, in turn, influence mechanical properties. After austenitizing samples at 850-900°C and cooling at various rates, it was determined that the tensile properties of pearlite depend primarily on carbon content and interlamellar spacing as controlled by the cooling rate. For carbon contents less than 0.6 percent, pearlite was always fragmented, which gives low yield strength but good reduction of area. For a carbon content of about 0.6 percent, a fine fragmented pearlite structure could be obtained by heat treatment. This leads to both high yield strength and reduction of area. For 0.8 percent carbon, pearlites were always of the normal continuous lamellae type for which yield strength increased as interlamellar spacing decreased but reduction of area was unaffected.

George et al. (56) states that the most important factor in controlling the properties of ferrite-pearlite steels is grain size because, as grain size is reduced, both yield strength and impact properties increase. One of the simplest means of obtaining grain refinement is by austenitizing and cooling at moderate rates, i.e., by normalizing. If grain refinement is combined with precipitation hardening, even higher yield properties are obtained. The most commonly used

precipitation hardening elements are niobium and vanadium. As precipitation hardening is increased, impact transition temperature increased; thus can be largely overcome by grain refinement. However, improper refinement can destroy the precipitation hardening effect by coarsening of the precipitates. The precipitation hardening and grain refinement become interactive in that austenite grain boundaries can be pinned by the fine precipitate particles. This is the basis for normalized fine grained steels. George et al. (56) concluded that an optimum combination of yield strength, ductility and impact properties could be obtained in normalized steels of ferrite-pearlite structures, by proper control of grain refining (and precipitation hardening) elements such as Al, Nb, Ti and V.

The effects of small amounts of vanadium, niobium and other microalloy elements on the mechanical properties of carbon steels were quantified by Pickering (57). For low to medium carbon steels with ferrite-pearlite structures, the addition of small amounts of vanadium as a carbide can produce an average increase in yield strength of 500 MPa (72 ksi)/percent and three times this rate as a nitride. For niobium as a carbonitride and titanium as a carbide, the effect is the same as for vanadium nitride, 1500 MPa (217 ksi)/percent.

Pickering (57) also discussed the effects of elements which are not considered to be microalloy elements. The effects of Ni and Cr essentially cancel each other, nickel results in an increase in yield of about 33 MPa (5 ksi)/percent, while chromium decreases yield at this rate. Manganese and copper produce the same effect as nickel, while silicon has about three times its effect and molybdenum about half.

Manning et al. (52) have determined the effects of several of these elements on the hardness of carbon steels with a ferrite-pearlite structure. For a transformation temperature of 595°C (1100°F), up to 0.1 percent V results in a hardness increase rate of 100 points R_c /percent; up to 0.5 percent Cu produces an increase rate of 2 points R_c /percent; up to 1.0 percent Ni produces the same effect as Cu; up to 1.0 percent Cr results in an increase rate of 4 points R_c /percent; and Mo, up to 0.2 percent has virtually no effect on hardness.

The effects of these elements, including carbon, on hardness are sensitive to the transformation temperature. As this temperature is lowered, these effects become less pronounced.

Pickering (58) attempted to quantify the effects of microstructure and inclusion content on the mechanical properties of HSLA steels. For HSLA steels, the fraction of pearlite, over a limited range, does not affect the yield strength, but does increase the flow stress (58). Grain refinement (fine ferrite grains and pearlite colonies), low silicon and free nitrogen optimize impact properties (58, 59, 62). Also, oxides and other nonmetallic inclusions should be minimized (58, 28). The length to width ratio of inclusions influences the isotropy of the material, with spherical particles resulting in the most nearly isotropic properties. However, the spherical shape usually reduces properties as compared to elongated inclusions with respect to the elongation direction. Also, since carbides can promote the propagation of cleavage cracks through ferrite, as carbide content and size is increased, an adverse effect on impact energy and an increase in the impact transition temperature may occur (58, 63). Subcritical stress

relieving may promote the formation of coarse carbide filaments by the degeneration of pearlite, particularly in low-carbon, low-manganese steels and actually reduce impact properties.

For a low-carbon, low-manganese steel, Pickering (58) observed an 80°C increase in the impact transition temperature for an increase in carbide filament size from 2 μ and 3-4 μ . In a quenched and tempered structure, as the carbide volume fraction increased from 0.01 to 0.10, the true strain at fracture decreased from 1.9 to 0.9 (58). In quenched and lightly-tempered steels, carbides can precipitate as platelets at prior austenitic grain boundaries and lower the fatigue strength. Lue and LeMay (64) noted this effect in AISI 4140 steel.

Acicular ferrite is a microstructural constituent which correlates with high strength and toughness in HSLA steels and with a high resistance to cleavage fracture of weld deposits in low-alloy steel (65, 66). Abson et al. (65) confirmed that inclusions in weld metal strongly influence the nucleation of ferrite from austenite and determine the extent of the desirable acicular ferrite. The inclusions not only serve as nucleation sites for ferrite at austenite boundaries, but also nucleation sites of acicular ferrite within the austenite grains. It was noted that a decrease of oxygen in the weld from 0.02 to 0.01 percent (i.e., a reduction in the number of inclusions), virtually eliminated the nucleation of acicular ferrite and resulted in a bainitic structure which was more brittle (65). On the other hand, an increase in oxygen from 0.03 to 0.06 percent resulted in predominantly side-plate structures with little or no acicular ferrite. In contrast, with 0.06 percent oxygen in a deposit produced under an alumina based flux,

the structure was substantially acicular ferrite. Changes in sulfur content only changed the microstructure slightly as compared to changes in oxygen. It was concluded that there is an optimum level of oxygen and, to a lesser extent, sulfur, and hence a volume fraction of inclusions, that results in the acicular ferrite structure.

Baker and Johnson (67) found that in the overheating of HSLA steels, sulfur content (MnS inclusions) has little effect on fracture toughness. However, overheating may have an adverse effect on fatigue behavior under high strain conditions as a function of sulfur content. In steels of high sulfur content, "burning" of the sulfur may occur during overheating, which can lead to a marked decrease in fracture toughness, particularly if the sulfur is concentrated at grain boundaries.

Karitonov et al. (68) found that the addition of small amounts of sodium chloride significantly lowered the gas and inclusion content of low to medium carbon, low alloy, steel castings. The additions of sodium chloride also refined the grain structure and increased the amount of pearlite. The net effect was an increase in mechanical properties, most noticeably the impact energy.

It is also known that the impact properties of castings are improved by additions of calcium silicide, rare earth metals and aluminum (69). The former spheroidize inclusions, and the aluminum is a deoxidant. Titarenka and Shalomeev (69) found that barium and strontium silicides produce the same effect as calcium silicide and rare earth metals. When these silicides are used in correct proportions with

aluminum, the low temperature impact properties of steel castings are noticeably improved.

Aleksandrov (70) found that similar results are obtained for welds when Ca, Zr, Ce and other rare earth metals are introduced into the weld metal. It was noted that calcium must be introduced in the form of a "silico-calcium" ferroalloy (Ca, Si, Al and Fe) to produce a noticeable improvement in the low temperature impact strength of the deposit.

In a related study, Ershov et al. (71) determined that the size of AlN, TiN, and ZrN inclusions in steel castings could be reduced by increased cooling rates during solidification. The sizes of the TiN and ZrN inclusions were most affected by varying the cooling rate with AlN least affected.

Filtering of the molten metal with ceramic filters has also been used with success in the superalloy industry to improve the properties of casting by reducing the number and sizes of primary inclusions (72).

2.6 Residual Stresses in Welds

During welding, the weld metal and the HAZ are at temperatures substantially above that of the unaffected parent metal (14). The areas of the weld which solidify first are weak and can exert little stress; however, as cooling and shrinkage progress, increasing stress is exerted on the weld metal and can reach the yield strength of the base metal and HAZ (14, 73). Since the region that solidifies first shrinks more rapidly than surrounding areas, it is typically placed in a state of residual tensile stress, and the regions that solidify last are under

compressive stress. The maximum (absolute) residual stresses occur in the region of the weld metal and HAZ (35). In addition to solidification and cooling effects, residual stresses may be produced in steel welds at relatively low temperatures by the martensitic transformation since it involves an increase in specific volume.

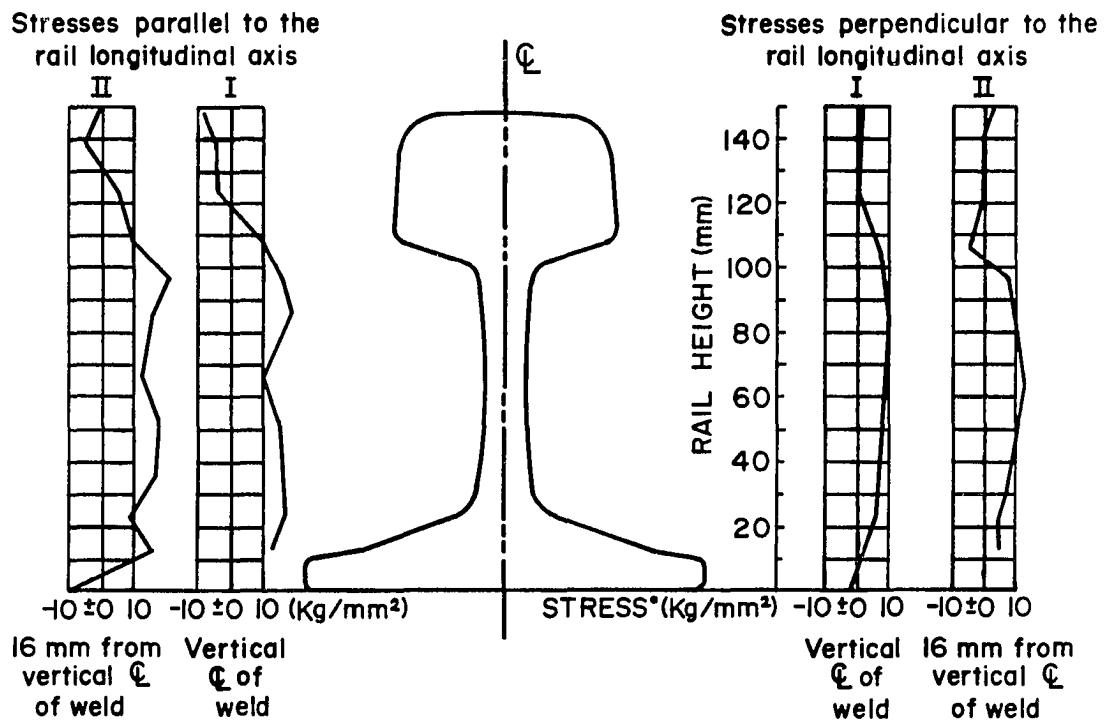
The residual stress state can vary from uniaxial to triaxial depending on the weld geometry and complexity (14, 73, 74). In most cases, the residual stresses are deleterious. For example, residual stresses in weldments may produce distortion, and they can cause premature weld fatigue either through the promotion of brittle fracture or the initiation and propagation of fatigue cracks during service loading (14, 73, 74). In addition, residual stresses may contribute to the corrosion failure of welds (14).

A beneficial effect of residual stresses was observed by Kapadia and Imhoff (75) who conducted linear elastic fracture mechanics (LEFM) studies of electroslag welds of A-36 and A-588 steels. They found that the crack growth rates in the weld metal were similar to or up to five times slower than in the parent steels. This retardation effect was most pronounced at low stress intensity ranges and was significantly greater in the coarse grained region of the HAZ and in the fusion zone as compared to the weld metal. It was noted that marked variations in microstructure of the HAZ and weld metal did not significantly affect growth rates in these respective regions; however, they did affect the topography of the fracture surface. In a separate study, Kapadia (76) attributed the retardation effects to residual compressive stresses in the HAZ and in the fusion zone. He concluded that the benefit of these

stresses would diminish under service conditions of high tensile mean loading or after a postweld stress-relief heat treatment.

In a study by Dohse (77), the residual stresses in nonwelded rails (50 kg/m) and in thermite welded rails (with and without vertical reinforcing ribs) were determined. He noted that the stress pattern in nonwelded rail was tensile in the head and base with compressive stresses in the web. This pattern was reversed in thermite welds of the rails. No significant difference was noted between welds with and without the reinforcing ribs. For the nonwelded rail (rail height -152.4 mm), the maximum longitudinal stresses were +83 MPa (+12 ksi) in the web 105 mm from the base. For the thermite welds, typical residual stresses were as shown in Figure 1.

Along the weld centerline, the average of the maximum longitudinal stresses were -108 MPa (-16 ksi) on the top of the head, -98 MPa (-14 ksi) on the underside of the base and +206 MPa (+30 ksi) in the web 60 mm (reinforcing ribs) and 85 mm (without ribs) from the base. The vertical residual stresses were a maximum of +196 to +254 MPa (28 to 37 ksi) at the web-weld center. The longitudinal stresses decreased slowly with distance from the weld, whereas the vertical stresses were completely relieved at 80 mm from the weld center. The vertical residual tensile stresses were considered to be insignificant due to the high compressive service loads. Dohse (77) concluded that the weld residual stress pattern is actually of benefit in service since the base, which is subject to tensile service stress, is prestressed in compression. Heller and Beck (26) confirmed Dohse's findings in a later study. It appears, however, that residual stresses in the HAZs of these welds



• 1.42 Ksi/Kg/mm², 9.807 MPa/Kg/mm²

— Pattern of residual stresses that existed in the weld
(from measurements after complete residual stress relaxation)

Figure 1: Residual stresses in a nonreinforced thermite rail weld; weld gap - 24 mm, 50 kg/m rail. From Dohse (77).

were not investigated. Thus, the benefit offered may be negated by detrimental HAZ stress fields.

Krauss (78) determined the residual stress levels in an EFB weld of head-hardened rail, 68 Kg/m, (136 lb/yd), that had been subjected to 1.2 GN (135 million gross tons) of service loading. His findings agree with Dohse; the base and head area of the weld are in compression while the web is in tension. Measurements taken approximately 3.6 cm from the weld vertical centerline indicate this area follows the weld stress pattern; however, at about 7.3 cm from the weld center, the head and web residual stresses vary from about zero to compressive regardless of orientation. Longitudinal stresses at about 8.1 cm above the base were +416 MPa (+60 ksi) at the weld centerline, +256 MPa (+37 ksi) psi at 3.6 cm from the weld center and -1 MPa (-0.2 ksi) at 7.3 cm from the weld center. Corresponding vertical stresses were +281 MPa (+41 ksi), +123 MPa (+18 ksi) and -6 MPa (-1 ksi), respectively.

3. EXPERIMENTAL PROCEDURES

3.1 Rail Welds

Fourteen thermite welds were produced according to standard practice at the DOT-FAST facility in Pueblo, CO. A thorough analysis of these welds, which included mechanical properties, macrostructures and microstructures, residual stresses and thermal history during the welding cycle, was conducted. The fourteen test welds were produced according to the test matrix outlined in Table 2, using the rail and weld metallurgies of Table 3. The welds all employed the Orgotherm SKV process in which two lengths of 68 kg/m (136 lb/yd) rail, (each of 1.2 m (4 ft.) length), were welded with a gap of 24 mm (15/16 in.). As indicated in Table 2, the test variables were rail and weld chemistries, rail preheat time and postweld condition. All other procedures were the same as applied in the field (79). The mold configuration and the flow pattern of the molten steel are shown in Figure 2.

In welds 1 through 4, fifteen thermocouples were placed in one rail, according to Figure 3. Thermocouples 1-5 in weld 4 were type 'S' (AWG 30) in alumina tubing; all others were type 'K' (AWG 20) in a glass-fiber insulation. After the production of weld 4, the first for which thermal data were recorded, it was determined that type 'K' thermocouples were adequate to withstand the peak temperatures, and these were used exclusively thereafter.

For weld 9, three thermocouples were placed in the center of the weld gap by means of holes bored in one mold half. These locations were

Table 2. Experimental Conditions for Rail Welds

Weld Number	Rail Type		Thermite Portion Type		Preheat Time (s)		Tap Time (s) Δ	With muffle	Cooling		Thermal Data Recorded
	A	B	Alloy	St'd	St'd	Long			Without muffle		
1	Cr	CrMo	X		120		25	X			X
2	Cr	CrMo	X		124		27			X	X
3	Cr	CrMo	X			184	23	X			X
4	St'd	CrV		X	128		25	X			X
5	St'd	CrV		X	120		24			X	
6	St'd	CrV		X		180	25	X			
7	CrMo	HH		X	120		21	X			
8	CrMo	HH		X	131		21			X	
9	Cr	CrV	X		125		25	*			X
10	Cr	CrV	X			180	22			X	

Δ Tolerance on automatic tap time: 18-28 s.

* Weld 9 cooled with the mold left in place.

Table 2--Continued

Weld Number	Rail Type		Thermite Portion Type		Preheat Time (s)		Tap Time (s) Δ	With muffle	Cooling		Thermal Data Recorded
	A	B	Alloy	St'd	St'd	Long			Without muffle		
11	St'd	St'd		X	120		24			X	
12	CrMo	CrMo	X		124		12+	X			
13	CrMo	CrMo	X		121		24			X	
14	CrMo	CrMo	X			183	24	X			

Δ Tolerance on automatic tap time: 18-28 s.
+ Premature tap.

Table 3. Nominal Composition of Rails and of Weld Metal

Element	CrMo*	Cr*	Rails CrV*	St'd. & HH**	Thermite Weld Metal Alloy+	St'd.+
C	0.70-0.80	0.73	0.72	0.69-0.82	0.61	0.53
Mn	0.50-0.70	1.20	1.27	0.70-1.00	1.47	1.28
P	0.030 max	0.023	0.014	0.04 max	--	0.036
S	0.025 max	0.026	0.03	0.05 max	--	0.019
Si	0.20-0.25	0.30	0.22	0.10-0.25	0.17	0.13
Cr	0.50-0.70	1.25	1.04	--	0.08	0.05
Mo	0.16-0.20	--	--	--	--	--
V	--	--	0.087	--	0.10	0.065
Ti	--	--	--	--	0.02	0.025
Al	--	--	--	--	0.36	0.48
Ni	--	--	--	--	--	<0.01
Cu	--	--	--	--	--	0.06

Weight percent, w/o

* CrMo, Cr and CrV rails from Reference 80.

** Standard (St'd.) and head-hardened (HH) from Reference 81.

+ From Reference 82.

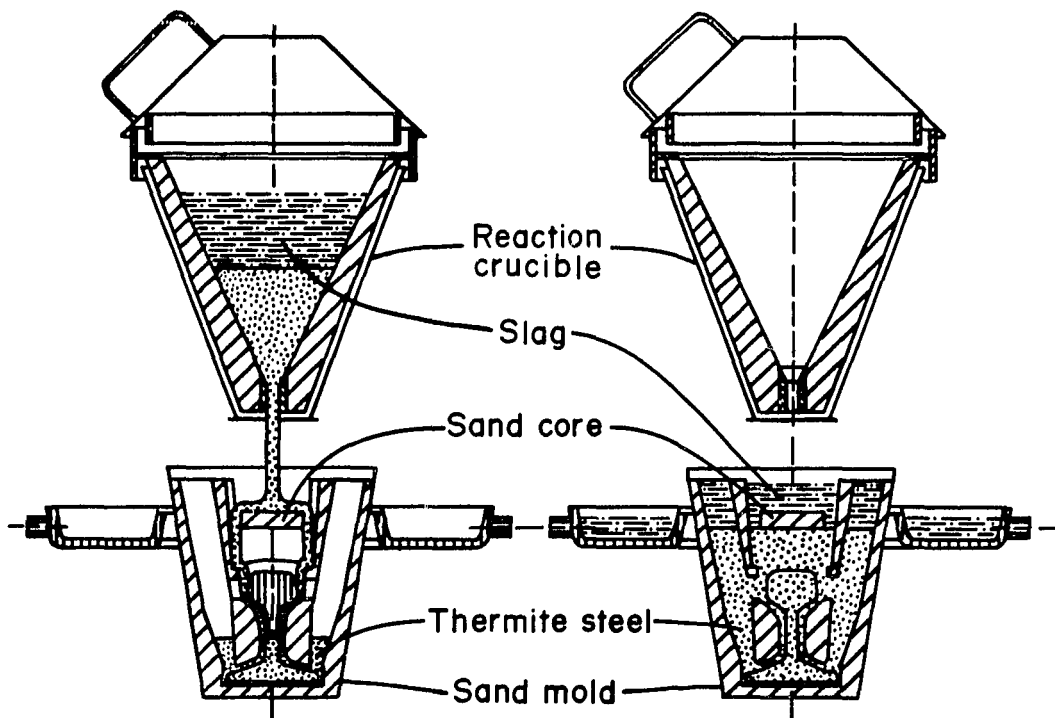


Figure 2: Mold configuration and flow pattern of the molten steel for the thermite rail welds.

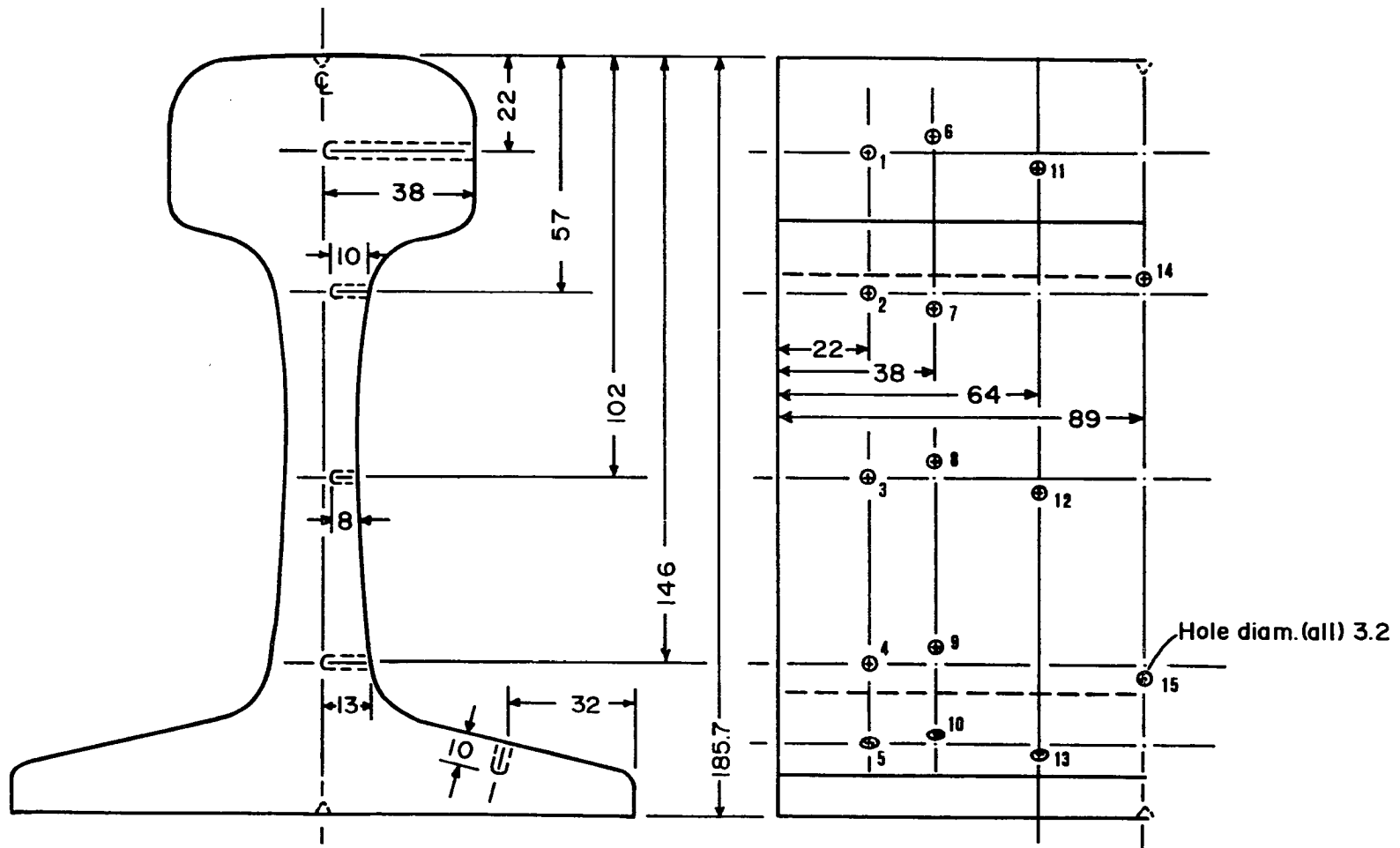


Figure 3: Thermocouple locations for welds 1, 2 and 4. For weld 3, all thermocouples were 3 mm closer to the rail end. Numbers identify the thermocouples and the dimensions are in mm. The rail is 68 kg/m (136 lb/yd RE).

approximately in the head, the web and the base, as shown in Figure 4. The thermocouples were made from tungsten-rhenium (5 percent vs 26 percent Re) wires (AWG 24) that had been sealed from the atmosphere in alumina tubing while in argon. Additional protection was provided by sheathing them in closed-end quartz tubes, which were inserted through the holes in the mold.

Thermal data were recorded by means of a 'Datalogger' data acquisition system. In addition, the output from thermocouples 1-5 in welds 1-5 were simultaneously recorded on a 'Brush 481' stripchart recorder to provide a check of the data. The outputs of the three thermocouples in the weld metal of weld 9 were simultaneously recorded by both units. The time to read all thermocouples once for the Datalogger was 7-8 seconds for welds 1-4 and 2-3 seconds for weld 9. The stripchart provided a continuous record. For all welds, thermal data were recorded at the start of preheat and continued for about 1.5 hours after weld completion.

Preheat was done with an oxy-propane torch with a reducing flame according to the standard practice for making thermite welds in rails. The 'muffle' referred to in the experimental schedule, Table 2, was a clamshell box about 30 cm (12 in.) in length, which was insulated with about 2.5 cm (1 in.) of fiber insulation in the top and sides. The bottom of the muffle, which locked the unit in place, did not contain insulation. The muffle was contoured to fit the rail profile, and was placed over the hot weld immediately after the sprue and risers were removed, and the weld was ground. The purpose of the muffle was to retard the cooling rate of the weld.

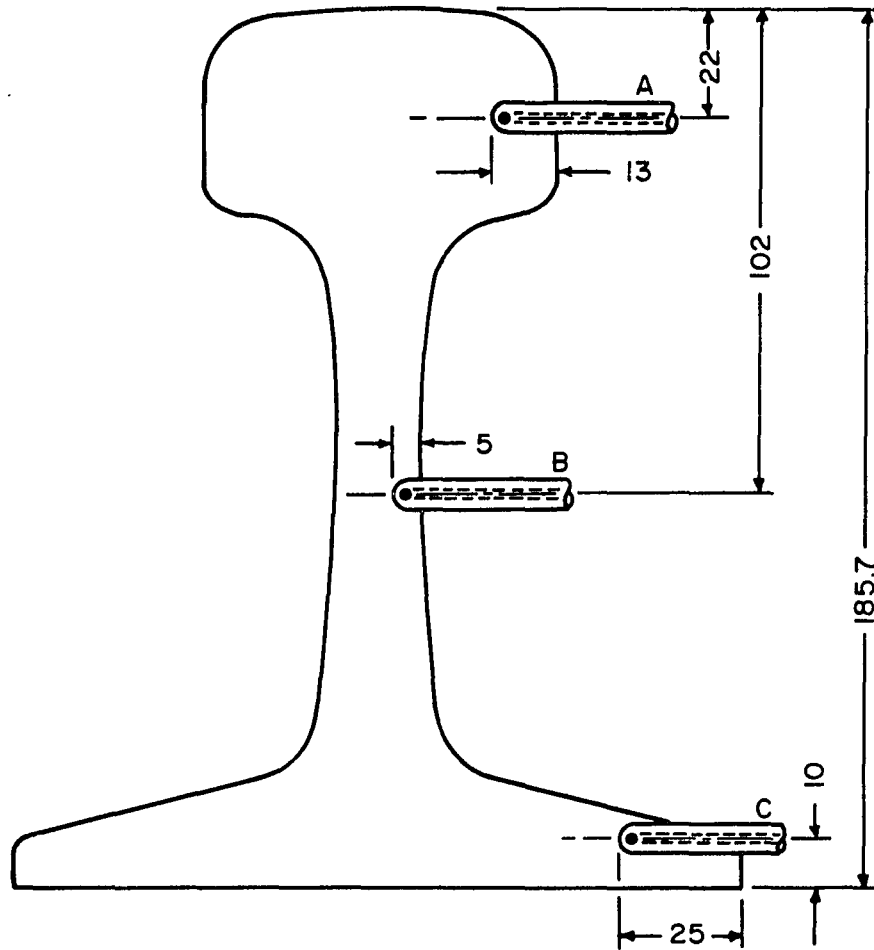


Figure 4: Locations of thermocouples in the weld metal of weld 9. Thermocouples were centered longitudinally in the 24 mm gap. A-Head, B-Web, C-Base. Dimensions in mm.

All completed welds were cut to a length of 30 cm (12 in.) with the weld metal centered. With the exception of weld 11, these lengths were sectioned longitudinally to provide a full-depth macroetch. The sections were etched in a boiling solution of 1 part of concentrated hydrochloric acid to 1 part of water, for approximately 45 minutes.

Rockwell 'C' hardness profiles were determined for planes which went across the welds, 2.5 cm (1 in.) below the running surface of the center of the head, as indicated in Figure 5. These profiles extended a minimum of 7.6 cm (3 in.) in both directions from the center of the weld metal until the original hardness of the rail material was encountered.

Tensile test bars and Charpy V-notch specimens were removed from the locations shown in Figure 5. Tensile specimens had a diameter of 0.64 cm (0.25 in.) and a gage length of 2.5 cm (1 in.). The Charpy V-notch specimens were standard size according to ASTM specifications. Note that the specimens in the HAZ of the welds straddle the narrow soft region of the HAZ and, as a result, contain a hardness and a structure gradient.

Specimens for microstructural analyses were taken at essentially the same location as the Rockwell hardness profile; refer to Figure 5. Two samples, each 7.6 cm (3 in.) in length, were taken from each weld. Each sample contained the structure gradient from the center of the weld metal to the unaffected rail. Specimens were prepared using standard metallagraphic procedures and etched with a 1:1 solution of 2 percent Picral. This was followed by vapor deposition of a carbon layer and then a gold layer. Microstructures were examined in an ISI model IIIA

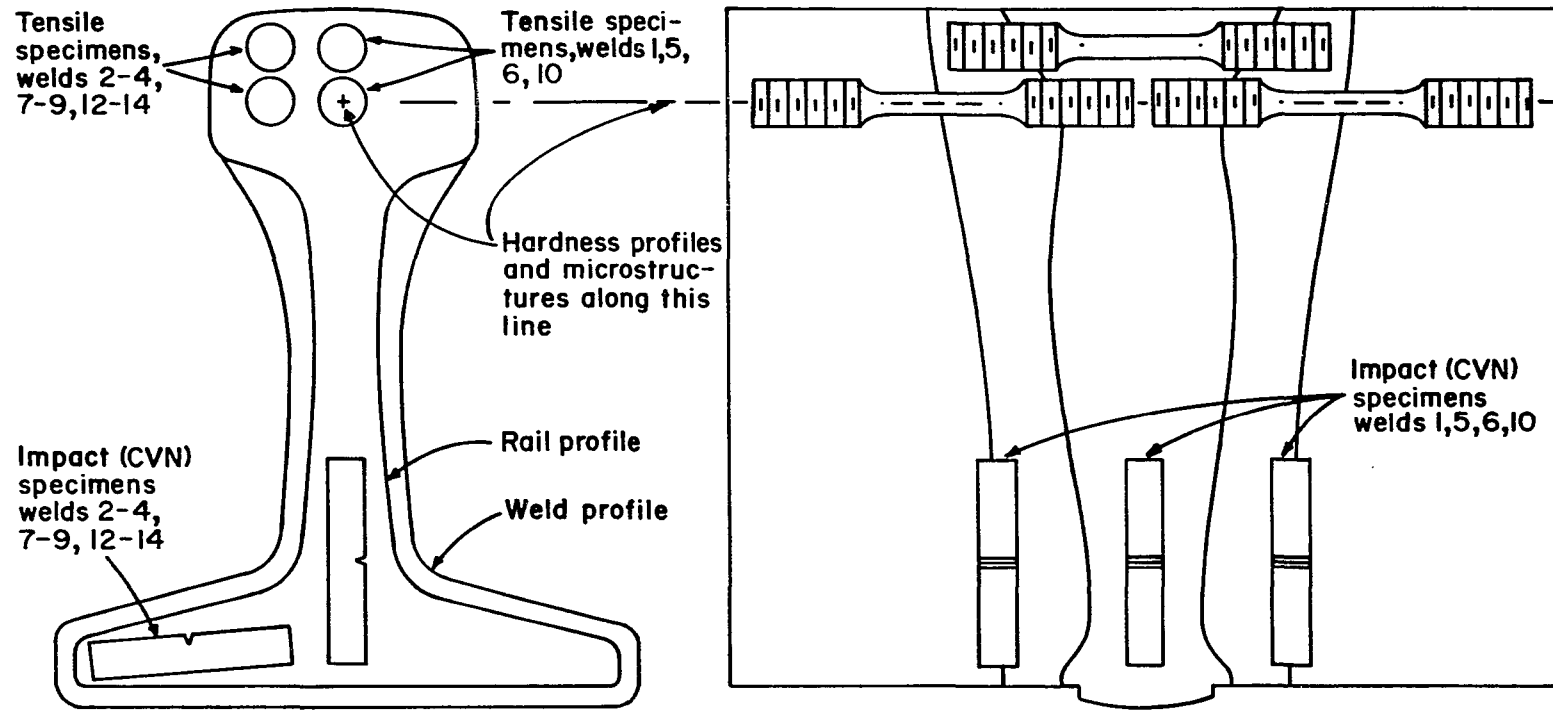


Figure 5: Locations of tensile and impact specimens, hardness profiles and microstructure specimens in welds. Fusion zones and outer edges of the HAZs are indicated.

scanning electron microscope (SEM) equipped with a PGT-System III energy dispersive spectroscopy (EDS) analyzer.

The SEM was also used to examine the fractured surfaces of all tensile and impact specimens. Elemental analyses were done on several inclusions, and unusual surface features which were encountered while viewing the fractures and microstructure samples.

Finally, several samples of weld metal from the location of the microstructural specimens were quantitatively analyzed for inclusions in a quantitative image analyzer. These analyses were on weld metal specimens which were carefully prepared to preserve the inclusions. Each field of view was an area of 0.26 mm^2 , examined at a magnification of 400X. Size distribution and volume fraction of inclusions were determined for welds 5-7 and 12-14. Ten fields of view were selected at random and evaluated for each specimen. Fields containing obvious microporosity were purposely avoided.

Residual stresses, as a result of welding, were measured in weld 11, which was left intact for this purpose. Measurements were taken at various locations in the weld metal and the HAZ, as shown in Figure 6. The blind-hole technique was employed using rosette strain gages (Micro-Measurements EA-06-062RE-102), designed for this purpose (83).

Each of the three elements of a rosette was made the active element of a quarter-bridge circuit. Each gage required three leads of copper wire, 1.2 m (48 in.) in length and AWG 16, which were twisted together to reduce interference. Two leads were attached to the same end of the active element and to the signal input and internal dummy gage of a nullmeter and switching unit. The third lead, connected to

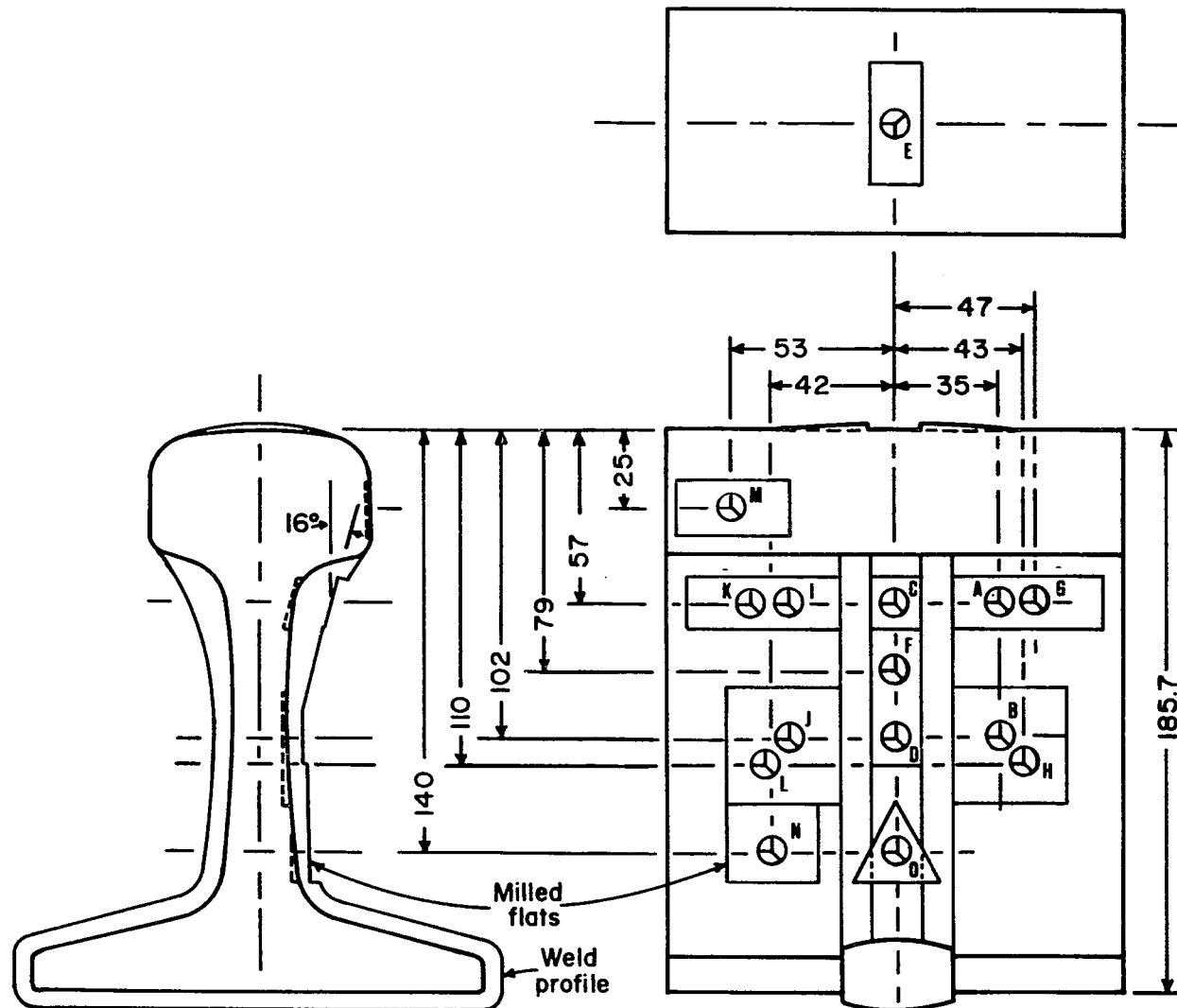


Figure 6: Locations of strain gage rosettes for residual stress measurements. Letters identify locations and the dimensions are in mm.

the excitation potential, completed the active element circuit. Thermal drift was not observed after gage attachment.

After setup and nulling of the gages, a 1.6 mm (0.062 in.) dia. hole was bored in the center of the rosette, and the changes in the three gage readings were recorded to determine the residual stresses in the immediate vicinity of the rosette. Virtually complete stress relief occurs at a hole depth/diameter ratio of 1 (83). The holes were bored accordingly for all rosettes, and then rebored to increase the ratio to 1.5 and the gage values recorded to determine if stress gradients normal to the surface existed. No significant changes were observed.

The boring of flat-bottom holes was accomplished with an end mill which was centered over the rosette by using a centering scope. Thermal drift due to localized heating from boring was checked by reading the gages immediately after boring and then checking for a change in the readings with time. In no case was drift observed.

3.2 Plate Welds

Following the analyses of the fourteen rail welds, a series of nine plate welds were produced with the objective of improving weld properties. For these welds, plates of hot-rolled AISI 1080 steel were welded according to the conditions given in Table 4. The plates had a cross-section of 25 mm x 76 mm and a length of 152 mm; two pairs of these plates were inserted into a silica-sand mold, Figure 7. The molds were produced from sand with an AFS grain number of 30/50, which was mulled with 4 wt pct. of 2.4:1 ($\text{SiO}_2:\text{Na}_2\text{O}$) sodium silicate. The molds

Table 4. Experimental Conditions for Plate Welds

Weld	Tap Time (s)	Weld gap (mm)		Filter System+
		Bottom	Top	
1-X, 2-X	21	38 25	25 38	None
3-X, 4-X	25	38 25	25 38	Filter A in sprue
5-X, 6-X	61*	25-no taper 25-no taper		Filter A in sprue and in base of 6-X
7-X, 8-X	23	25-no taper 25-no taper		Filters B, A and B in sprue; preheated to 2000°C
9-X, 9-XI	20	25-no taper **		Filter A, 13 mm of beads, and filter B in sprue; preheated to 2000°C

+ Filters A and B were 51 mm x 51 mm x 13 mm thick. Filter A is a mesh of 1.3 mm square openings with 41 openings per cm². Filter B is a mesh with 0.96 mm square openings with 64 openings per cm².

* Manual tap; all others were self-tapping.

** 9-XI was an ingot with dimensions of 2.5 cm x 2.5 cm x 7.6 cm in place of the weld.

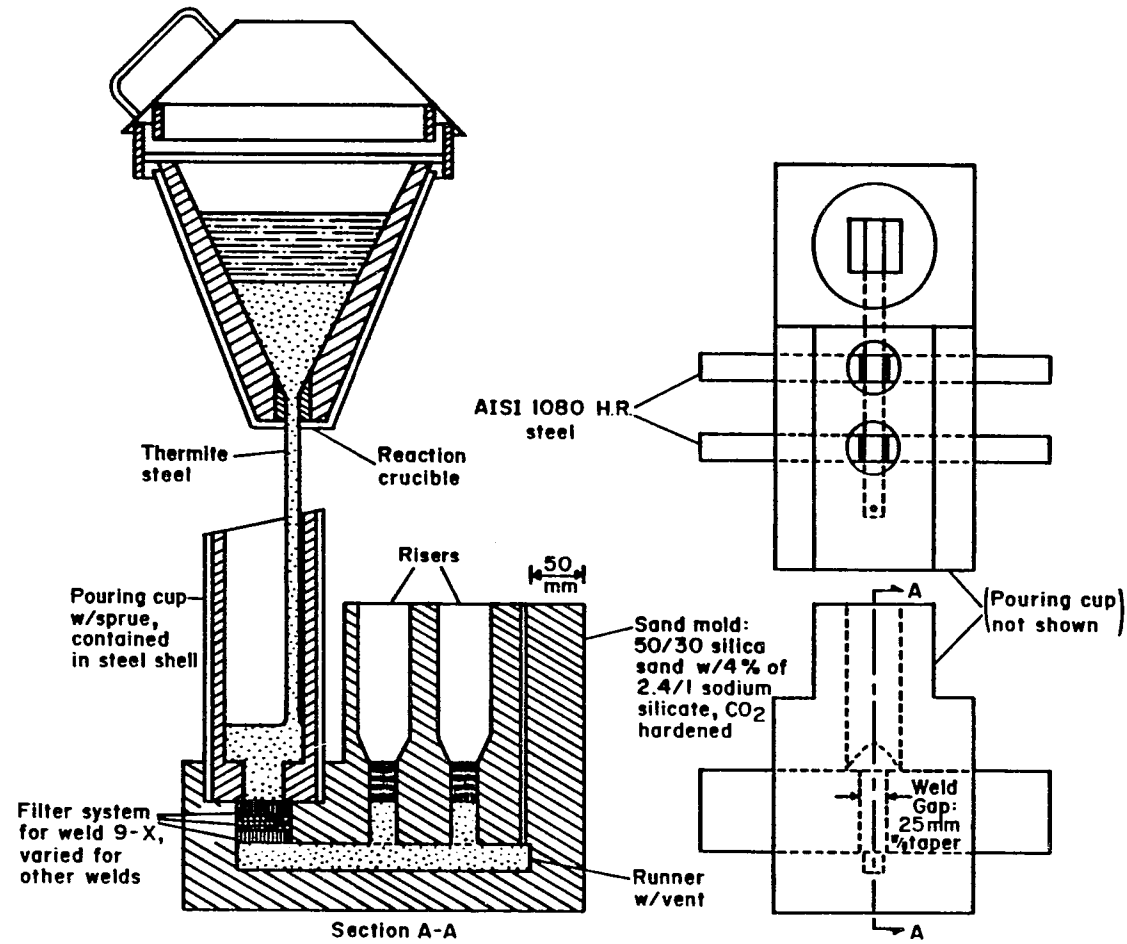


Figure 7: Mold configuration and steel flow pattern for plate welds.

were hardened with carbon dioxide for about 60 s, as in the so-called "CO₂ process" for producing metal castings.

Figure 7 shows a weld gap of 25 mm, which was employed for some welds, but not all. The remaining welds had a tapered gap with a width which was varied from 25 mm to 38 mm, as indicated in Table 4. With the exceptions of welds 1-X and 2-X, the molds were produced with ceramic filters, as attempts to reduce the sizes and volume fraction of inclusions in the weld metal. The filter systems consisted of various combinations of two different meshes of zirconia-24 wt. pct. mullite filters and zirconia beads with diameters in the range of 1.6-2.3 mm, produced by Corning.

To produce the welds, the reaction crucible used was the same as used in thermite welding of rail. Weld metal of standard composition was produced by the Orgotherm SKV process, which provided enough steel to fill the runner, the two weld gaps and the two risers for the mold, as shown in Figure 7.

The plate welds were sectioned and macroetched, according to the same procedure applied to the rail welds. Hardness profiles were taken across the weld metal and both HAZs at 13 mm below the top of the weld. Tensile bars were removed from each weld at the location of the hardness profiles and across the weld metal.

Based on the results of the tensile tests, representative weld fractures and microstructures were studied using the SEM. The welds were also quantitatively evaluated for inclusions by means of Quantimet analyses, provided through the courtesy of IBM in Tucson.

In order to study the effects of normalizing, preliminary heat treatments were performed on blanks removed from the runners. These blanks were austenitized at 870°C for 30-40 minutes and cooled through the transformation range (1000°K to 810°K) at various rates.

The austenitizing temperature was chosen by consulting the Steel Castings Handbook (84). Optimum time at the austenitizing temperature was determined by holding samples from welds 1-X and 2-X for various time and brine quenching. Hardness and microstructure were checked for evidence of complete transformation to austenite, i.e., a fully martensitic structure. In this case, it was determined that complete transformation had occurred after 20 minutes and that there was no further change in microstructure or hardness between 20 minutes and 45 minutes.

To measure the cooling rates from the austenitizing temperature, type 'K' thermocouples were inserted in axial holes, which ran to the midlength of the blanks. The blanks were cooled in various environments; in the order of increasing cooling rate, these included silica sand at 870°C, a reflective enclosure, still ambient air and forced air. This procedure was quantified by measuring the various cooling rates with the thermocouple inserted into the blanks. From the standpoint of heat transfer, the tensile-bar blanks, which were normalized, had cooling rates equivalent to the cooling rate samples, depending on the method of cooling from the austenitizing temperatures.

Microstructures, hardness, tensile properties and fracture modes for normalized specimens of weld metal were evaluated for various cooling rates.

4. RESULTS AND DISCUSSION

4.1 Mechanical Properties of the Rail Welds

4.1.1 Hardness Profiles. Hardness measurements were taken across both heat affected zones and the weld metal of thirteen of the welds; weld 11 was excluded from this study. The data are shown in Figures 8-11 and Table 5. Nominal chemistries of the weld metal and of the rails for the welds are given in Table 3.

Figure 8 presents the hardness profiles of welds 1, 4 and 7, which are between two alloy rails, a standard and an alloy rail, and a head-hardened and an alloy rail, respectively. In all cases, except for the head-hardened (HH) rail of weld 7, the maximum hardness is observed in the HAZ and often just beyond the edge of the fusion zone. In all welds, minimum hardness is at the outer edge of the HAZ. The profiles for welds 1 and 4 are typical for all welds between alloy rails and between a standard rail and an alloy rail. However, the hardness profile for weld 7 is atypical because of the region of low hardness in the HAZ and adjacent to the fusion zone in the head-hardened rail. This was the only weld which exhibited this behavior and may be due to the heating and cooling effect of welding on the case-hardening imparted to the head of the rail. Specifically, the irregularity in the shape of the hardness profile is possibly the result of a mixed structure. The HH rail is AREA standard rail (American Railway Engineering Association) in which the head has been induction heat treated. The depth of this "cap" terminates at 12 to 15 mm below the running-surface and is

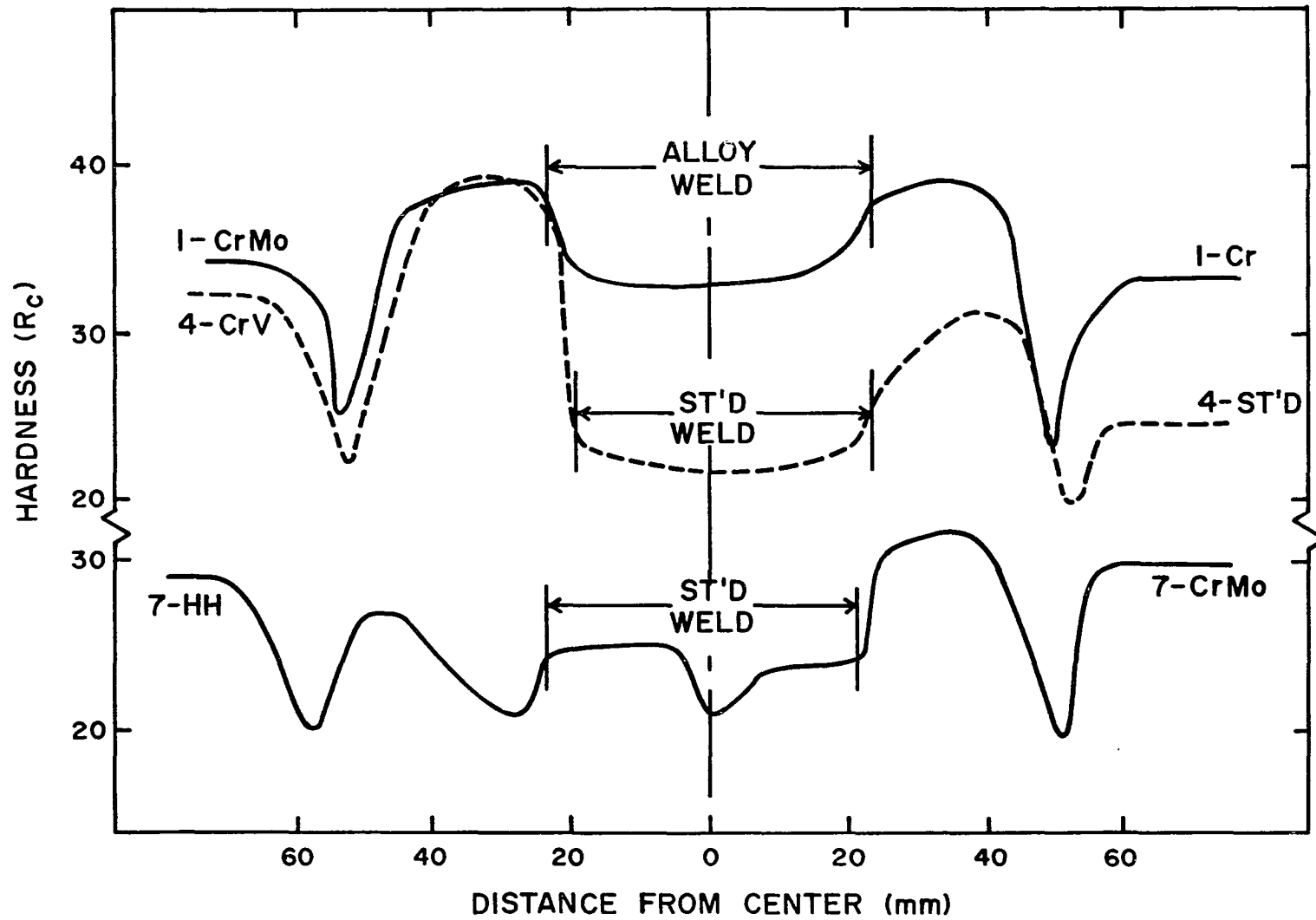


Figure 8: Hardness profiles of welds 1, 4 and 7.

primarily a very fine pearlitic structure with possibly some bainite. Underlying the cap, the structure may not have been completely transformed to austenite during the welding process, and the result is a mixed structure with hard and soft spots. The hardness profile, at 25 mm below the running-surface, probably represents this region. In any case, the microstructures observed at this location were not uniform.

Figures 9 and 10 summarize the range of hardness deviations observed in the heat-affected zones of the five types of rails. No effect of preheat time on hardness and only a slight effect of the application of the muffle to retard cooling on hardness was observed; thus, the data are presented as a range of hardness for a given type of rail. All of the heat-affected zones are included in Figures 9 and 10, except the HAZ of the CrMo side of weld 7. For an unknown reason, this particular rail did not respond to the welding process in a manner similar to the twenty alloy welds represented in Figure 9.

The hardnesses for the heat-affected zones are summarized in Table 5. From these data, it appears that the effect of retarding cooling by application of the muffle is to decrease the maximum hardness by approximately 1-3 R_C points in the alloy rails. However, it is difficult to make any statement regarding the effect of the muffle on the hardness in the standard and in the head-hardened rails because of the small number of experiments with these rails.

Figure 11 summarizes the hardness of the weld metal in the thirteen welds for which hardness profiles were measured. The most noticeable effect is that weld metal produced from so-called "alloy"

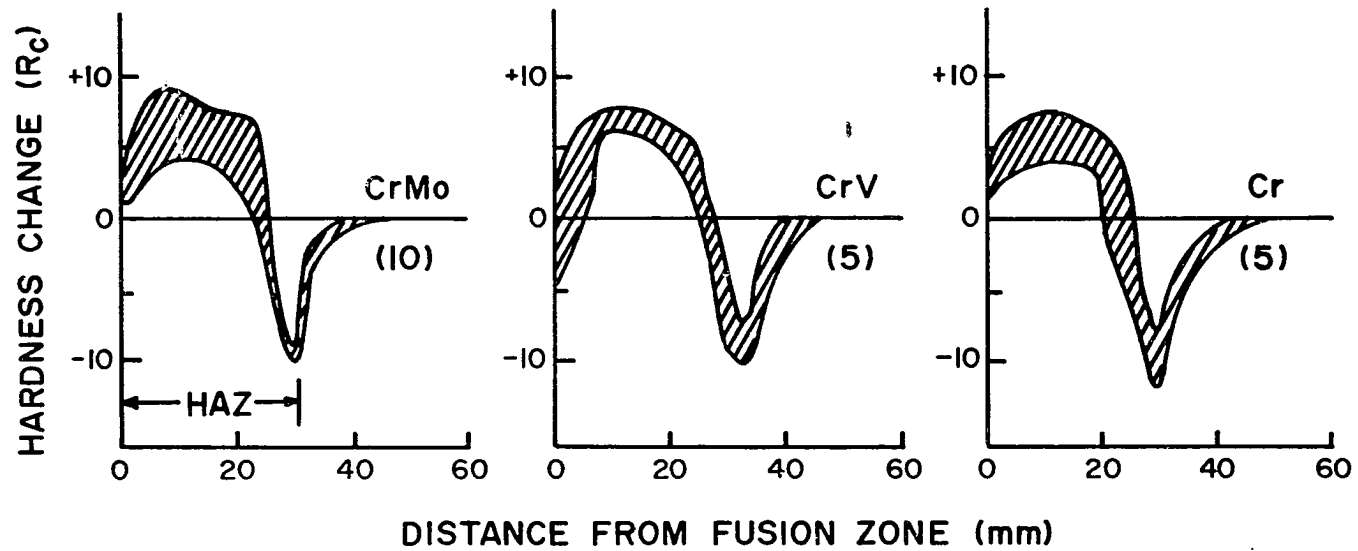


Figure 9: Hardness variations in the HAZs of alloy rails relative to the hardness of parent rail. Numbers in parentheses are the numbers of respective rails.

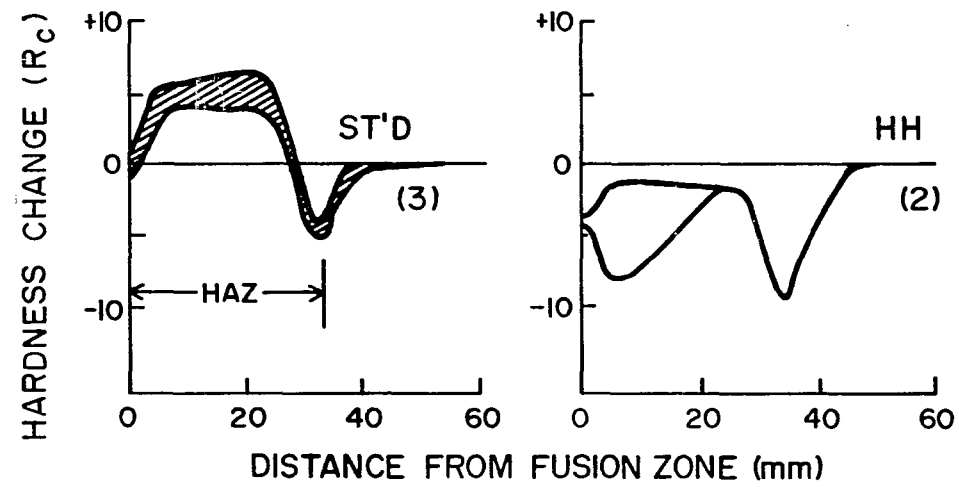


Figure 10: Hardness variations in the HAZs of standard and of head-hardened rail relative to the hardness of parent rail. Numbers in parentheses are the numbers of respective rails.

Table 5. Hardnesses of the Heat-Affected Zones in the Rail Welds

Rail Alloy	Weld	Preheat, min.	Use of Muffle	Hardness in HAZ, R _C		Hardness in Rail, R _C
				Maximum	Minimum	
CrMo	1	2	yes	40	25	34
	7	2	yes	32	20	30
	12*	2	yes	38	23	33
	2	2	no	40	22	33
	8	2	no	41	23	32
	13*	2	no	41	23	32
	3	3	yes	37	23	33
	14*	3	yes	38	23	32
						Avg: 32.4
CrV	9	2	yes	38	22	32
	4	2	yes	40	22	33
	5	2	no	40	25	32
	6	3	yes	39	24	33
	10	3	no	39	23	32
						Avg: 32.4

*Both sides of the weld were CrMo rail steel.

Table 5--Continued

Rail Alloy	Weld	Preheat, min.	Use of Muffle	Hardness in HAZ, R _C		Hardness in Rail, R _C
				Maximum	Minimum	
Cr	9	2	**	38	22	33
	1	2	yes	39	23	34
	2	2	no	40	24	32
	3	3	yes	38	22	32
	10	3	no	40	26	32
						Avg: 32.6
St'd	4	2	yes	32	20	25
	5	2	no	34	23	28
	6	3	yes	28	20	23
						Avg: 25.3
HH	7	2	yes	27	20	29
	8	2	no	29	20	30
						Avg: 29.5

**The mold was left intact for this weld.

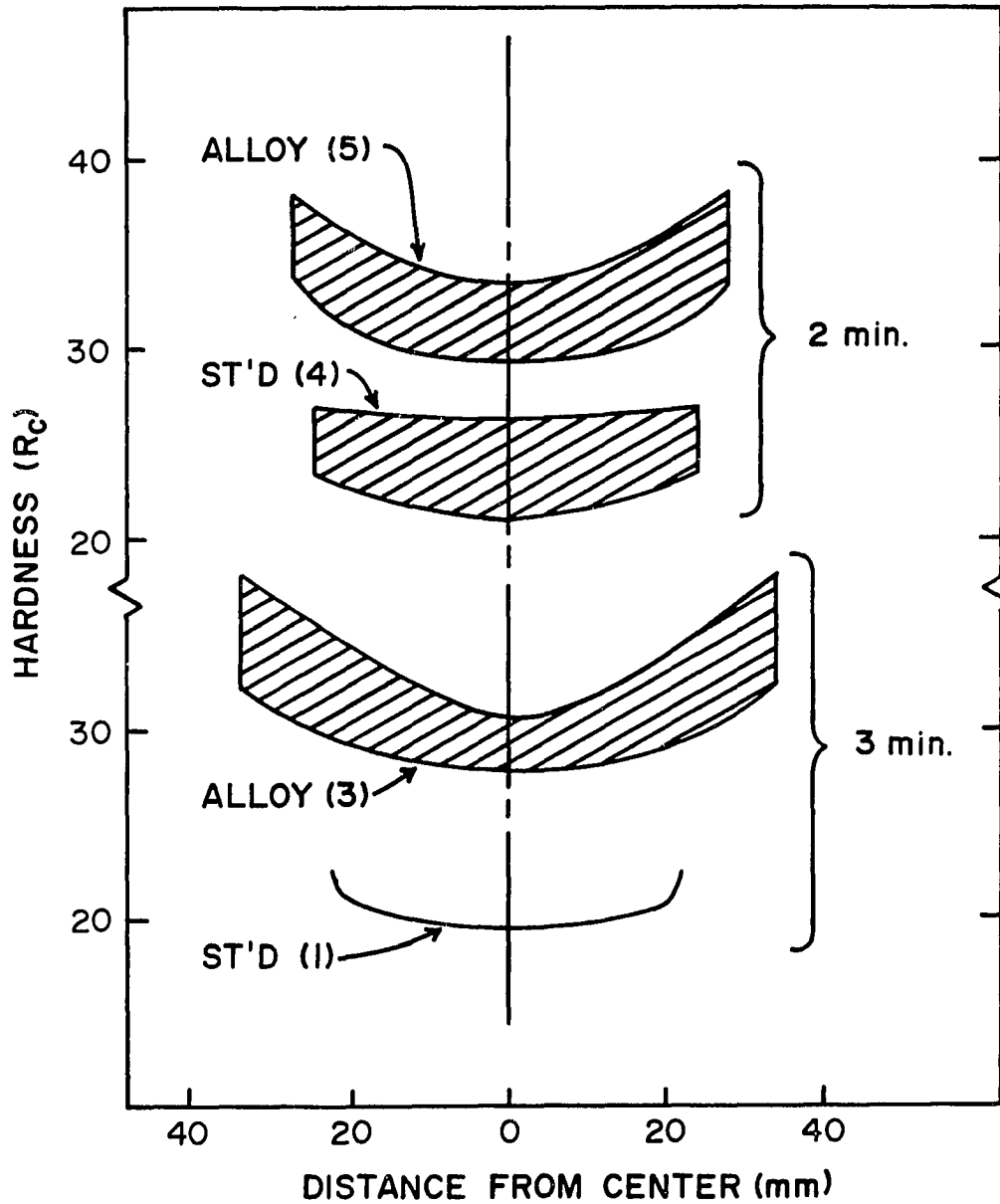


Figure 11: Hardness of the weld metal as a function of preheat time and distance from the weld centerline. Numbers in parentheses are the numbers of respective rails.

thermite steel has a hardness of 28-34 R_C at the center and 32-38 R_C near the fusion zone. This is significantly harder than the weld metal produced from the "standard" thermite steel which varies in hardness from 20 to 27 R_C .

Another effect is that of preheat time. As indicated above, preheat has no significant effect on the hardness within the HAZ. For the weld metal, however, a preheat of 3 minutes causes the weld metal to be about 2-5 R_C points softer at the center; this is evident in Figure 11. Finally, Figure 11 shows that the longer preheat increases the width of the weld metal by approximately 25 percent. This is true for the welds produced using "alloy" thermite steel, but there are not enough data to draw the same conclusion when a weld is produced using "standard" thermite steel.

4.1.2 Impact Properties. Impact properties were determined with Charpy V-notch specimens. Specimens were taken from the weld metal and from the transitional region between the HAZ and the unaffected rail on each side of the weld, as shown in Figure 5. The impact energies are tabulated in Table 6.

The impact energies do not show any trends associated with variations in preheating time or with retardation of cooling rates. In the weld metal, the impact energy is only 1.5 to 2.8 Joules (1.1 to 2.1 ft-lb_f) with only slightly better properties in the welds using the standard mix for the thermite steel.

The specimens in the heat-affected zones incorporated about 50 percent of the HAZ and 50 percent of the unaffected rail, as indicated in Figure 5. This location was selected because it includes the weakest

Table 6. Impact Energies of the Rail Welds at 20°C

Weld	A-Rail HAZ		C-Weld Metal		B-Rail HAZ	
	J	(ft-lb _f)	J	(ft-lb _f)	J	(ft-lb _f)
St'd Mix						
4	5.6	(4.1)	2.7	(2.0)	6.8	(5.0)
5	4.8	(3.5)	2.4	(1.8)	5.2	(3.8)
6	5.2	(3.8)	2.8	(2.1)	6.9	(5.1)
7	6.5	(4.8)	2.3	(1.7)	2.8	(2.1)
8	6.5	(4.8)	2.6	(1.9)	2.6	(1.9)
Alloy Mix						
1	6.1	(4.5)	2.0	(1.5)	5.7	(4.2)
2	5.2	(3.8)	1.8	(1.3)	6.8	(5.0)
3	4.3	(3.2)	1.5	(1.1)	4.3	(3.2)
9	5.2	(3.8)	1.6	(1.2)	9.6	(7.1)*
10	5.3	(3.9)	2.0	(1.5)	6.9	(5.1)
12	5.6	(4.1)	1.6	(1.2)	6.8	(5.0)
13	6.5	(4.8)	1.8	(1.3)	5.4	(4.0)
14	6.8	(5.0)	1.5	(1.1)	5.2	(3.8)

*Only 10 percent of HAZ in fracture.

metal at the edge of the HAZ. With the exception of the B-specimen in weld 9, the fractures did, in fact, reveal approximately 50 percent of the cross-section to be in the HAZ, and this was further verified by lightly etching the fractured impact specimens to reveal the HAZ. Given the scatter typically associated with impact energy, no trends can be associated with rail chemistry, preheating time or retardation of cooling. An exception appears to be the low energies of the HAZ of the head-hardened rail (welds 7 and 8). These energies, 2.8 and 2.6 Joules, are lower than the remaining energies which range from 4.3 to 6.9 Joules. Weld 9, with one side of the HAZ at 9.6 Joules, is another exception, but this is due to the fact that approximately 90 percent of the fracture surface was within the unaffected rail. The low energies in welds 7 and 8 are probably the result of a mixed structure which resulted from the head-hardened rail steel; these microstructures are discussed later. Notice, also, that the hardnesses in the HAZs of the head-hardened rails are less than 30 R_c and less than the unaffected rail, Figure 10.

4.1.3 Tensile Properties. Tensile properties were determined with reduced size tensile bars (6.4 mm dia. with 25.4 mm gage length). Specimens were taken from across the weld metal and across the HAZ on each side of the weld, as shown in Figure 5. The tensile properties are given in Table 7.

The tensile properties of the weld metal, C-specimens in Table 7, are shown in Figure 12, as a function of Brinell hardness number at the center of the weld (converted from measured R_c hardness). Appendix A contains the linear regression analyses of these data. As expected,

Table 7. Tensile Properties of the Rail Welds

Weld	Specimen Location	BHN	Yield Strength		Ultimate Strength		True Fracture Strength		Percent Elongation Δ	Percent Reduction of Area
			0.2% Offset MPa	(ksi)	MPa	(ksi)	MPa	(ksi)		
St'd Mix										
4	A-HAZ	236	476	(69)	855	(124)	1103	(160)	6.8	25.3
	C-Weld		469	(68)	772	(112)	814	(118)	2.7	4.7
	B-HAZ		558	(81)	924	(134)	1475	(214)	11.9	58.3
5	A	255	552	(80)	883	(128)	1048	(152)	4.9	16.8
	C		538	(78)	800	(116)	821	(119)	1.5	2.4
	B		534	(78)	924	(134)	945	(137)*	9.0	20.5
6	A	227	462	(67)	855	(124)	1041	(151)	5.7	18.9
	C		462	(67)	786	(114)	834	(121)	3.8	5.5
	B		579	(84)+	958	(139)	938	(136)*	10.6	25.9
7	A	233	545	(79)+	952	(138)	1565	(227)	10.0	54.7
	C		586	(85)	800	(116)	814	(118)	1.3	1.6
	B		469	(68)+	862	(125)	1344	(195)	9.9	46.0

* Failed outside necked region, within 2.5 mm (0.1 in.).

+ Yield point displayed.

Δ 25.4 mm (1.0 in.) gage length

Table 7--Continued

Weld	Specimen Location	BHN	Yield Strength 0.2% Offset		Ultimate Strength		True Fracture Strength		Percent Elongation Δ	Percent Reduction of Area
			MPa	(ksi)	MPa	(ksi)	MPa	(ksi)		
8	A	244	588	(81)+	952	(138)	1372	(199)	10.4	49.1
	C		572	(83)	841	(122)	869	(126)	2.6	3.2
	B		476	(69)+	869	(126)	1317	(191)	10.1	44.1
Alloy Mix 1	A	310	558	(81)+	931	(135)	1048	(152)	7.6	24.1
	C		683	(99)	1000	(145)	1027	(149)	3.2	2.4
	B		510	(74)+	931	(135)	1110	(161)	7.2	33.0
2	A	290	586	(85)+	931	(135)	1544	(224)	10.3	43.2
	C		669	(97)	938	(136)	965	(140)	1.0	2.4
	B		552	(80)	952	(138)	1041	(151)	10.0	45.2
3	A	268	593	(86)+	945	(137)	1262	(183)	9.5	50.0
	C		558	(81)	889	(129)	931	(135)	1.6	2.4
	B		531	(77)+	938	(136)	1489	(216)	10.8	54.8
9	A	286	558	(81)+	889	(129)	1517	(220)	10.9	57.3
	C		620	(90)	979	(142)	1020	(148)	2.1	3.9
	B		545	(79)+	883	(128)	1496	(217)	13.0	61.2

+Yield point displayed.
 Δ 25.4 mm (1.0 in.) gage length.

Table 7--Continued

Weld	Specimen Location	BHN	Yield Strength		Ultimate Strength		True Fracture Strength		Percent Elongation Δ	Percent Reduction of Area
			0.2% Offset MPa	(ksi)	MPa	(ksi)	MPa	(ksi)		
10	A	286	531	(77)+	945	(137)	1096	(159)	8.4	25.8
	C		634	(92)	979	(142)	1007	(146)	1.8	3.2
	B		565	(82)+	958	(139)	1069	(155)	7.4	23.9
12 (two sets)	A	296	717	(104)	931	(135)	1627	(236)	9.9	59.4
	C		572	(83)	938	(136)	972	(141)	1.2	3.2
	B		607	(88)	924	(134)	1565	(227)	11.0	57.6
	A	620	(90)	938	(136)	1034	(150)*	8.3	29.4	
	C	607	(88)	931	(135)	958	(139)	1.0	2.4	
	B	510	(74)	910	(132)	1551	(225)	10.1	54.5	
13	A	314	552	(80)+	952	(138)	1613	(234)	10.3	56.4
	C		696	(101)	979	(142)	1007	(146)	1.3	2.4
	B		558	(81)+	958	(139)	1462	(212)	9.6	51.4
14	A	282	820	(119)	1000	(145)	1455	(211)	11.6	47.2
	C		614	(89)	924	(134)	958	(139)	1.1	3.2
	B		531	(77)+	945	(137)	1503	(218)	10.0	54.3

*Failed outside necked region, within 2.5 mm (0.1 in.).

+Yield point displayed.

Δ 25.4 mm (1.0 in.) gage length.

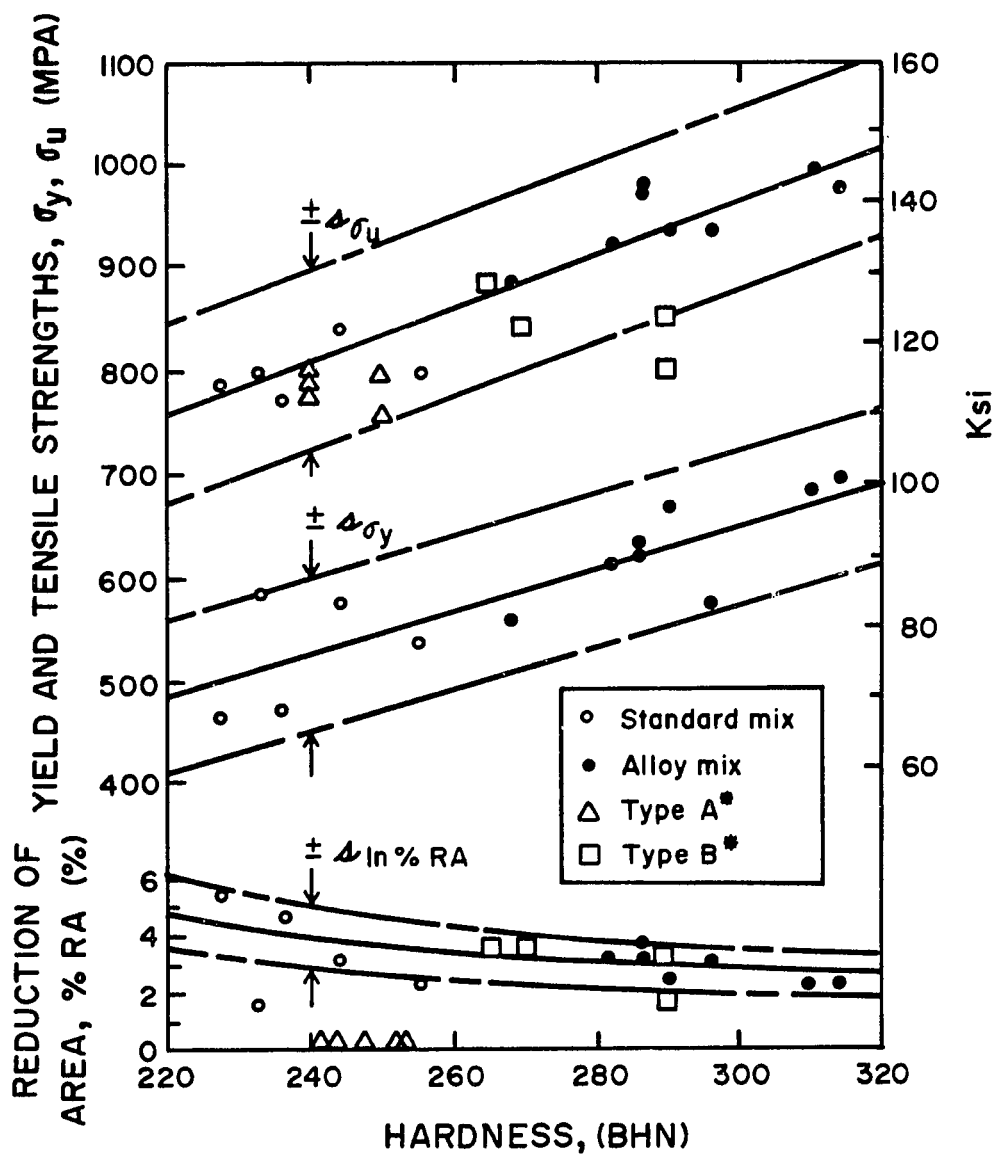


Figure 12: Tensile properties of weld metal as a function of hardness.
 *From Ref. (24); not included in linear regression analyses.

the data show scatter, but tensile strength and yield strength increase with hardness. Ductility (percent reduction of area) decreases from 4-6 percent at a hardness of 224 BHN to 2-4 percent for hardnesses greater than 250 BHN. Weld 7 appears to be an anomaly among the data shown in Figure 12 in that at its hardness, the ductility is significantly lower and its yield strength is higher than the remaining data apparently indicate. This is probably due to a very nonuniform hardness at the center of the weld metal in this weld, Figure 8.

Figure 12 shows that the weld metal prepared from "alloy mix" is consistently harder (268-314 BHN) than weld metal prepared from "standard mix" (227-255 BHN). Accordingly, the "alloy mix" is usually stronger (approximately 103-138 MPa) with slightly less reduction of area than exhibited by the "standard mix". Finally on Figure 12, data (tensile strength and reduction of area) from another study (24) are also shown. For the most part, tensile strengths are comparable. However, that there is no ductility for the specimens labeled Type A indicates that these specimens were embrittled or contained an excessively large number of nonmetallic inclusions.

It is difficult to draw conclusions for the tensile properties of the specimens removed from the heat affected zones, as given in Table 7. Apparently the steep gradient in hardness, where hardness is a minimum at the outer edge of the HAZ, causes the yield strength to be rather unpredictable. For example, the yield strengths among the CrMo rails vary from a low of 476 MPa (69 ksi) to a high of 820 MPa (119 ksi) yet there are no significant differences between their respective hardness profiles. The Cr rails show similar results, yet the CrV

rails, the standard rails and the head-hardened rails do not exhibit similar deviations in yield strength; however, the number of tests for these rails is significantly less than the number of tests on CrMo rails.

The tensile strength is more predictable than is the yield strength of the specimens from the heat-affected zones. All of the alloy rails (CrMo, Cr and CrV) have tensile strengths which are in the range 869-1000 MPa (126-145 ksi). In all rails, the tensile specimens exhibit significant ductility (17 to 61 percent) which far exceeds the weld metal (2 to 6 percent).

4.1.4 Fractography of Impact and Tensile Specimens. The fracture surfaces of the impact and tensile specimens were examined by a SEM/EDS* system. In most instances, the SEM mode was used to study the fractures, but when atypical features on the fractures were encountered, the EDS was employed to gather qualitative chemical analyses. The results of the fractographic analyses are presented in the order of observations of the fractures of the Charpy V-notch (CVN) specimens and then descriptions of the fractures of the tensile specimens. Each group is discussed in terms of the specimens removed from the HAZ and from the weld metal, respectively.

4.1.4.1 Charpy V-Notch Specimens in the HAZ. Two-thirds of the CVN specimens straddled the regions of minimum hardness in the HAZ with the notch oriented such that the crack propagated across the thickness of the rail in a direction perpendicular to the rolling direction.

*Scanning electron microscope with an energy dispersive spectroscopy analyzer.

Figure 5 shows the specimens; according to the classification in Hertzberg (85), the specimen orientations were T-S (width long transverse-thickness short transverse).

Since part of the cross-section of each specimen was in the rail beyond the HAZ and the remainder was in the HAZ, the fractures had a duplex appearance, which was apparent when examined visually and with the SEM. Figure 13 shows a fracture at a low magnification, which is typical of the fractures observed for all welds. The material beyond the HAZ (the original rail in Figure 13) has a faceted fracture which is coarser in appearance than the more fibrous fracture within the HAZ. At a higher magnification, the fracture in the "original rail", Figure 14a, is mostly cleavage with some intergranular separation on surfaces which are almost normal to the major crack. In the lower-right corner, an elongated MnS inclusion, which has partially separated from the matrix, can be seen. Figure 14a is typical of fractures of rail steel; e.g., see Park and Bernstein (86). Figure 14b shows the fracture appearance in the region of minimum hardness. The major portion of the fracture has details finer than those of Figure 14a with an appearance described in quasi-cleavage (87), with some regions of intergranular separations similar to those in Figure 14a.

According to Table 6, specimen 1-B shows an energy absorbed of 5.7 J. Feddersen and Broeck (88) report values of about 2.7-5.4 J for rail steels at 20°C. Thus, the energy absorbed by the fracture shown in Figures 13 and 14 is comparable to unwelded rail; in fact, all of the data for the HAZs in Table 6 are comparable to the impact energies for unwelded rail.

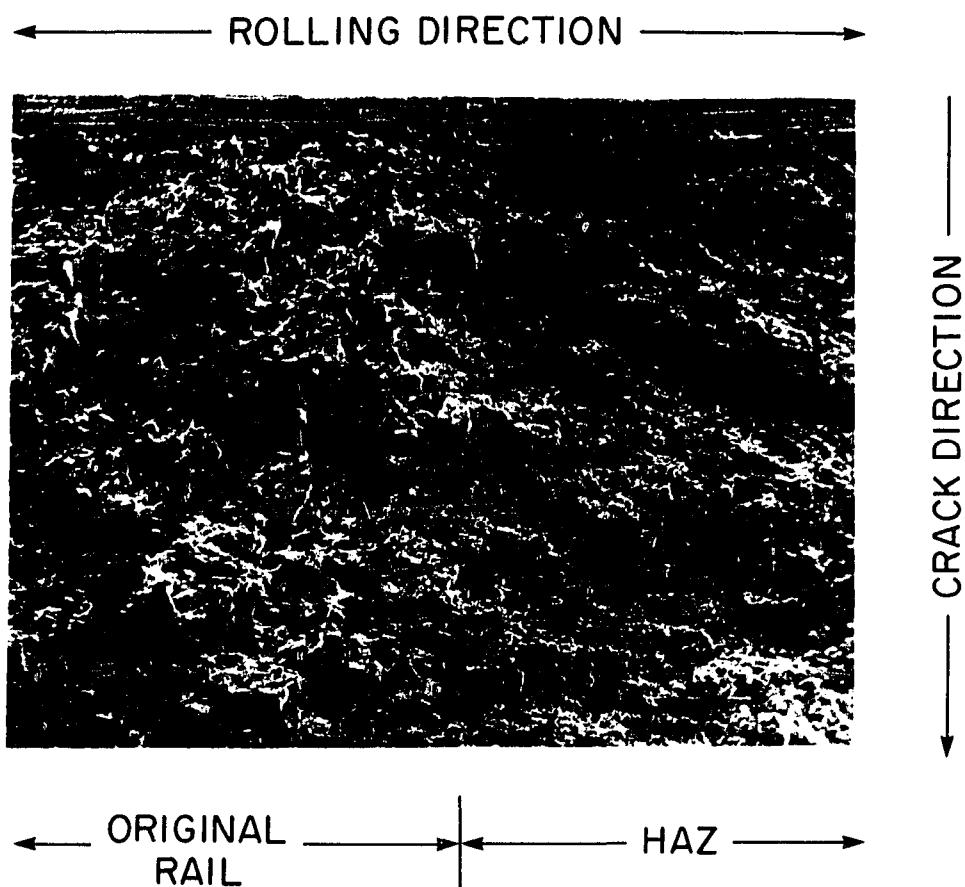


Figure 13: Fracture of impact specimen through the region of minimum hardness in heat-affected zone. Fractograph is from the CrMo side of weld 1. 17X.

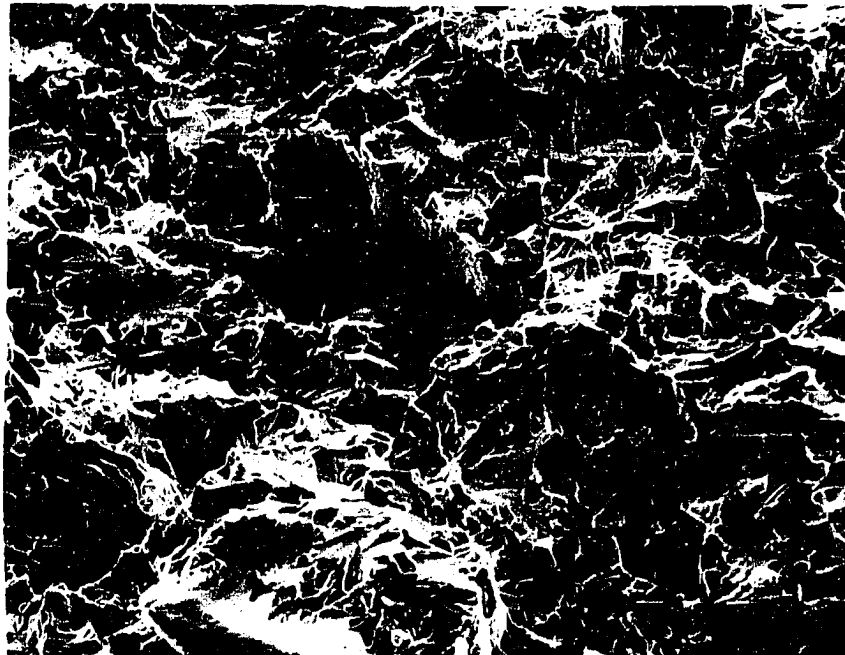
The lowest impact energy of a HAZ shown in Table 6 is 2.6 J for specimen 8-B, which was removed from a head-hardened rail. The fracture appearance on the rail side of the region of minimum hardness, Figure 15a, is similar to Figure 14a, except that the transgranular facets are larger, which is consistent with less energy absorbed in an impact test. A MnS inclusion is also present in this fractograph, Figure 15a. In the HAZ portion, Figure 15b, the fracture is similar to Figure 14b; of course, in both instances, partial spheroidization has occurred and the minimum hardnesses are approximately equal.

As indicated above, MnS inclusions, elongated in the direction of rolling, were often seen in the fracture surfaces of the rail material; e.g., see Figures 14a and 15a. In all but four fractures of the twenty-six impact specimens for the region of minimum hardness in Table 6, delamination of the rail was evident. An example is shown in Figure 16, which is a fractograph from the CrV side of weld 4. The delamination occurs on the side opposite the notch. In this case, the delamination was detected in about 10-15 percent of the HAZ side of the region of minimum hardness, where the pearlite has partially spheroidized. Among the welds in which the delamination was seen, it occurs always on the side opposite the notch and predominately in the HAZ side, regardless of the type of rail.

4.1.4.2 Charpy V-Notch Specimens in the Weld Metal. For the most part, the appearance of these fractures was similar to the fractures of unwelded rail with transgranular cleavage and some evidence of intergranular separations, Figure 17. The fracture appearance was similar for all welds regardless of weld metal chemistry, preheat time, or

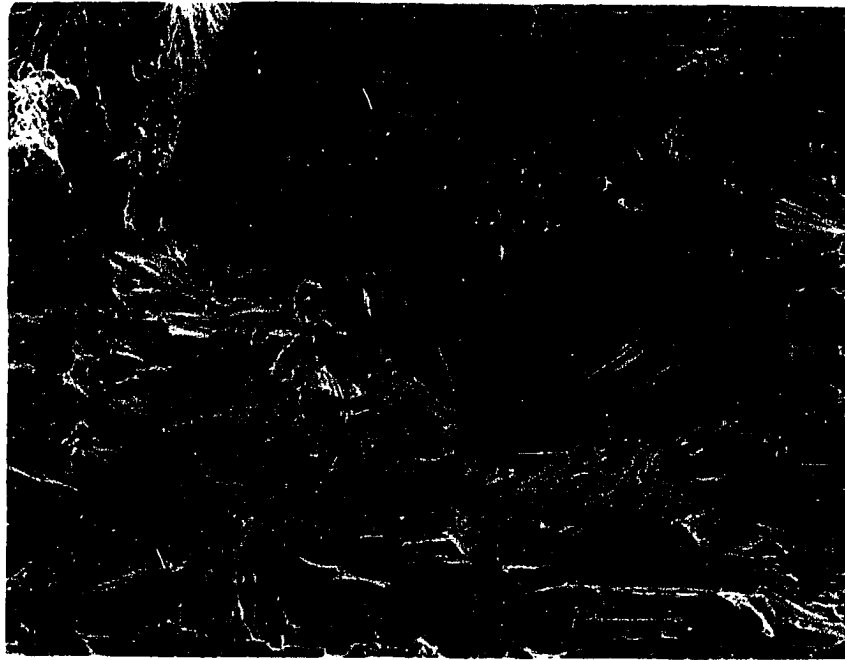


(a)

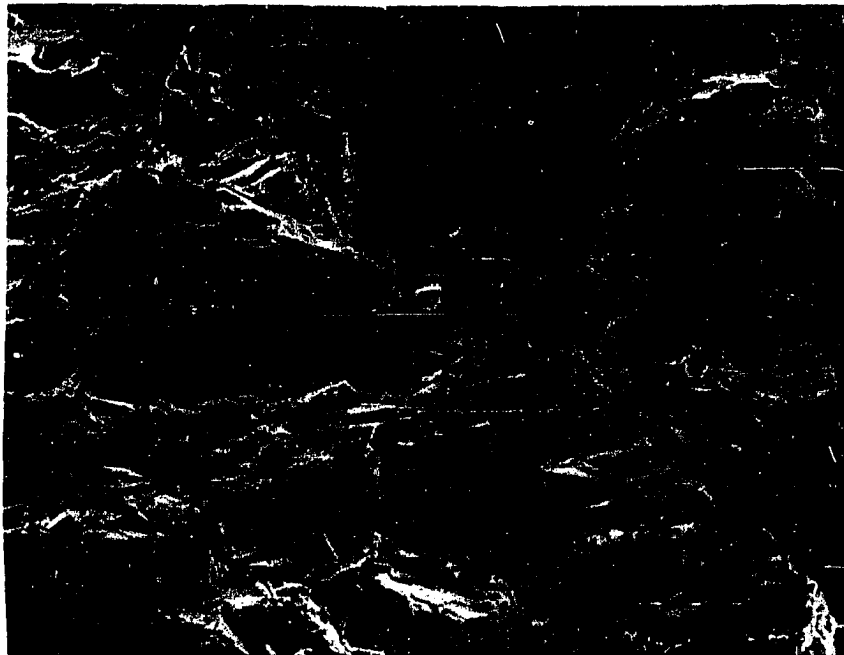


(b)

Figure 14: Fracture surface of Figure 13; (a) original rail side; (b) HAZ side. 280X.



(a)

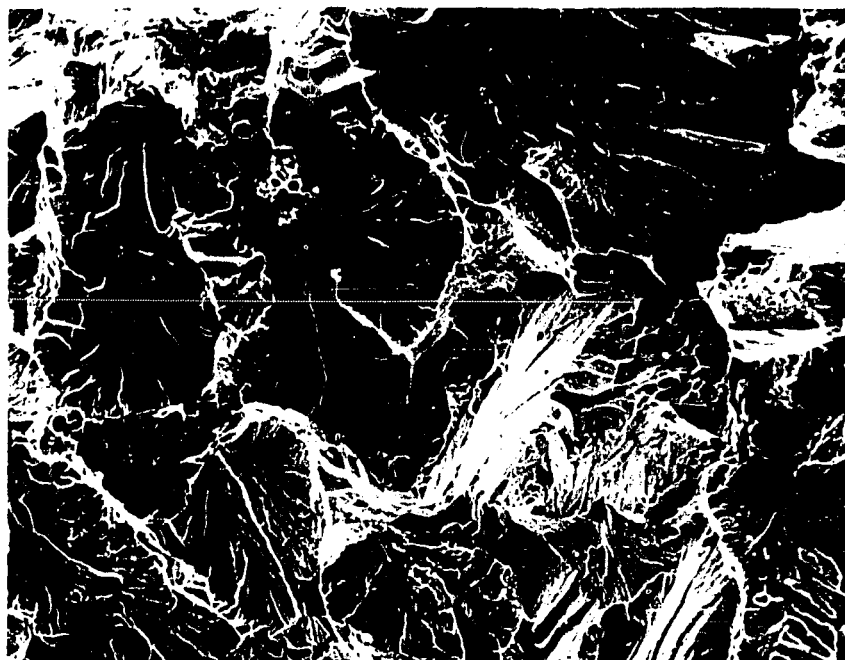


(b)

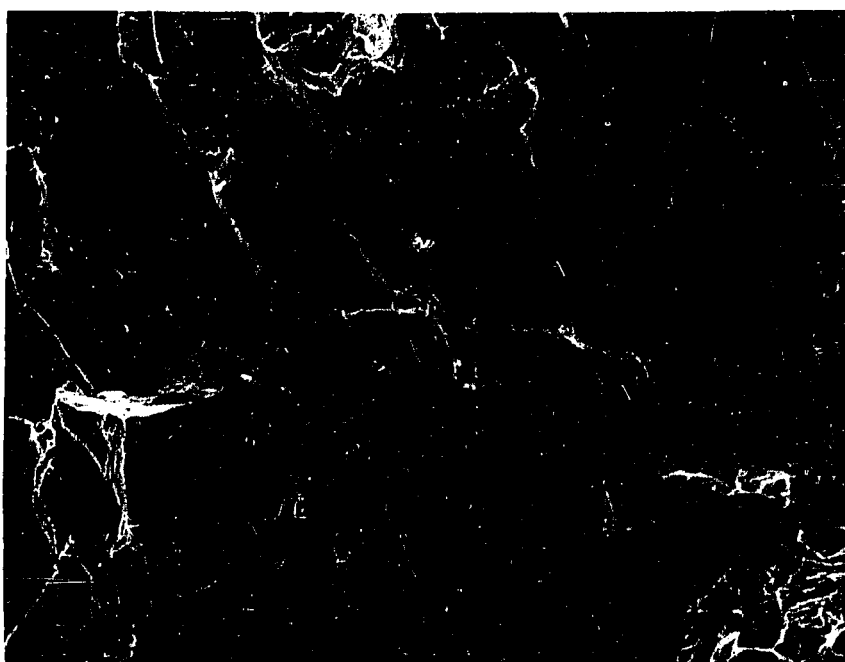
Figure 15: Fracture of impact specimen through the region of minimum hardness in the HAZ of the HH rail of weld 8. (a) original rail side; (b) HAZ side. 280X.



Figure 16: Delamination of the HAZ side (region of minimum hardness) of the impact specimen from the CrV rail of weld 4. Bottom of the photomicrograph is the side opposite the V-notch. 52X.



(a)



(b)

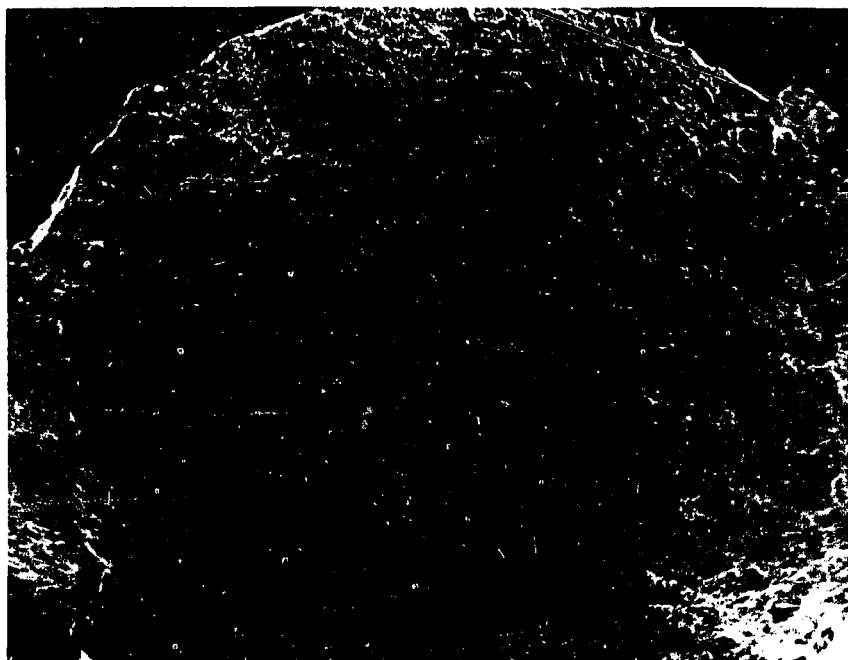
Figure 17: Fracture of impact specimens from the weld metal. (a) weld 1, alloy weld metal; (b) weld 8, st'd. weld metal. 280X.

cooling rate. Although not evident in the fractographs of Figure 17, small amounts of microporosity were observed when the specimens were studied with the SEM. Small inclusions were observed on the facets which can be seen in Figure 17. The inclusions in all impact specimens were qualitatively analyzed with the EDS system, which showed predominantly Al with lesser amounts of Mn, S and Si. Presumably, the inclusions are rich in Al_2O_3 and contain SiO_2 and MnS.

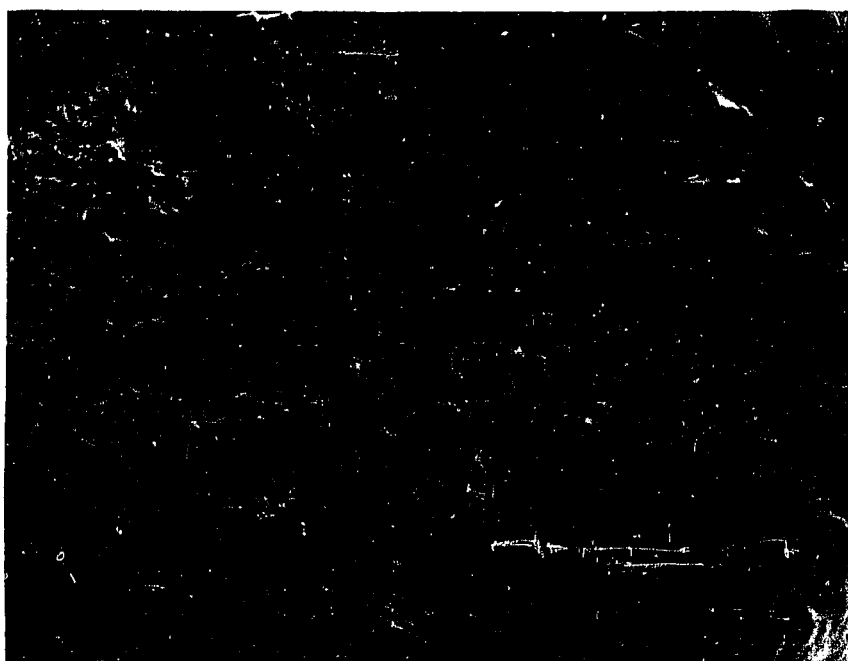
4.1.4.3 Tensile Specimens in the HAZ. The tensile specimens were oriented longitudinally and across the region of minimum hardness in the head portion of the rails, as shown in Figure 5. Collectively as a group, these fractures were more complex than those of the CVN specimens. Four types of fractures were noted: (1) cleavage with a small shear lip, Figure 18a; (2) cleavage with a fibrous central-region and no shear lip, Figure 18b; (3) "cup and cone" fractures, Figures 19a and 19b; and (4) "cup and cone" with radial features, Figures 20a and 20b.

Table 8 summarizes the specimens according to the above classification. It shows that the failures of types 1 and 2 have ductilities in the range of 16.8-29.4 percent reduction of area and that types 3 and 4 have ductilities in the range of 43.2-61.2 percent reduction of area with one exception at 33 percent (tensile specimen 1-B).

Table 9 summarizes the distribution of rail types according to the observed fractures. The number of specimens is small (the greatest number is 13 for CrMo), but it appears that the failures of the CrMo rails are among the fractures of high ductility, with the exception of one specimen (12-A). That particular specimen necked, but the fracture

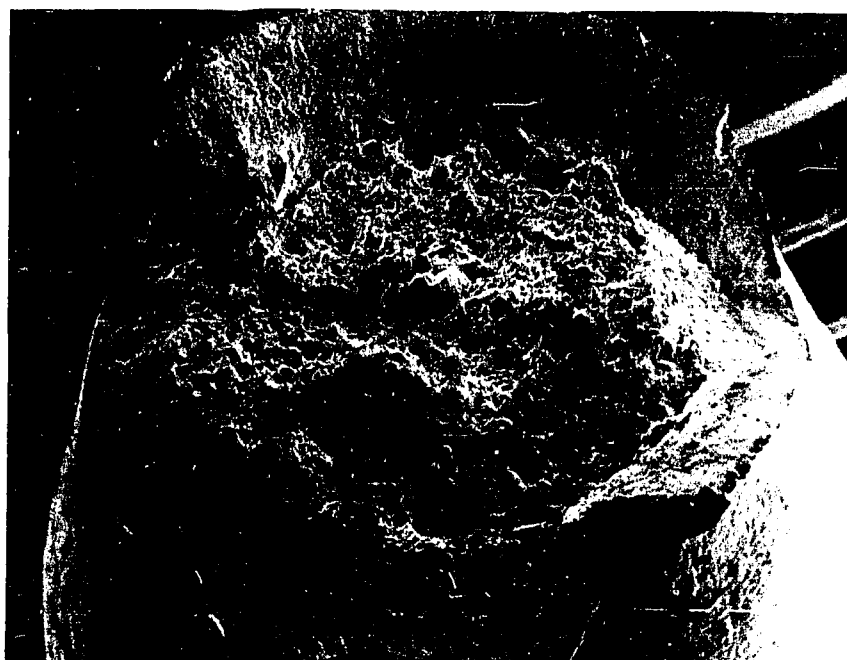


(a)

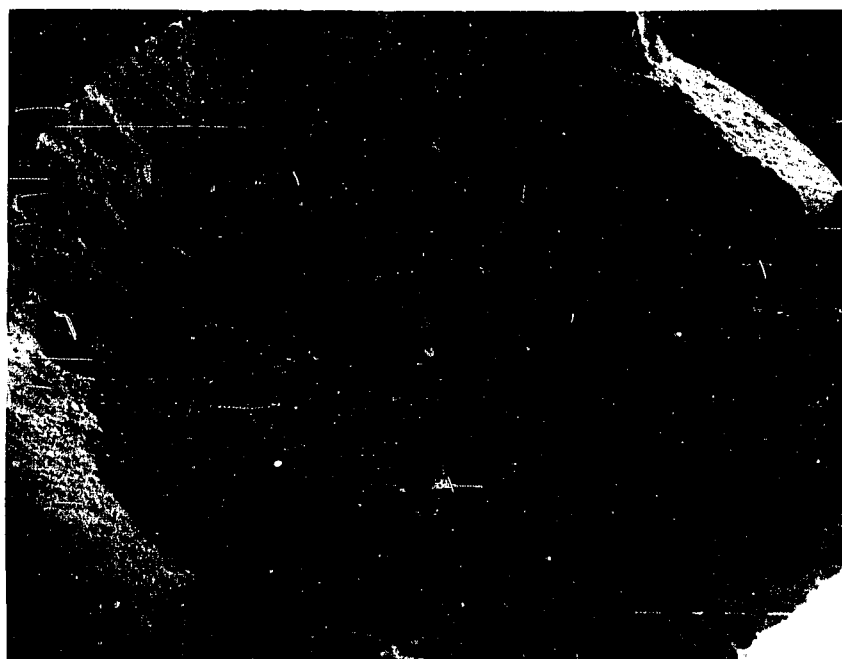


(b)

Figure 18: Low ductility tensile fractures in the region of minimum hardness. (a) weld 1-Cr rail; (b) weld 4-st'd. rail. 24X.



(a)



(b)

Figure 19: "Cup and Cone" tensile fractures in the region of minimum hardness. (a) weld 1-CrMo rail, 23X; (b) weld 8-HH rail, 28X.



(a)



(b)

Figure 20: "Cup and Cone" tensile fractures with radial features in the region of minimum hardness. (a) weld 4-CrV rail, 25X; (b) weld 8-CrMo rail 29X.

Table 8. Fracture Characteristics of Tensile Specimens of the Heat-Affected Zones in the Rail Welds

Fracture	Specimen	Rail Type	Range of Reduction of Area (%)
1. Cleavage with shear lip	1-A, 10-A, 5-B*, 6-B*, 10-B* 12-A* (lowest RA)	Cr CrV CrMo	20.5 - 29.4
2. No Shear lip, cleavage with fibrous central region	4-B, 5-A, 6-A	Standard	16.8 - 25.3
3. "Cup and Cone", fibrous central region with shear lip	1-B 7-B, 8-B	CrMo HH	33.0 - 46.0
4. "Cup and Cone" with radial features joining fibrous central region to shear lip	2-A, 3-A, 9-A 4-B, 9-B 2-B, 3-B, 7-A 8-A, 12-A (highest RA), 12-B (both) 13-A,B, 14-A,B	Cr CrV CrMo	43.2 - 61.2

*Failed outside necked region, within 2.5 mm.

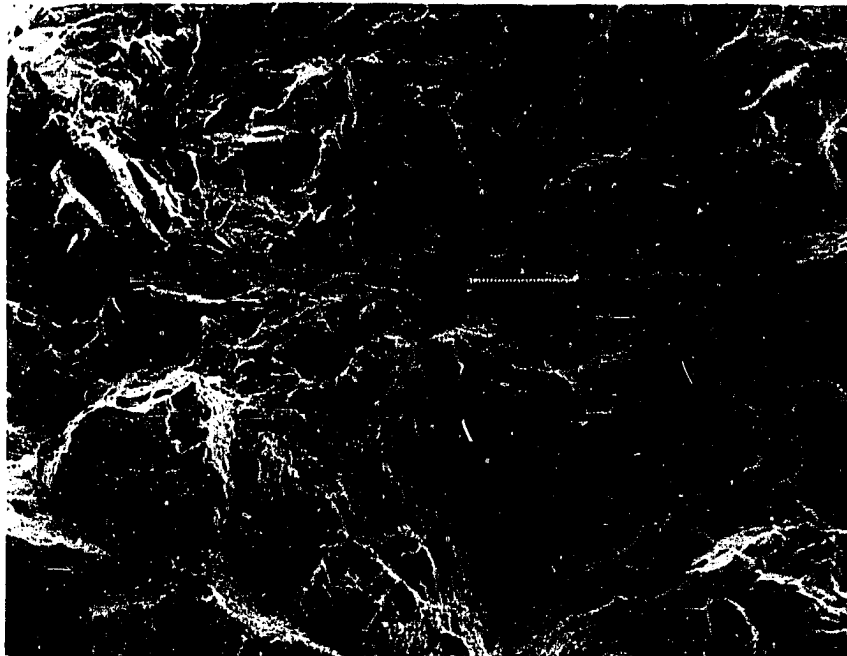
Table 9. Fracture Categories of Tensile Specimens in the Region of Minimum Hardness

Rail	Number of Specimens	Low Ductility Fracture		High Ductility Fracture	
		Type 1	Type 2	Type 3	Type 4
Standard	3		3		
Head-hardened	2			2	
Cr	5	2			4
CrMo	13	1		1	11
CrV	5	3			2

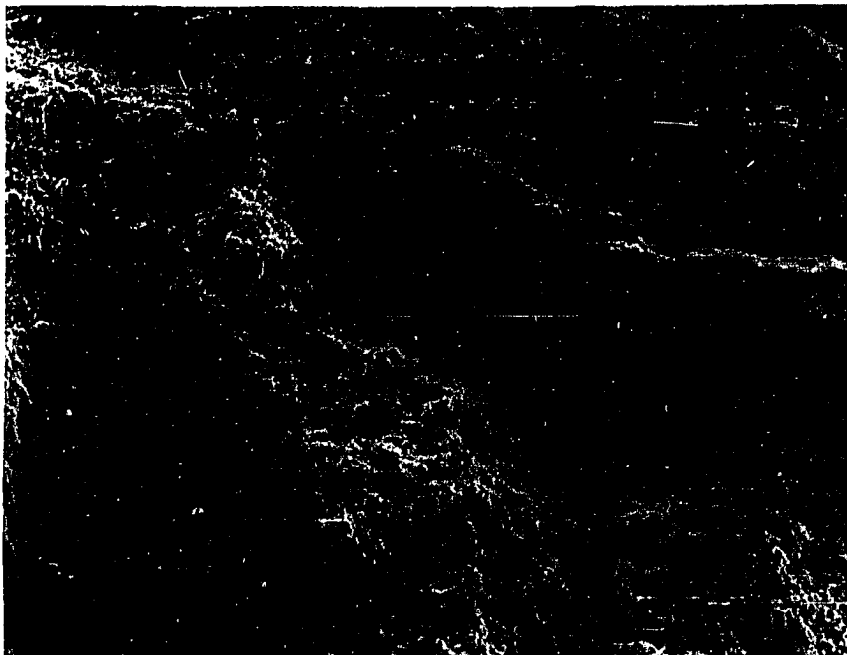
was displaced slightly from the location of the minimum area. The three specimens from the standard rails failed with low ductility (type 2), the head-hardened with high ductility, and the Cr and CrV rails had failures of high and low ductilities.

Figures 21a and 21b show the fractures of a low-ductility and of a high-ductility specimen, respectively. Figure 21a is a type 2 fracture at the transition between the central-fibrous region (the lower portion of the fractograph) and the region of transgranular cleavage (the upper portion of the fractograph). Figure 21b is an example which shows the details of a radial feature. Along the "cliff" which goes across most of the fractograph, one can see evidence of the inclusions elongated in the rolling direction. There are numerous secondary cracks and also many holes resulting from the separation of the matrix from the inclusions. Many of these holes were qualitatively analyzed with the EDS, and Mn and S were always detected in significant amounts. Since the inclusions in the rails are elongated in the rolling direction, rather high ductility is observed because the tensile specimens are oriented longitudinally. However, if specimens oriented transverse to the rolling had been selected, then it is likely that the ductility would be significantly less.

4.1.4.4 Tensile Specimens in the Weld Metal. The mode of fracture of the tensile specimens removed from the weld metal for all of the welds was essentially cleavage, which corresponds to the low ductility reported in Table 7. Figures 22a and 22b show the fractures of alloy weld metal and standard weld metal, respectively. In Figure 22b, there is a large region showing the separation of an as-cast



(a)



(b)

Figure 21: Tensile fractures in the region of minimum hardness. (a) weld 4-st'd. rail, 240X; (b) weld 4-CrV rail, 250X.



(a)



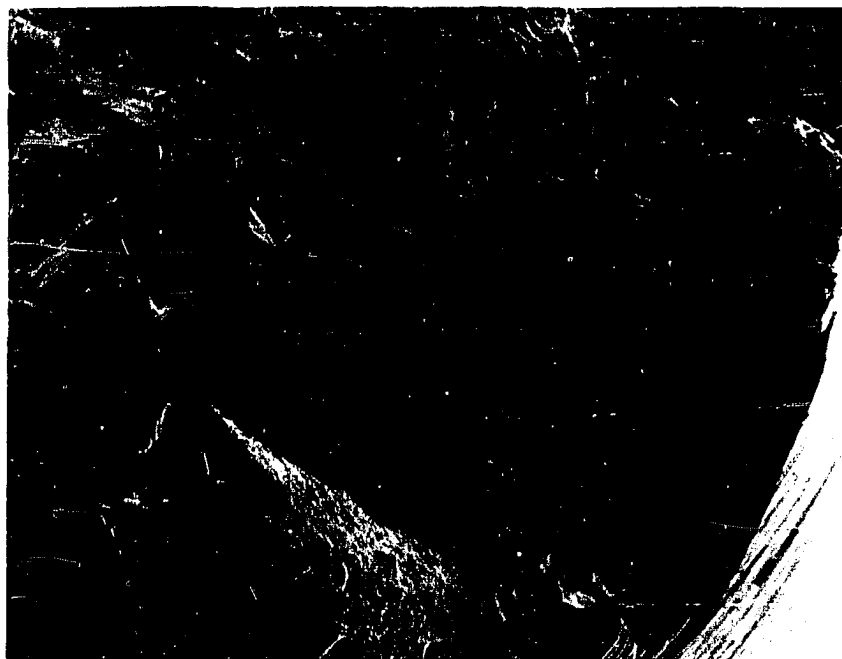
(b)

Figure 22: Tensile fractures of the weld metal. (a) weld 3-alloy weld metal; (b) weld 4-st'd. weld metal. 25X.

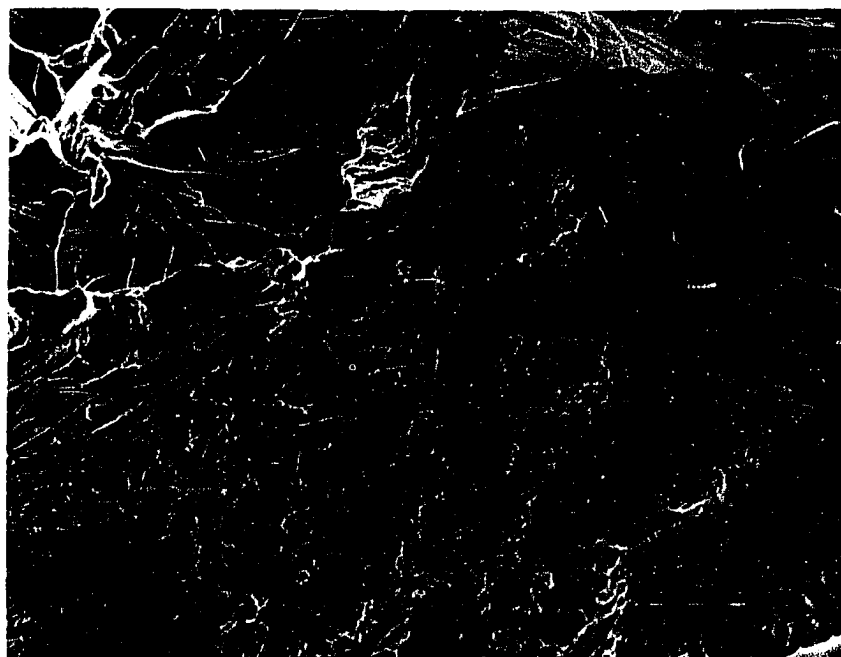
columnar grain from its neighbor with the dendritic structure readily apparent. Tensile bars were removed from five welds prepared from standard weld metal, and their fractures all displayed one or two of these features which occupied about 10-25 percent of the fracture area. None of the tensile specimens from alloy welds showed this feature. At a greater magnification, it is clear that the as-cast grain boundaries have separated; this can be seen in Figure 23. In Figure 23b, much of the surface of the grain boundary is smooth with rough areas corresponding to the dendrite arms shown in Figure 23a. Before fracture, neighboring columnar grains were bridged at the rough areas; fracture merely tore the "bridges" and produced the roughness.

The direction of the as-cast columnar grains exposed in Figures 22b and 23 corresponds closely to the dendrite direction, shown in Figure 24. The tensile specimens were removed from the head portion where the dendrites are oriented at approximately 45° to the horizontal, and this corresponds to the large regions of easy separation in the fractures of standard weld metal. The absence of similar features in alloy weld metal cannot be explained.

Further evidence that the regions of easy separation are as-cast columnar grain boundaries is given in Table 10. The regions were semi-quantitatively analyzed and found to contain high concentrations of many elements, particularly Ni, Cu and Zn. These analyses are similar to the analyses in Table 11, which are from surfaces of dendrite arms found in areas of microporosity, Figure 25. Since microporosity occurs between dendrite arms, then it follows that the surfaces of the dendrite arms in Figure 25 would exhibit segregation; as-cast grain boundaries (between



(a)



(b)

Figure 23: Fracture of the tensile specimen from the standard weld metal of weld 6. (a) 50X; (b) 270X.

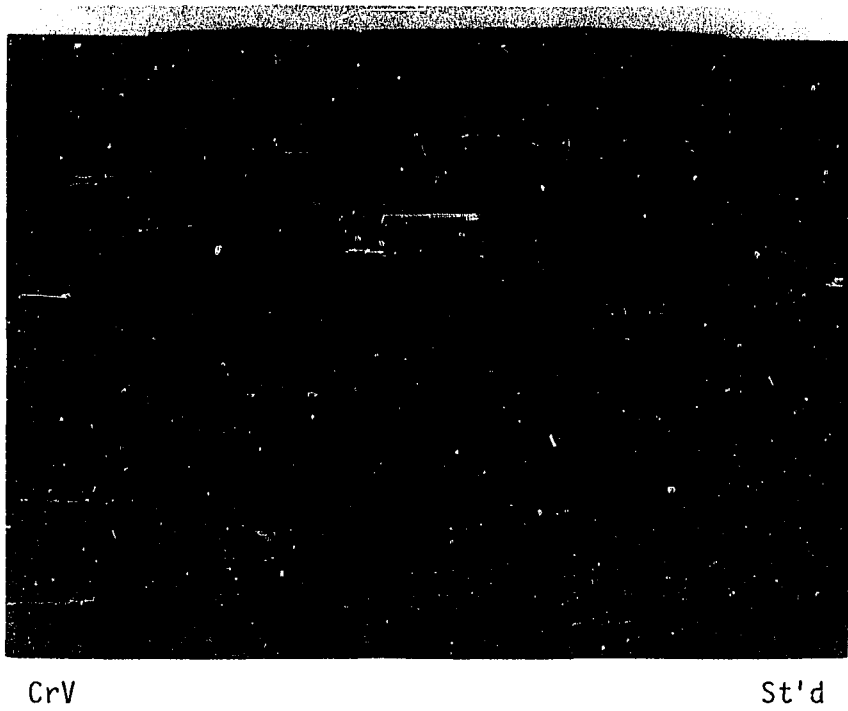


Figure 24: Macrostructure of the head area of weld 6. 1X.

Table 10. EDS Analyses of the Surfaces of the As-Cast Columnar Grains in Standard Weld Metal

Element	Count Ratios			
	Weld 4	Weld 8	Weld 6	Weld 7
Fe	1	1	1	1
Ni	0.49	1.33	0.36 & 0.43	0.35
Cu	0.21	0.64	0.15 & 0.18	0.14
Zn	0.13	0.37	0.09 & 0.11	0.09
Al	0.03	0.16	0.03 & 0.03	0.03
Mn	0.06	0.09	0.05 & 0.05	0.05
Si	0.03	0.07	0.04 & 0.04	0.03
P	0.05	0.14	0.05 & 0.06	0.05

Table 11. EDS Analyses of the Surfaces of Dendrites in Alloy Weld Metal

Element	Count Ratios	
	Weld 10	Weld 3
Fe	1	1
Ni	0.42	0.36
Cu	0.31	0.16
Zn	0.18	0.10
Al	0.03	0.03
Mn	0.06	0.05
Si	0.04	0.04
P	0.06	0.05
Cr	0.05	0.04

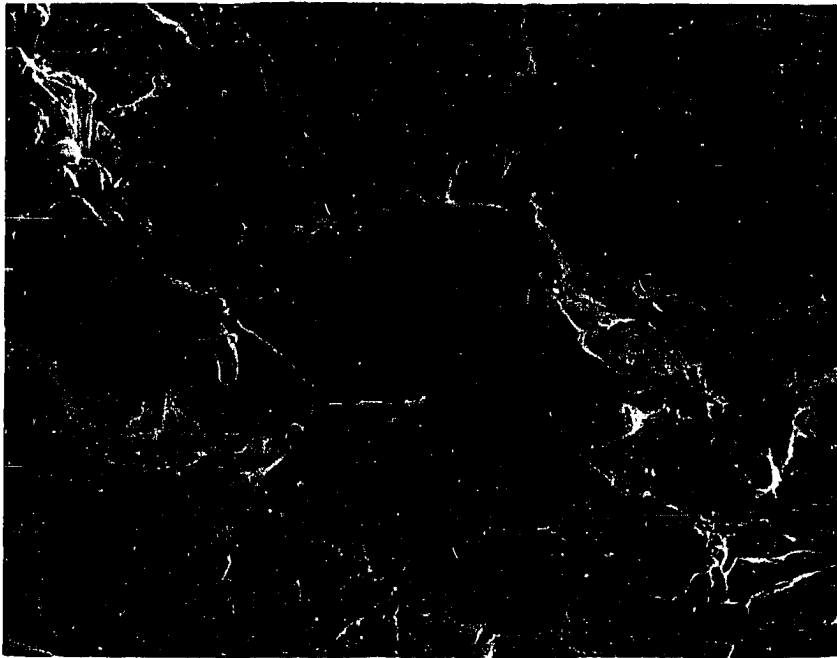


Figure 25: Tensile fracture of the alloy weld metal of weld 10 showing microporosity. 290X.

neighboring arrays of similarly oriented dendrites) also would be expected to exhibit segregation.

4.2 Structural Analyses of Rail Welds

4.2.1 Macrostructures. The weld macrostructures appeared independent of all weld parameters except preheat time. Preheat time affected the extent of melt back or the width of the weld deposit. At the location of the hardness profile, the deposit width was 45-58 mm for the standard preheat and 64-74 mm for the long preheat with the exception of weld 6. Weld 6 was subjected to a long preheat but displayed a deposit width of only 46 mm. A possible explanation for this discrepancy is a suppressed reaction temperature and thus reduced superheat. Also, weld 6 was the first weld of the day (ambient temperature was only -1°C) so that inadequate preheating of the reaction crucible could have contributed to a loss of superheat.

Overall, with the exception of weld 6, the weld deposits for the long preheats were 20-30 percent wider than for the standard preheat. At all locations, growth of primary dendrite arms was essentially perpendicular to the fusion zone. These effects are shown in the representative macroteches of Figures 26 and 27.

For all welds, the dendritic structure was columnar with the dendrites growing from both fusion zones and meeting in the weld center. From the weld base to about the head-web area, the primary dendrite arms were essentially parallel to the longitudinal axis of the rail. In the head-web and head areas, the primary arms were oriented at an upward angle of about 45° . This is due to the head, with the pouring cup

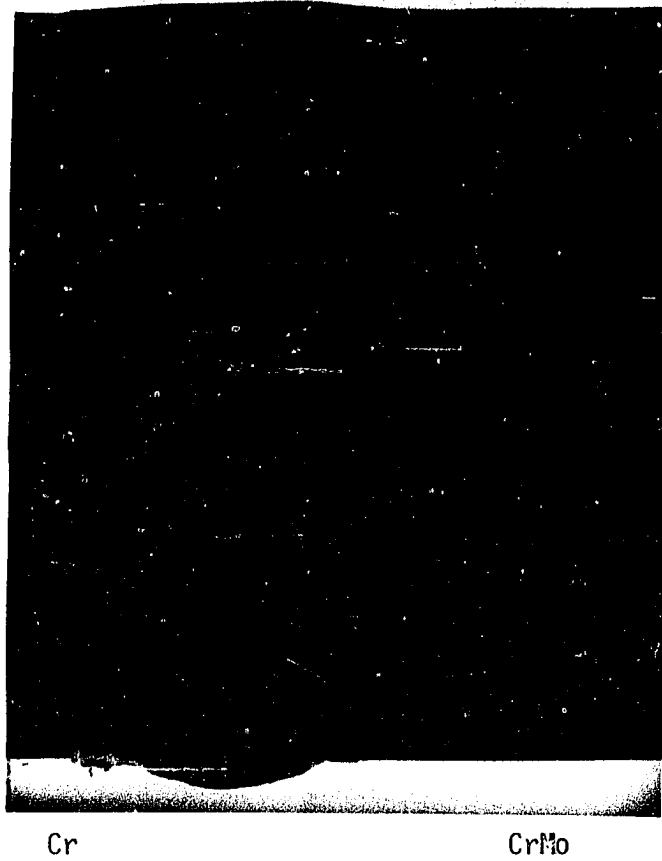


Figure 26: Macrostructure of weld 2-alloy weld metal. Note the thermocouple locations. Approximately one-half size.



Figure 27: Macrostructure of weld 10 showing the effect of a long preheat. Approximately one-half size.

located directly above it, having the greatest melt-back. This results in solidification proceeding inward and upward towards the cup, as reflected by the dendrite growth direction.

Some macroetches displayed slight pitting along the weld centerlines; however, this was not attributed to porosity. Rather, the pitting was determined to be due to preferential etching. Weld 14 displayed a slight depression along the top of the weld metal. This was caused by improper removal of the pouring cup and sprue from the weld.

Welds 7, 11 and 14 exhibited macroinclusions in the weld. In welds 11 and 14, these inclusions were located at about the web center along the fusion zone, approximately where the mold for the weld contacted the rail. They were about 6 mm in diameter and appeared to be alumina with silicate. Weld 7 displayed a similar inclusion in the top of the base. Also, a black iron oxide inclusion of similar size was noted in this region. In addition, a large alumina/silicate inclusion, 10 mm x 6 mm x 6 mm deep, was noted in the web-center of this weld, where contact with the mold surface occurs. These inclusions were not analyzed, but had the glassy appearance and color of the alumina slag with evidence of fused and unfused silica. The alumina/silicate inclusions are attributed to trapped alumina slag and sand particles from the mold that either were washed from the mold walls during the pour or were not blown from the mold prior to welding. The iron oxide is probably unreacted material from the thermite charge.

The width of the HAZ was essentially constant for all welds at 30-33 mm with respect to the fusion zone at the location of the hardness profile. The HAZs of the welds with a long preheat were about 2 mm

wider than the HAZs of welds produced with standard preheat. Otherwise, the width of the HAZ was essentially independent of the welding parameters.

4.2.2 Microstructures. The results of the microstructural analyses are summarized in Appendix B and Figure 28, with representative structures shown in Figures 29-33. The linear regression analysis used to arrive at the lines in Figure 28 is given in Appendix A.

As evident in Appendix B, structures ranged from essentially all pearlite to all transitional pearlite with small amounts of bainite in the fusion zones. The microstructures were characterized after consulting Smith and Fletcher (89). According to them, transitional pearlite has ordered lamellae; further, of the constituents given in Appendix B, it has the greatest strength, hardness and ductility (89). Bainite has a coarser carbide distribution than transitional pearlite, so that its hardness and strength are somewhat less. Examples of pearlite, transitional pearlite and bainite are shown in Figures 31 and 32.

Since transitional pearlite and bainite are stronger and harder than pearlite, Figure 28 was prepared to show the effects of these constituents on the hardness of thermite rail welds. This figure shows that hardness does increase with increasing amounts of transitional pearlite and bainite in the weld metal, in the heat affected zones and in the rail. However, for any fraction of transitional pearlite and bainite, alloy material (alloy rail and alloy weld metal) is approximately 9 R_c points harder, on the average, than standard material (standard rail and standard weld metal).

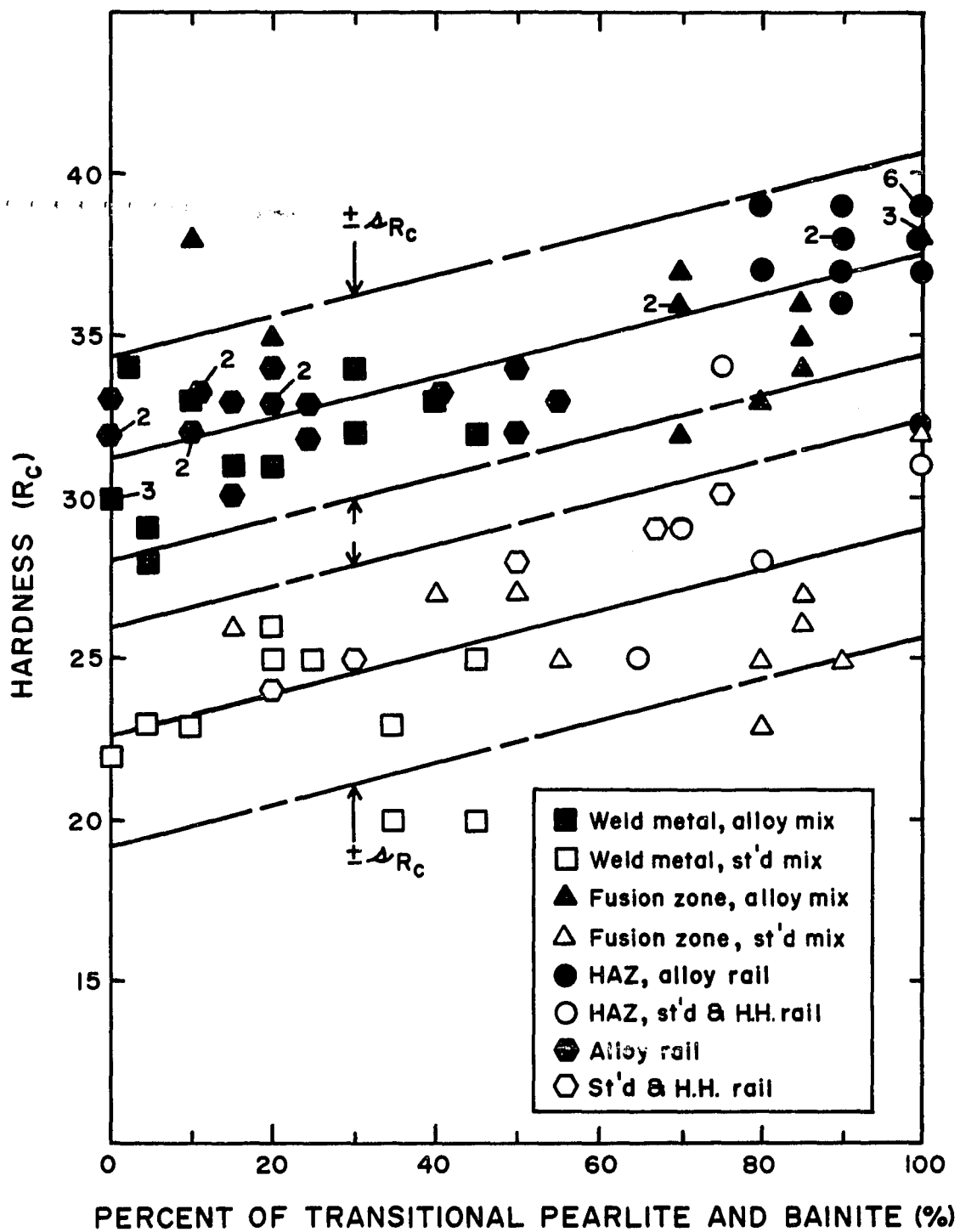


Figure 28: Hardness as a function of the percent of transitional pearlite and bainite at various locations in the rail welds.

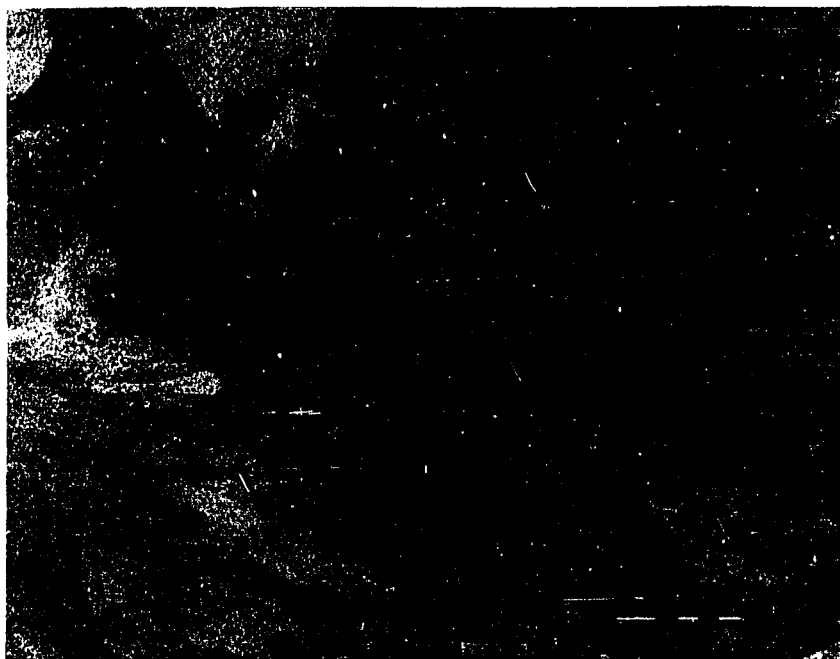


Figure 29: Proeutectoid ferrite in the weld metal of weld 6. 450X.

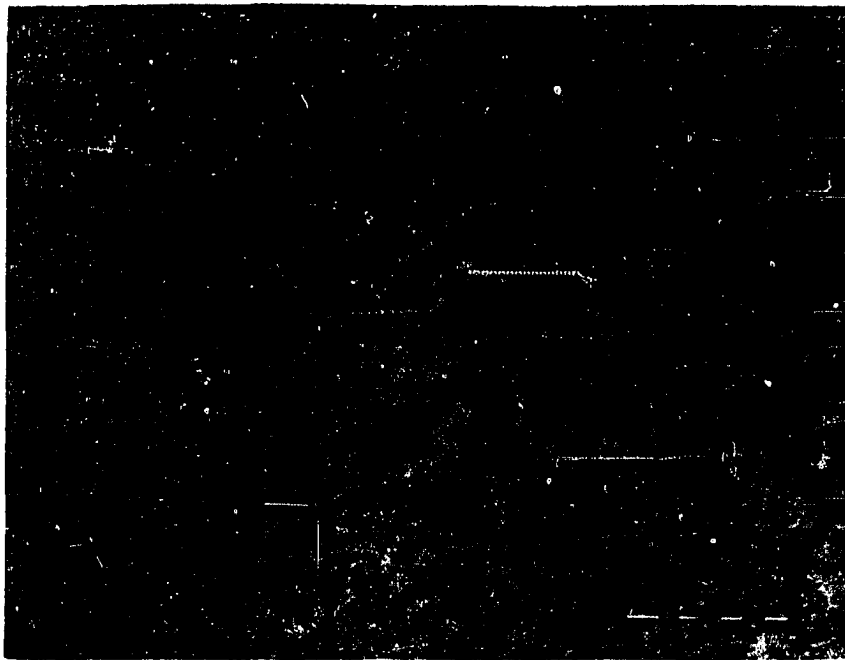


Figure 30: Alumina (with silica) inclusions in the CrV fusion zone of weld 6. The weld metal is to the right of the inclusions. 32X.



(a)



(b)

Figure 31: Pearlitic structure (a) and transitional pearlite and bainite (b) in weld metal of weld 14. 4500X.



Figure 32: Very fine transitional pearlite in the HAZ of the Cr rail of weld 1. 4500X.

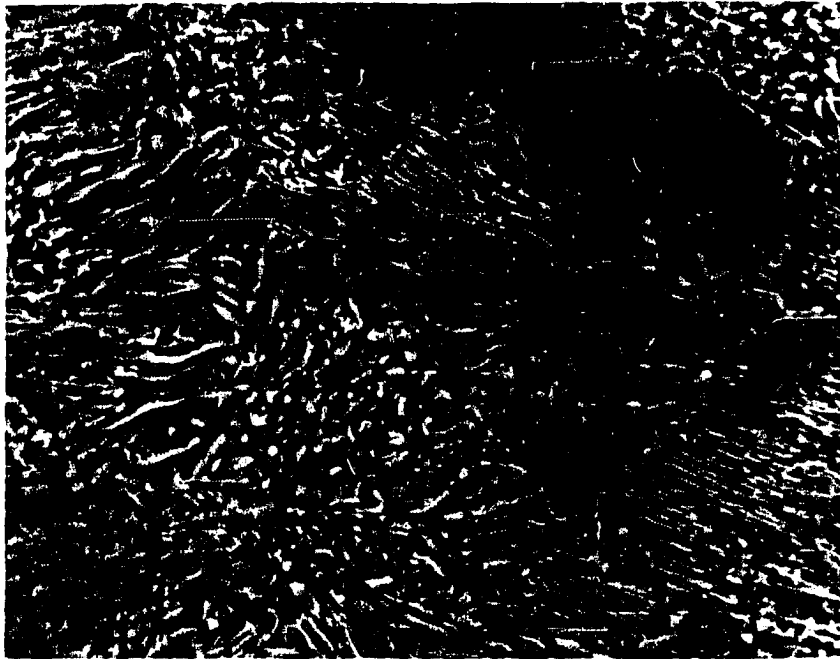


Figure 33: Spheroidite and degenerative pearlite in the outer edge of the HAZ of the HH rail of weld 7. 4500X.

With regard to the microstructure of weld metal, the most obvious difference between alloy weld metal and standard weld metal is the proeutectoid ferrite, evident in Figure 29, which was present only in standard weld metal. While the lower strength of ferrite contributes to the difference in hardness between standard and alloy weld metal, it is doubtful that this factor alone accounts for the difference of 9 R_C points. Further, the fact that the hardness difference holds for rail as well as for weld metal indicates that these discrepancies cannot be attributed to structures observed with the SEM. Other factors, possibly ferrite strengthening associated with the alloy material must be responsible for the observed differences.

The regions of minimum hardness in the outer edges of the HAZ were composed of spheroidite and degenerative pearlite; the latter is a structure with remnants of lath-like carbides. Such a structure is shown in Figure 33.

Finally, some large inclusions, 170-420 μ , were observed along the fusion zone in welds 6 and 10, Figure 30. In weld 6, the EDS analysis indicated that inclusions were rich in alumina and silica. The inclusions in weld 10 also contained alumina and silica with a significant amount of manganese sulfide.

4.2.3 Inclusion Evaluation in Rail Welds. Quantitative image analysis was performed on the weld metal in six welds for the purpose of determining inclusion volume fraction. The location of the inclusion evaluation surface was approximately at the center of the weld, 2.5 cm below the running surface and parallel to the surface.

The parameters and results of the evaluation are listed in Table 12. The fields of view were selected at random with the exception that when microporosity was observed in a field, this field was disregarded and another selected. The volume fraction of inclusions for a sample was based on the mean inclusion area and the total observations for that sample. Confidence limits were established using the basic definitions of expected value and variance for the volume fraction and the Student's t-distribution (90).

Inclusion content varied from 0.24 percent to 0.49 percent and seemed to be independent of the welding process variables. Table 12 also indicates that the welds with the higher volume fraction of inclusions have the larger inclusions with the greater dispersion (standard deviation from the mean size).

Welds 5 and 6 represented the standard weld composition after standard and long preheats, respectively. Weld 7, a standard weld, was evaluated because several macroinclusions were observed during sectioning for the macroetch. Among these three welds, no obvious differences were noted on the micro-level. Welds 13 and 14 represent alloy weld metal for standard and long preheats, respectively. Weld 12, an alloy weld, was produced with a premature tap, and as a result, a high inclusion level was expected. As evident in Table 12, this was not the case. Thus, these measurements indicate that the inclusion level is approximately 0.2-0.5 volume percent in thermite welds. This factor could account for, at least in part, the lower fracture ductilities of the tensile specimens reported in Table 7 and Figure 12.

Table 12. Inclusion Content of the Weld Metal in the Rail Welds

Magnification: 400X, Fields per sample: 10
 Area per field: 257,600 μ^2 (0.26 mm²)
 Feature area range: 0-400 μ^2

Weld	Total No. of Features Observed, n	No. of Features with Area > 400 μ^2 *	Size: (μ^2)			Volume Fraction, V_v (%)	95% Confidence Limits on V_v (%)	
			mean, \bar{x}	St'd deviation, s	max.			
5	196	11	38.7	52.4	280.7	0.294	0.239 < V_v < 0.350	
6	162	10	69.4	86.3	371.5	0.436	0.353	0.520
7	162	3	57.6	77.7	369.2	0.362	0.287	0.437
12+	157	4	45.2	67.8	379.8	0.276	0.211	0.340
13	151	9	40.8	63.2	327.3	0.239	0.180	0.299
14	168	9	75.3	91.4	383.0	0.491	0.401	0.581

* Primarily microporosity.
 + Premature tap.

4.3 Thermal Measurements

Thermocouples were positioned in the rails of welds 1-4 and in weld metal of weld 9. Figure 34 shows the temperature as a function of time for weld 1. The numbers on the curves refer to the thermocouples located at the respective positions shown in Figure 3. The locations nearest to the rail end (thermocouples 1-5), of course, respond most rapidly and achieve the greatest peak temperatures after the molten charge is tapped at 145 s. All curves exhibit peak temperatures, and some of the curves show thermal arrests or retardation of cooling due to the transformation of austenite upon cooling through the temperature range of 1000°K to 810°K (1340°F to 1000°F). Curve 2 shows a sudden temperature fluctuation at about 370 seconds. This is attributed to the removal of the mold, and, at this time, excess metal (feeders and gates) are removed from the solidified weld metal by torch cutting. By wrapping the muffle on the weld (750 s) the cooling rate is decreased somewhat; the decrease is particularly evident for the thermocouples located in the rail head (thermocouples 1, 6 and 11).

Figure 35 shows the measured temperatures in the weld metal of weld 9. At 125 s, the preheating torch was removed, and the charge was tapped at 150 s. During preheat, the temperatures shown in Figure 35 do not reflect the true preheat rail temperatures due to the combined effects from the gas flame and radiant energy from the heated rail ends. These temperatures dropped as soon as the torch was removed, just prior to tapping at 150 seconds, and, of course, increased very rapidly as the thermite charge was tapped.

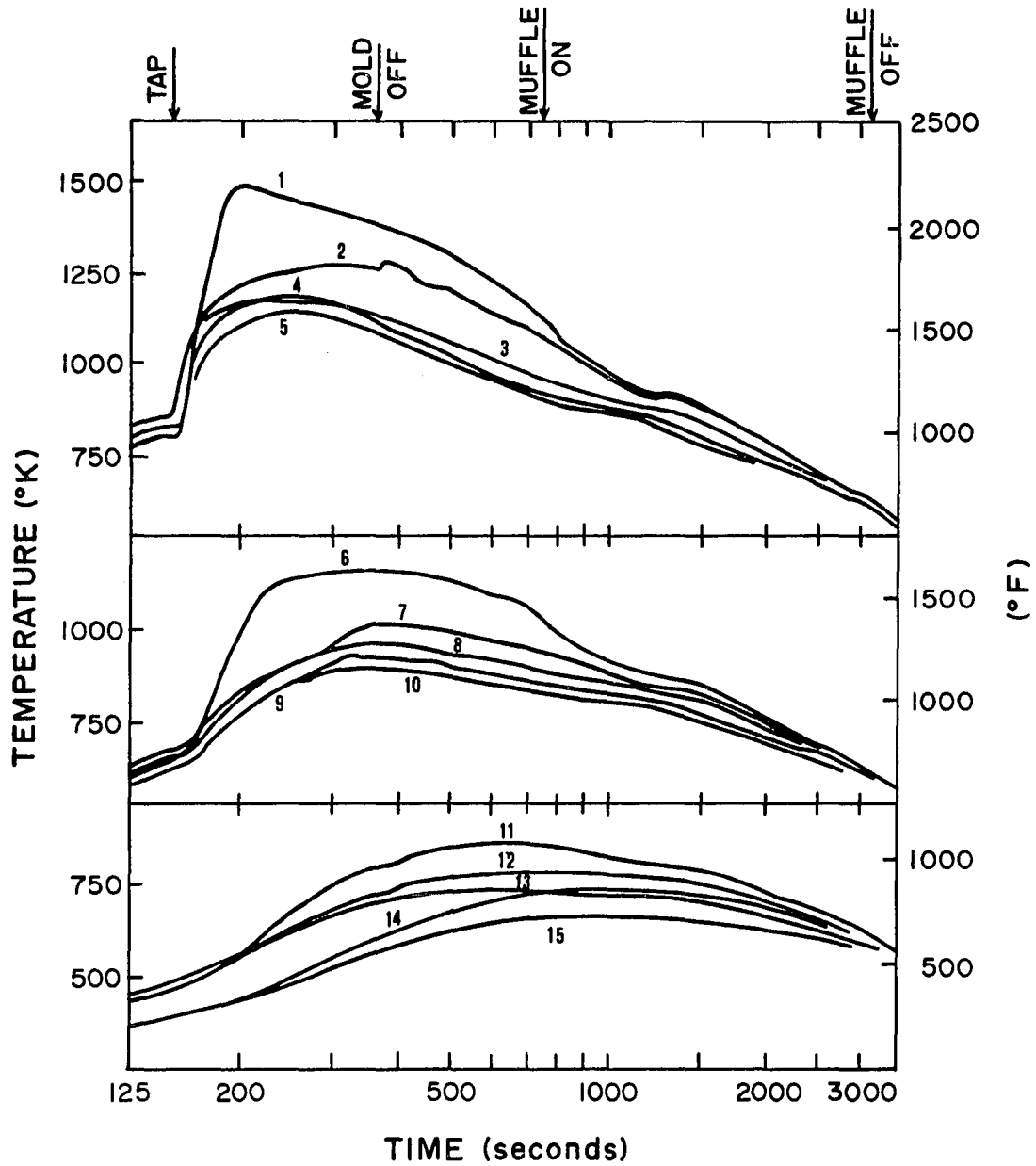


Figure 34: Temperature as a function of time and position in the rail during the welding process for weld 1. Refer to Figure 3 for the locations of the thermocouples.

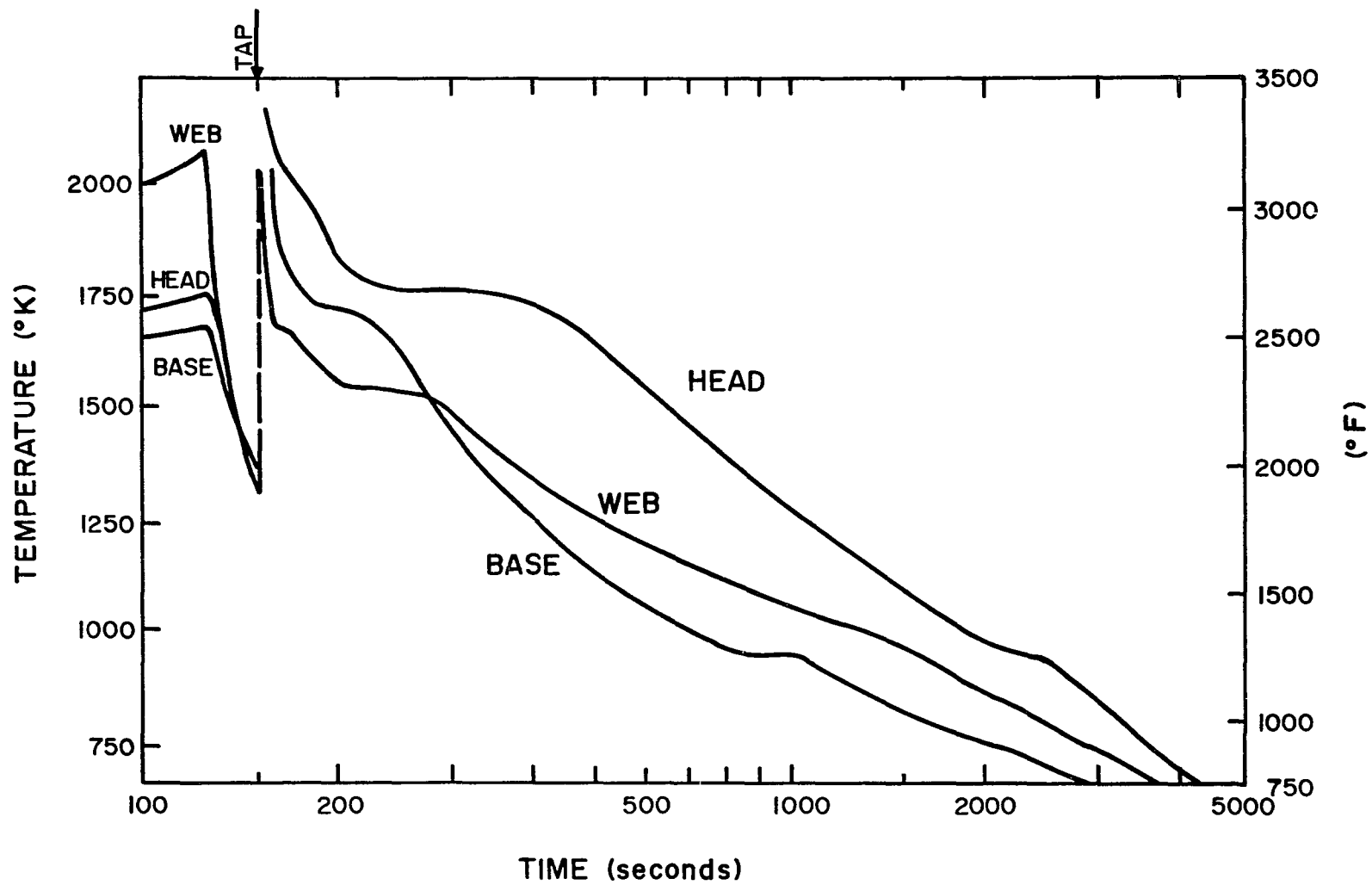


Figure 35: Temperature as a function of time and position in the weld metal of weld 9. Refer to Figure 4 for the locations of the thermocouples.

Thermocouple output was monitored continuously by the strip chart recorder and at discrete intervals (every 2-3 s) by the data acquisition system. Data from each system were in agreement except for the peak temperatures at tapping. The strip chart data, being continuous, were used for these values. The discrepancy is attributed to the time interval between readings for the data acquisition system. It is difficult to ascertain the exact temperature at tapping, but the maximum recorded temperature is 2140°K (3400°F) at position A in the rail head, so the tapping temperature is at least of that magnitude. While all three thermocouples indicate tapping temperatures well above the liquidus, cooling at the B and C positions was very rapid, so that the true tapping temperatures at these positions were probably not recorded.

The heaviest mass of weld metal is in the rail head, and so the thermal arrest at approximately 1760°K (2700°F) and 250 seconds shown for the head is the arrest closest to the liquidus temperature of the weld metal. The corresponding portions of the other two curves are also due to the heat of solidification, but these curves reflect that the heat was evolved at locations removed from the web and the base. Consequently, the indications of freezing on these cooling curves are well below the liquidus temperature of the alloy. The curves for the head and base also show evidence of the transformation of austenite at 950°K (1250°F) during cooling.

Figures 36-38 summarize important features derived from the thermal measurements for welds 1-4. Figure 36 shows the temperature distribution in the rails at the end of the preheating period. At a given distance from the end of the rail, preheat temperature is almost

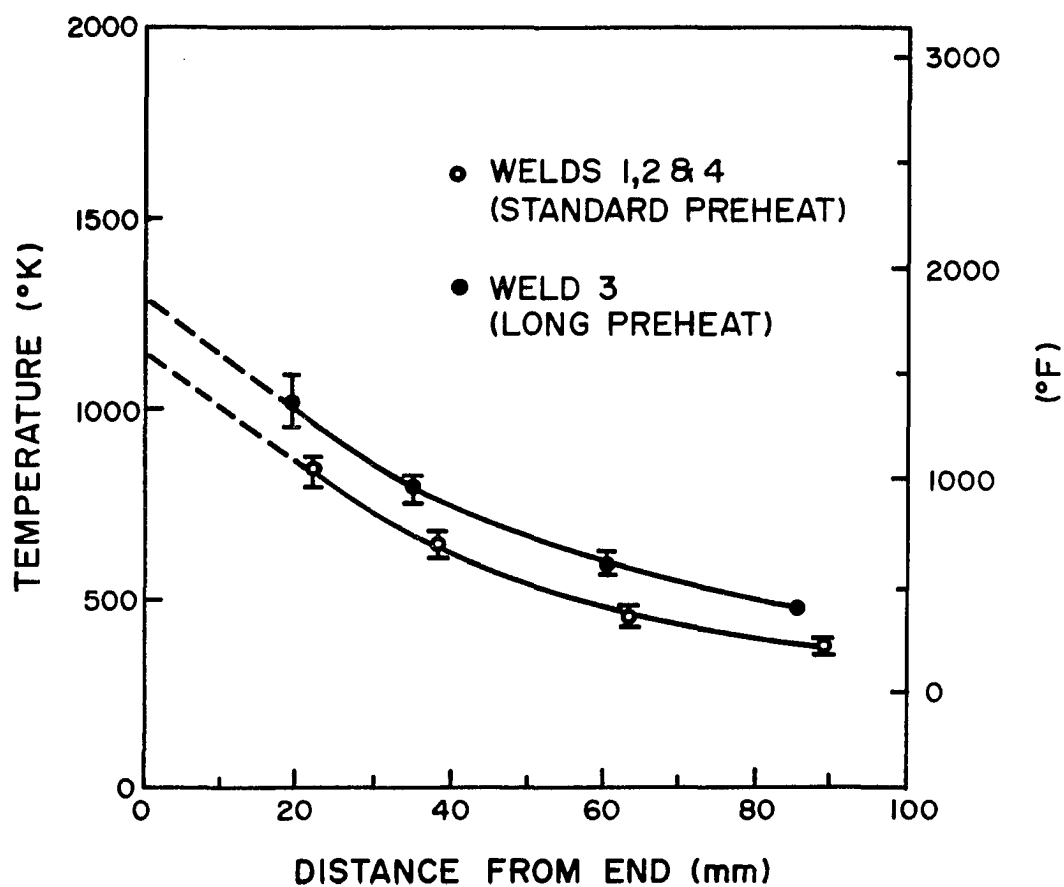


Figure 36: Rail temperature distributions at the end of preheat. Curves are extrapolated to the rail end.

uniform from the head down to the base. In Figure 36, data are combined for welds 1, 2 and 4 because they were preheated for the same period (2 minutes). A longer preheat of 3 minutes (weld 3) increases the pre-heat temperature distribution somewhat, and causes an increase in the width of the weld metal region and a decrease in cooling rate through the critical range for the austenite transformation. Both curves are extrapolated by assuming that

$$\ln (T-T_a) \text{ vs } x/(2\sqrt{\alpha\tau})$$

is linear for $x/(2\sqrt{\alpha\tau}) < 0.5$ where

x = distance from the end of the rail,

α = thermal diffusivity,

τ = time,

T = temperature at x , and

T_a = ambient temperature.

This assumes that during preheat, heat flow in the rail is one-dimensional, and that the rail is infinitely long with the end heated by a convective environment. Such a solution is available in heat transfer texts (e.g., see Geiger and Poirier (91) or Schneider (92)). From the extrapolations, it appears that no melting of the rail end occurs after preheat times of 2 and 3 minutes.

Figures 37 and 38 show the peak temperatures in welds 1-4. These plots were derived from the maximums of the curves of temperature versus time as shown, for example, in Figure 34 for weld 1. Figure 37a gives peak temperatures for weld 1. Notice that the peak temperatures decrease with increasing distance from the end; this is predictable

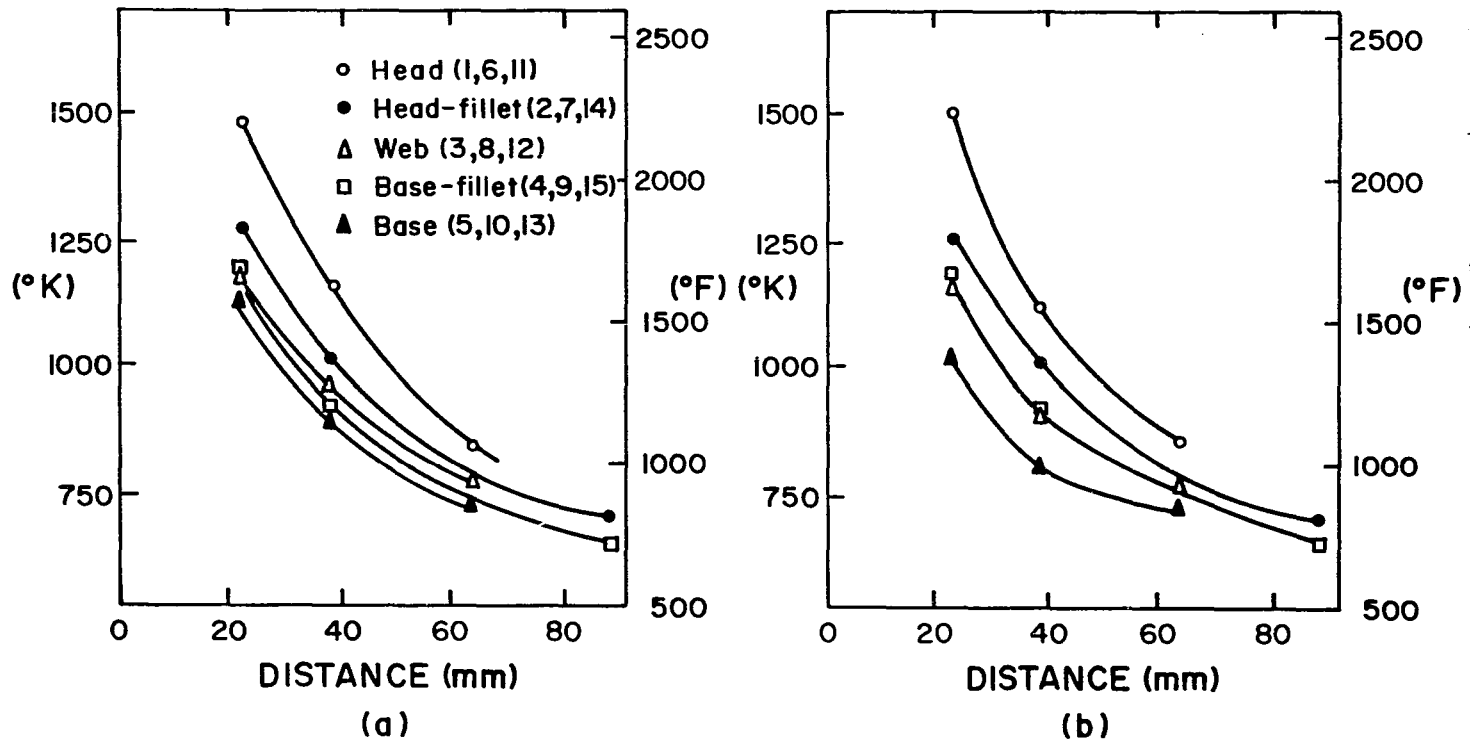


Figure 37: Peak temperatures as a function of distance from the rail end: (a) weld 1; (b) weld 2. Standard preheats. The numbers in parentheses identify the thermocouple locations shown in Figure 3.

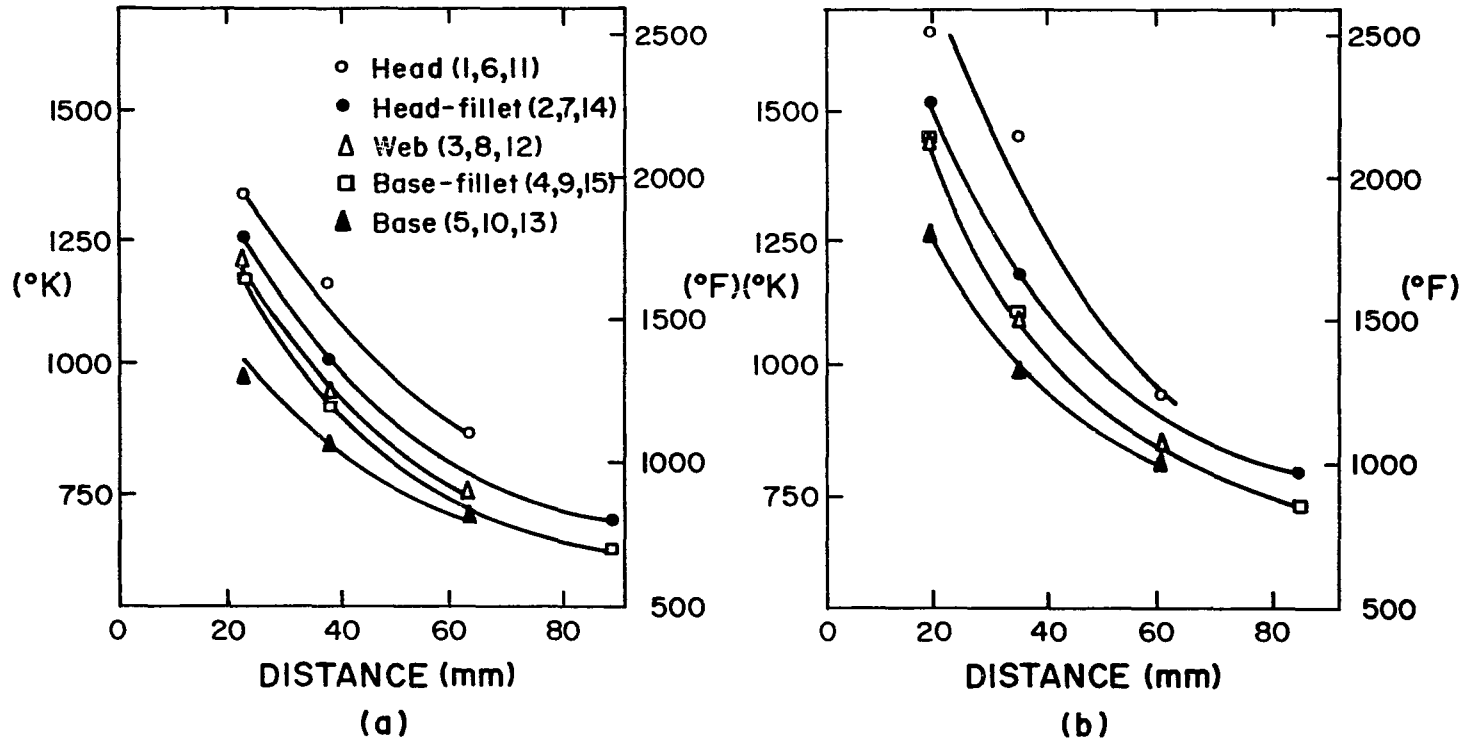


Figure 38: Peak temperatures as a function of distance from the rail end: (a) weld 4 - standard preheat; (b) weld 3 - long preheat. The numbers in parentheses identify the thermo-couple locations shown in Figure 3.

based upon the thermal behavior normally associated with welding processes. Also, peak temperatures are the greatest in the head, and they decrease in a regular manner from the head to the base. The same behavior of peak temperature in welds 2-4 can be seen in Figure 37b and in Figures 38a and 38b. The effect of a longer preheat is evident for weld 3 (Figure 38b); peak temperatures in this weld are the highest of the four given in Figures 37 and 38.

Finally, Table 13 has been prepared to show the thermal characteristics of the welds as they cooled through the temperature range of 1000°K to 810°K (1340°F to 1000°F); within this range, the austenite transforms. Along with data derived from welds 1-4, data from Figure 35 are included. The latter represents the characteristics of the cooling of weld metal. Table 13 illustrates that the average cooling rates through the specified temperature range are comparable within the weld metal and within the heat-affected zones although they are somewhat less in the head and web of the weld metal. The slowest cooling shown for these welds is 1380 s in the weld metal of weld 9. Weld 2 was produced with no muffle, and it, in fact, cooled somewhat faster than welds 1, 3 and 4. Weld 4, while produced with the muffle, cooled noticeably faster than welds 1 and 3 and, in fact, has rates that approach those of weld 2, while the preheat temperatures of welds 1, 2 and 4 are comparable, Figure 36, the peak temperatures of weld 4, particularly in the head near the rail end, are on the order of 150°K lower than for welds 1 and 2, Figures 37 and 38a. These lower peak temperatures would account for the faster cooling rates of weld 4 in Table 13, particularly in the head. These lower temperatures for weld 4 are probably due to a

Table 13. Time in the Transformation Range During Cooling

Position		Distance From End, mm	Time Between 1000°K and 810°K; seconds				Weld 9 (mold in place)
			Weld 1 (muffle)	Weld 2 (no muffle)	Weld 3 (muffle)	Weld 4 (muffle)	
Head	1	22 (19*)	920	590	1000	690	--
	6	38 (35*)	940	600	1020	790	--
Head- Fillet	2	22 (19)	960	620	960	660	--
	7	38 (35)	1100	700	1020	960	--
Web	3	22 (19)	1040	720	1010	870	--
	8	38 (35)	--	--	1050	--	--
Base- Fillet	4	22 (19)	900	770	950	800	--
	9	38 (35)	--	--	1050	--	--
Base	6	22 (19)	840	720	910	--	--
	10	38 (35)	--	--	--	--	--
Weld Met.							
Head			--		--		1380
Web			--		--		1140
Base			--		--		880

*In weld 3, the thermocouples were located at 19 and 35 mm; in welds 1, 2 and 4, they were located at 22 and 38 mm.

suppressed thermite reaction peak temperature. This weld was the second of the day (ambient of +6°C) so that crucible preheat should not have been a problem. No adverse effects on the properties of weld 4 were noted. Finally, there is no significant effect of a longer preheat (weld 3) on cooling from 1000°K to 810°K (1340°F to 1000°F), although the width of the zone of weld metal is increased by increasing the time of preheating.

4.4 Residual Stresses

Residual stresses were determined by the blind hole technique for weld 11 at the locations shown in Figures 6 and 39. The principal stresses and their orientations relative to the vertical centerline are given in Table 14 and shown in Figure 39. In Figure 39, the principal stresses are shown as vectors with lengths proportional to the respective scalars.

The residual stresses for the weld metal, locations E, C, F, D and O, agree with the findings of Dohse (77) and others (26, 78) in that the head and base areas are in compression while the web area exhibits tensile residual stresses. The compressive stresses in the head, head-fillet and base-fillet areas are relatively high, on the order of -270 MPa, while the tensile stresses in the web are relatively low, on the order of +60 MPa.

A lack of symmetry is noted for the stress fields in the HAZs on both sides of the weld metal. This is particularly evident in the locations selected for the web region (L, J, B and H). In going from location L to J, a transition from a compressive-tensile state to a

Table 14. Principal Residual Stresses in Weld 11

Gage Location	Principal Stresses MPa (ksi)				Orientation of σ_p from the Weld Vertical Centerline θ , +ccw, -cw, Degrees Δ	Comments
	σ_p		σ_q			
E	-285.4	(-41.4)	-160.6	(-23.2)	+1.30*	Head running surface
M	-56.5	(-8.2)	-154.4	(-22.4)	+15.90	Head side
K	-22.8	(-3.3)	+147.6	(+21.4)	-38.70	Head-web fillet
I	+3.4	(+0.5)	+129.6	(+18.8)	-36.20	Head-web fillet
C	-229.2	(-43.4)	-271.0	(-39.3)	-34.00	Head-web fillet
A	-88.3	(-12.8)	+33.8	(+4.9)	+36.90	Head-web fillet
G	-96.5	(-14.0)	+128.2	(+18.6)	+34.60	Head web fillet
L	+109.6	(+15.9)	-94.5	(-13.7)	-44.30	Web
J	-206.8	(-30.0)	-82.7	(-12.0)	-23.60	Web
F	+52.4	(+7.6)	+26.2	(+3.8)	-1.95	Web
D	+69.9	(+10.1)	-40.0	(-5.8)	-7.25	Web

Δ Ccw - counterclockwise, cw - clockwise.

* Ccw from the longitudinal center of the rail when viewed from above.

Table 14--Continued

Gage Location	Principal Stresses MPa (ksi)				Orientation of σ_p from the Weld Vertical Centerline θ , +ccw, -cw, Degrees Δ	Comments
	σ_p		σ_q			
B	-48.3	(-7.0)	-12.4	(-1.8)	+17.45	Web
H	-336.5	(-48.8)	-115.8	(-16.8)	-40.40	Web
N	-18.6	(-2.7)	+151.0	(+21.9)	+33.90	Base-web fillet
O	-251.0	(-36.4)	-146.2	(-21.2)	+0.75	Base-web fillet

Δ Ccw - counterclockwise, cw - clockwise.

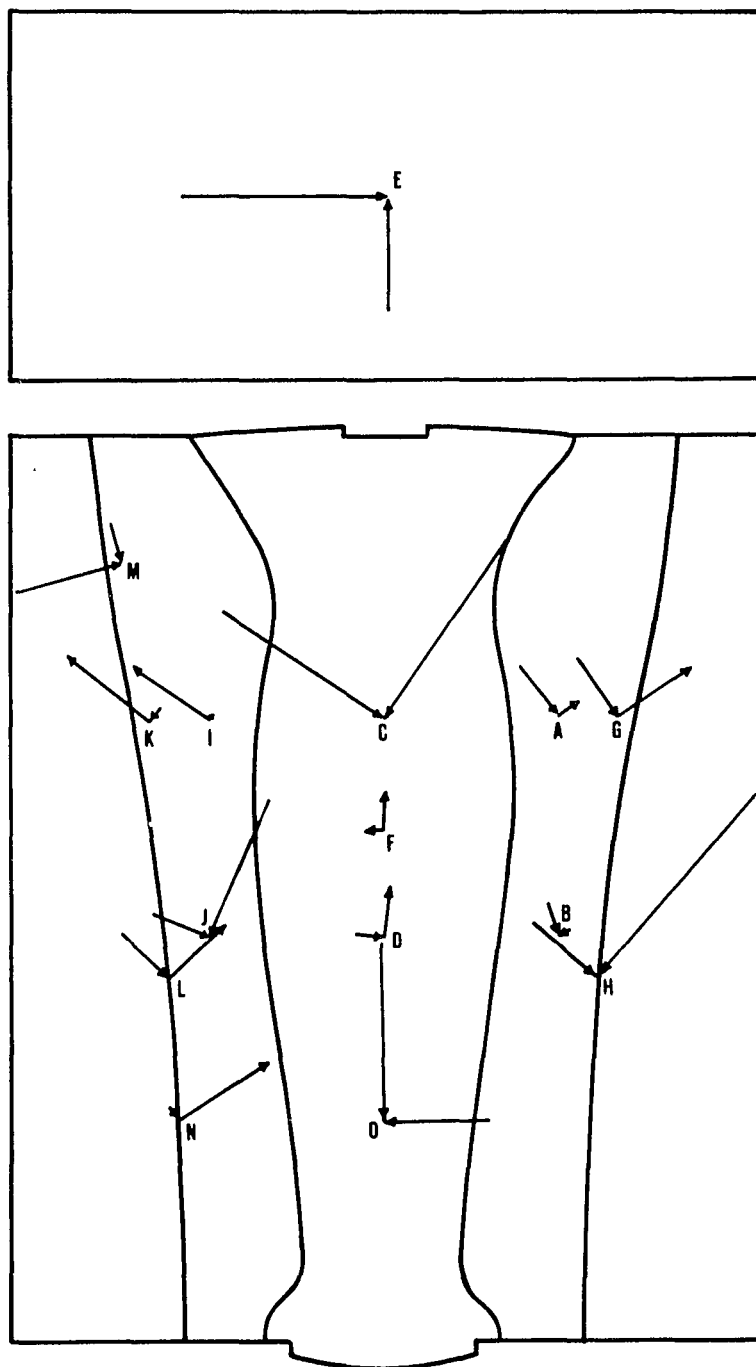


Figure 39: Principal residual stresses in weld 11. The lengths of the vectors are proportional to the magnitudes of the stresses. The letters correspond to the locations of the rosettes shown in Figure 6.

compressive state occurs. At L, the maximum principal stress is +110 MPa and at J, a compressive maximum of -270 MPa occurs. In the opposite side of the weld and in the web HAZ, no tensile stresses are observed at locations B and H. At B, a low compressive state exists, -48 MPa maximum, but at H, a high compressive state occurs, with a maximum of -335 MPa exhibited.

In contrast, the stress fields in the HAZ of the head-fillet area (locations K, I and A, G) are relatively symmetrical. At both K and I, the maximum principal stress is about +145 MPa. At A, the tensile stress is relatively low at +34 MPa while at G, a value of +128 MPa is observed. The compressive stress at K is insignificant, and at I the material is in a tensile-tensile state, with one principal stress essentially equal to zero. At A and G, the compressive-principal stresses are about -90 MPa.

The residual stresses in the head are compressive. Specifically at location M, the maximum compressive stress is -154 MPa, and at location E, on the head running surface, the maximum compressive stress is -285 MPa. Finally at N, the greatest tensile residual stress is observed, +151 MPa.

The residual stresses observed in the HAZs are considered significant since they approach 25 percent of the yield strength and 15 percent of the ultimate strength of the unwelded rail steel, 600 MPa and 950 MPa, respectively (7). Further consideration should be given to the fact that the HAZ material is no longer in the 'as produced' state. Tensile data from the standard rail portion of welds 4 and 5, produced under similar conditions as weld 11, show that the yield strength of the

outer edge of the HAZ is 474-548 MPa, and the ultimate strength is 857-885 MPa; these values are significantly lower than for the unwelded rail. Thus, the residual tensile-stresses in the outer edge of the HAZ exceed 25 percent of the yield strength in the web, and they are also significant in the head fillet and base fillet regions.

If the fatigue limit is estimated as 45 percent of the ultimate strength, then the residual tensile stresses are on the order of 15-20 percent of the fatigue limit of the region of minimum hardness in the outer edge of the HAZ. Note that this estimate for the fatigue limit does not take into consideration the effects of preexisting defects. Based on Sato's (54) findings, these tensile residual stresses could be about half of the fatigue limit. Given the flexural loading of these welds in field service, it is felt that the tensile residual stresses contribute to the initiation and propagation of fatigue cracks in the HAZ and particularly in the region of minimum hardness.

5. RESULTS AND DISCUSSION OF PLATE WELDS

Based on the evaluation of the rail welds and the previous studies of Myers (7), it was felt that properties of the weld metal could be improved by reducing the size and volume fraction of inclusions. The approach chosen to accomplish this was to pass the molten thermite steel through various filtration systems, as shown in Figure 7, and outlined in Table 4. None of these attempts to filter the thermite steel was completely successful in that the filters were partially dissolved. Even so, there is some evidence that the weld metal of filtered steel contains fewer inclusions.

The structure and properties of the weld metal of plate welds were evaluated in the as-cast state and after normalizing. Normalizing was done in order to study the effect of a relatively simple heat treatment on the tensile properties of weld metal. In this regard, normalizing was very effective in grain refining the as-cast structure of the weld metal and in improving tensile properties.

5.1 The Effects of Filtering

Figure 40 shows a portion of a ceramic filter before use and two sections through a filter after use. It can be seen that much of the filter has been dissolved. It appears that the slag, entrained in the thermite steel, has reacted with the ceramic filters. This is likely since the slag is rich in alumina and the ceramic filters are approximately 65 wt. pct. zirconia and 35 wt. pct. mullite. Cracking is not



Figure 40: Cross-sections of the filter system for weld 9-X. From top to bottom: filter A before use; filter B after use; vertical section showing remnants of filter A, the beads and filter B.

thought to be the cause of the failure of the filters since the portions of the filters which survived showed no cracks, and the filters are used in current ferrous and nickel-base casting technologies.

Quantitative image analysis was performed on the weld metal from the plate welds for the purpose of determining inclusion volume fraction. The location of the evaluation was approximately at the center of the weld and 13 mm below the top surface of the welded plates. The procedures applied in obtaining and reducing the data were the same as those applied to evaluation of inclusions in the rail welds. These results are given in Table 15. In Table 15, welds 5-X and 6-X should be disregarded since they were made with a tapping time of 61 s rather than the recommended and usual period of 18-28 s. This resulted in welds with incomplete fusion to the plates. The remaining welds exhibit 0.36 volume percent of inclusions when no filter was employed to lesser amounts with a filter. Welds 3-X and 4-X, produced with only one filter in place (Table 4), have about 0.28 volume percent of inclusions. Together with the unfiltered welds, these inclusion contents and mean inclusion sizes are comparable to those reported for the rail welds (Table 12) whereas welds 7-X, 8-X and 9-X have inclusion contents and mean inclusion sizes somewhat less than observed for the rail welds. Thus, it appears that with multiple filters there is some effectiveness in removing inclusions from the weld metal. It should be pointed out, however, that application of confidence limits to the volume fraction of inclusions does result in overlap between these welds and the unfiltered and once-filtered welds.

Table 15. Inclusion Content of the Weld Metal in the Plate Welds

Magnification: 400X; Fields per sample: 10

Area per field: 257,600 μ^2 (0.26 mm²)

Feature area range: 0-400 μ^2

Weld	Total No. of Features Observed, n	No. of Features with Area > 400 μ^2 *	Size: (μ^2)			Volume Fraction, V_V (%)	95% Confidence Limits on V_V (%)	
			mean, \bar{X}	St'd deviation, s	max.			
1-X	221	3	42.5	62.2	395.0	0.365	0.294 < V_V < 0.435	
2-X	275	3	34.0	54.6	366.0	0.363	0.294	0.432
3-X	146	6	51.7	76.3	399.2	0.293	0.223	0.363
4-X	154	10	46.6	85.9	384.0	0.279	0.197	0.360
5-X+	231	2	52.1	59.0	324.1	0.467	0.399	0.535
6-X+	183	3	49.0	67.1	343.9	0.348	0.279	0.417
7-X	293	0	23.7	31.9	193.2	0.135	0.114	0.156
8-X	191	3	23.1	39.4	306.6	0.171	0.130	0.213
9-X	158	0	36.7	56.2	380.3	0.225	0.172	0.279

* Primarily microporosity.

+ Low pouring temperature due to 6l s. tap time.

5.2 Mechanical Properties of Plate Welds and the Effects of Normalizing

5.2.1 Hardness Profiles. Hardness measurements were taken across the weld metal and both HAZs for all plate welds except 5-X and 6-X which, as stated above, were disregarded. The measurements were taken 13 mm below the top of the weld. In addition, complete hardness traverses were taken on heat treated specimens, 1-X.3 and 2-X.5, to determine the effects of the extremes of cooling rates from the austenitizing temperature. For the remaining heat treated specimens, hardness measurements were from the central 30 mm of the weld metal. All of these data are given in Tables 16 and 17, and representative hardness profiles are shown in Figures 41 and 42.

Figure 41 displays hardness profiles from as-cast welds produced with and without filtration. In addition to the absence of filtration, 1-X and 2-X indicate that tapered weld gaps had little effect on the final weld profile. The width of the weld metal is virtually unaffected by the wider gap of 2-X; however, the HAZs do appear wider and slightly lower in peak hardness than in 1-X. Weld 7-X was made without any taper and has a width equal to 1-X and 2-X.

Since the hardness levels of the weld metal of welds 7-X, 8-X and 9-X were found to be consistently higher than for welds 1-X, 2-X, 3-X and 4-X, it was first thought that the filters had the effect of increasing the hardness of the weld metal since, ostensibly, the thermite charges of all plate welds were the same. However, chemical analyses of the plate welds show that there are differences in the compositions of the weld metals, which account for the differences in hardness. The compositions of the weld metal of the plate welds are given in Table 18,

Table 16. Hardnesses and Dimensions of Plate Welds

Weld	Hardness of Weld Metal*, R _C	Width of Weld Metal (mm)	Width of HAZs (mm)		HAZ Hardness, R _C				Hardness in Plates, R _C	
					max.	min.	max.	min.		
1-X	23	42	10	10	38	23	39	22	32	33
2-X	23	42	14	14	36	25	35	24	30	30
3-X	21	38	16	16	33	21	32	20	30	32
4-X	21	45	13	13	32	21	32	20	29	29
5-X	26	--	--	--	--	--	--	--	--	--
6-X	27	--	--	--	--	--	--	--	--	--
7-X	28	42	14	12	34	21	35	20	33	31
8-X	29	32	12	12	34	20	33	21	30	29
9-X	28	39	13	18	33	20	33	20	29	29

* Average hardness across 30 mm in the weld metal.

Table 17. Hardness of Plate Welds
After Normalizing

Weld and Cooling Rate Identification	Cooling Rate*, K°/min	Hardness of Weld Metal Δ		Hardness of Plates, R_B	
		R_C	R_B		
1-X.3	12	(11)	92	104	102
4-X.3	12	(9)	90	---	---
1-X.4	37	(11)	92	---	---
4-X.4	37	(11)	92	---	---
2-X.1	54	(14)	94	---	---
3-X.1	54	(13)	93	---	---
2-X.5	154	(20)	98	108	107
3-X.5	154	(19)	97	---	---
7-X.3	12	(16)	95	---	---
9-X.3	12	(17)	96	---	---
7-X.4	37	(19)	97	---	---
8-X.1	54	21	(98)	---	---
8-X.5	154	28	(104)	---	---
9-X.5	154	28	(104)	---	---

* From 1000 to 810°K.

Δ Average hardness across 30 mm in the weld metal.

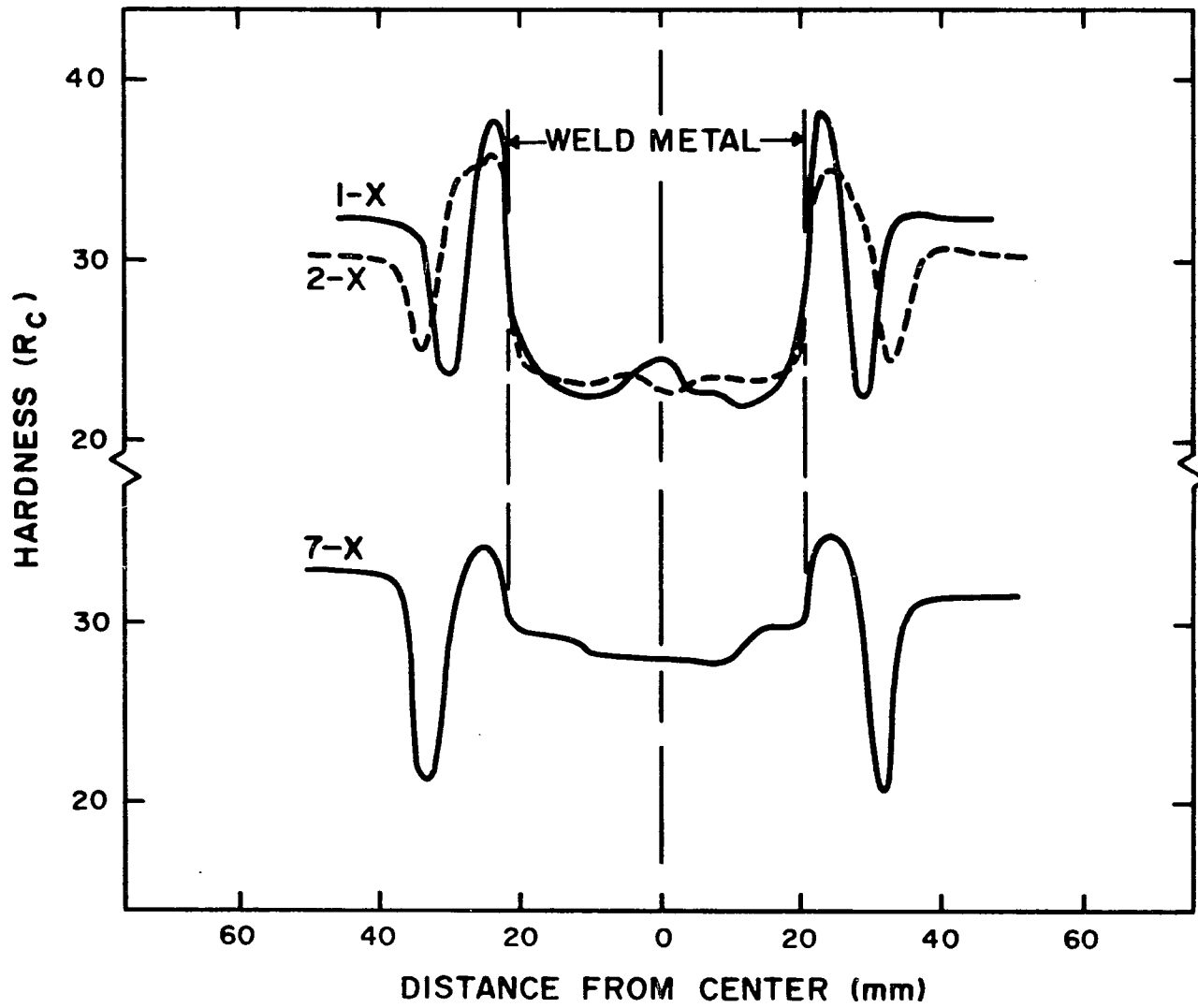


Figure 41: Hardness profiles of welds 1-X, 2-X and 7-X.

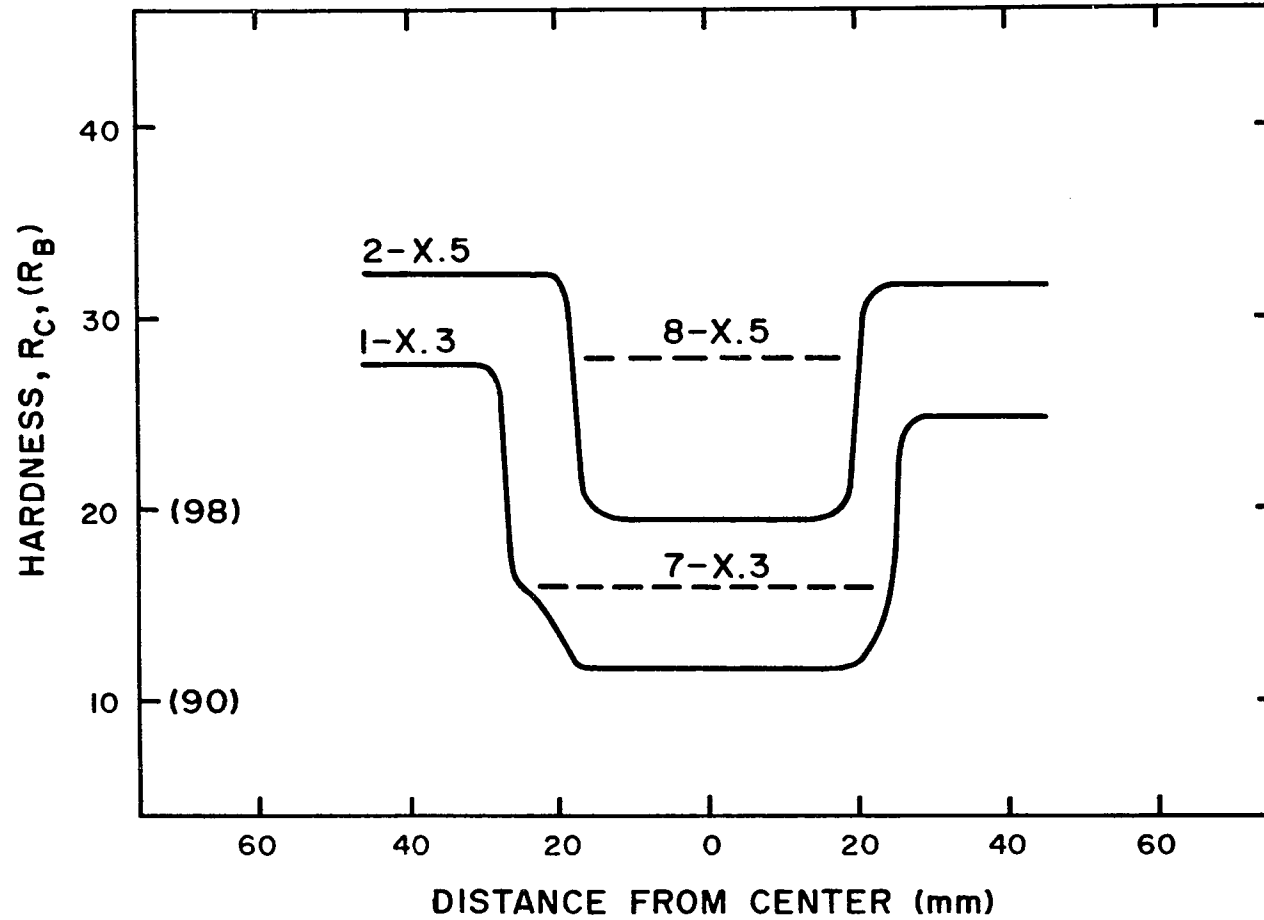


Figure 42: Hardness profiles of welds 1-X.3 and 2-X.5 with the hardness of the weld metal in welds 7-X.3 and 8-X.5.

which shows that the welds of the lower hardness have carbon compositions of 0.44-0.46 percent versus compositions of carbon of 0.52-0.59 percent and of vanadium of approximately 0.06 percent for the harder welds. This is particularly evident in Figure 43, which shows hardness in the as-cast condition and after normalizing with various cooling rates. In Figure 43, there are differences of about 5-8 R_C points, which cannot be entirely attributed to the difference in the carbon compositions. The added hardness, however, can be attributed to vanadium, since vanadium is known to strengthen ferrite as a "microalloying" element. According to Manning (52), the increase in carbon level and the addition of 0.06 percent vanadium could result in a hardness increase of up to 6 R_C points each.

In Figure 42, the effects of the slowest and fastest cooling rates on weld metal and parent plate material are shown. By normalizing, the soft outer edge of the HAZ was eliminated; hardness of the parent metal varies from 102-108 R_B as a result of heat treatment.

5.2.2 Tensile Properties. In the plate welds, tensile properties were determined for the weld metal only, both in the as-cast condition and after normalizing. The results are summarized in Table 19 and in Figure 44, which illustrate the effect of normalizing with the various cooling rates on the tensile properties. In the as-cast condition, the harder welds with the greater composition of carbon have yield strengths which are significantly greater than the softer welds; however, the tensile strengths of both groups are approximately equal. According to Manning (52), the carbon increase could increase the yield strength as much as 21 MPa (3.0 ksi) and, from Pickering (57), 0.06

Table 18. Composition of Weld Metal
in Plate Welds

Element	Weld 2-X	Weld 4-X	Weld 8-X	Weld 9-X
C	0.44 (0.45)	0.46	0.59 (0.59)	0.52 (0.54)
Mn	0.99 (0.97)	1.00	1.04 (0.93)	0.96 (0.99)
P	0.029 (0.030)	0.029	0.027 (0.025)	0.022 (0.024)
S	0.005 (0.007)	0.005	0.006 (0.007)	<0.005 (0.007)
Si	0.29 (0.28)	0.28	0.33 (0.36)	0.38 (0.37)
Ni	0.04	0.03	0.04	0.04
Cr	0.08 (0.06)	0.08	0.06 (0.05)	0.06 (0.05)
Mo	<0.01	<0.01	<0.01	<0.01
Cu	0.04 (0.04)	0.04	0.05 (0.05)	0.05 (0.05)
Al	0.13 (0.14)	0.12	0.16 (0.089)	0.074 (0.063)
Ti	<0.005 (0.003)	<0.005	<0.005 (0.003)	<0.005 (0.003)
V	<0.005 (0.01)	<0.005	0.059 (0.07)	0.058 (0.07)
Nb	<0.005	<0.005	<0.005	<0.005
Zr	<0.005	<0.005	<0.005	<0.005

NOTE: Check analyses from a second analytical laboratory are in the parentheses.

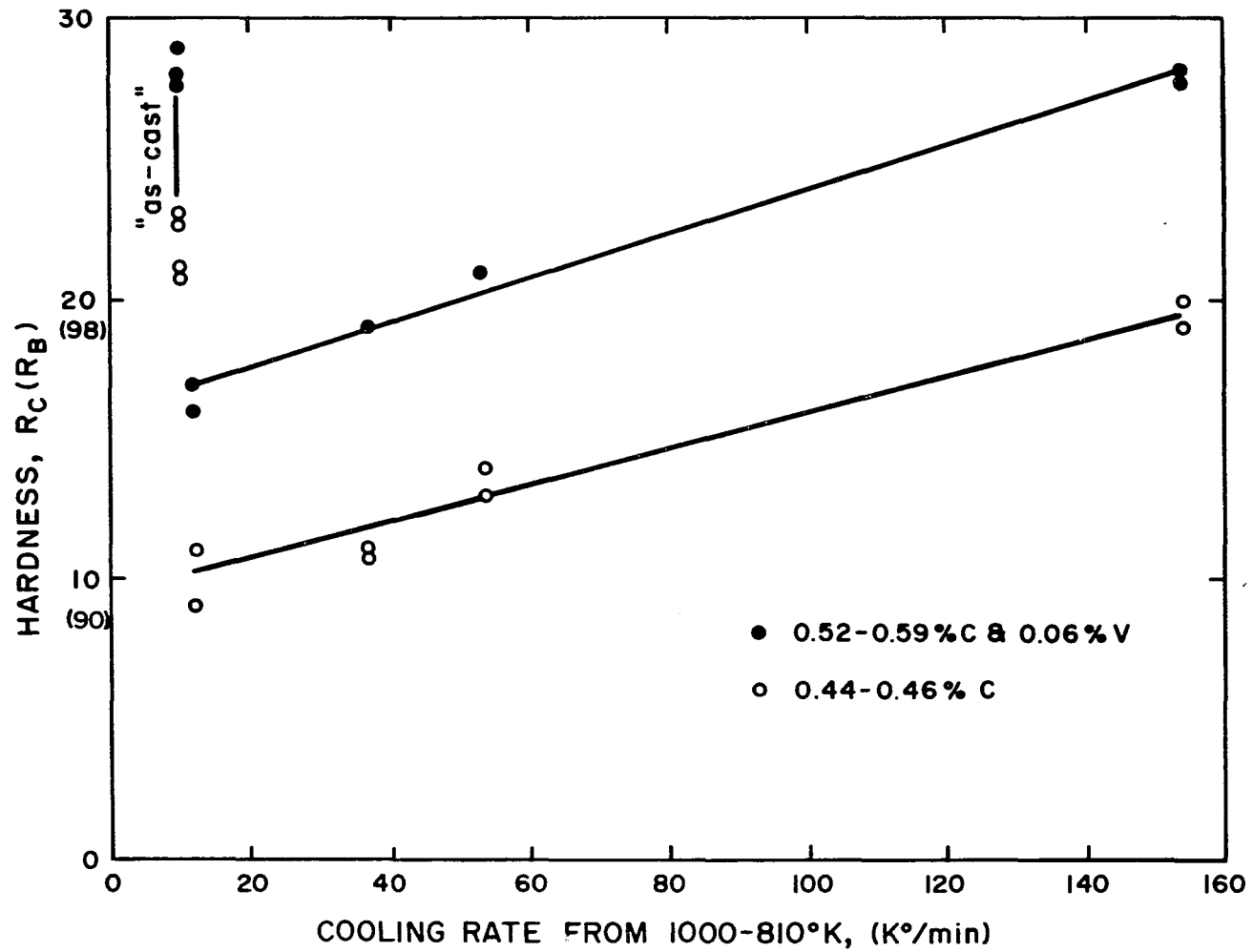


Figure 43: Hardness of the plate weld metal as a function of cooling rate through the transformation range.

Table 19. Tensile Properties of the Plate Welds

Weld	BHN	Yield Strength		Ultimate Strength		True Fracture Strength		Percent Elongation*	Percent Reduction of Area
		0.2% Offset MPa	(ksi)	MPa	(ksi)	MPa	(ksi)		
1-X	243	538	(78)	820	(119)	855	(124)	2.6	3.9
2-X	243	524	(76)	827	(120)	889	(129)	3.3	7.0
3-X	233	503	(73)	807	(117)	834	(121)	2.6	3.5
4-X	233	510	(74)	800	(116)	834	(121)	2.4	4.1
7-X	275	662	(96)	779	(113)	793	(115)	0.4	1.6
8-X	280	683	(99)	869	(126)	883	(128)	0.8	2.2
9-X	275	662	(96)	848	(123)	869	(126)	1.0	2.4
1-X.3	190	338	(49) Δ	676	(98)	717	(104)	5.2	6.3
4-X.3	185	338	(49) Δ	676	(98)	945	(137)	16.4	36.5
7-X.3	210	386	(56)	807	(117)	1000	(145)	8.9	22.2
9-X.3	2.5	400	(58)	800	(116)	1027	(149)	12.3	29.3

* 25.4 mm (1.0 in.) gage length.
 Δ Yield point displayed.

Table 19--Continued

Weld	BHN	Yield Strength		Ultimate Strength		True Fracture Strength		Percent Elongation*	Percent Reduction of Area
		0.2% Offset MPs	(ksi)	MPa	(ksi)	MPa	(ksi)		
1-X.4	190	372	(54)	724	(105)	820	(119)	9.4	15.3
4-X.4	190	359	(52)	696	(101)	793	(115)	9.0	15.8
7-X.4	220	648	(94)	827	(120)	917	(133)	4.2	10.1
2-X.1	205	400	(58) Δ	745	(108)	1020	(148)	14.8	35.0
3-X.1	200	386	(56) Δ	627	(91)	696	(101)	3.3	11.6
8-X.1	233	524	(76)	924	(134)	1048	(152)	8.7	18.0
2-X.5	228	448	(65)	731	(106)	786	(114)	3.3	7.4
3-X.5	220	455	(66)	793	(115)	1110	(161)	16.9	38.4
8-X.5	270	607	(88)	979	(142)	1096	(159)	5.9	11.6
9-X.5	270	607	(88)	952	(138)	1117	(162)	7.4	17.0

* 25.4 mm (1.0 in.) gage length.

Δ Yield point displayed.

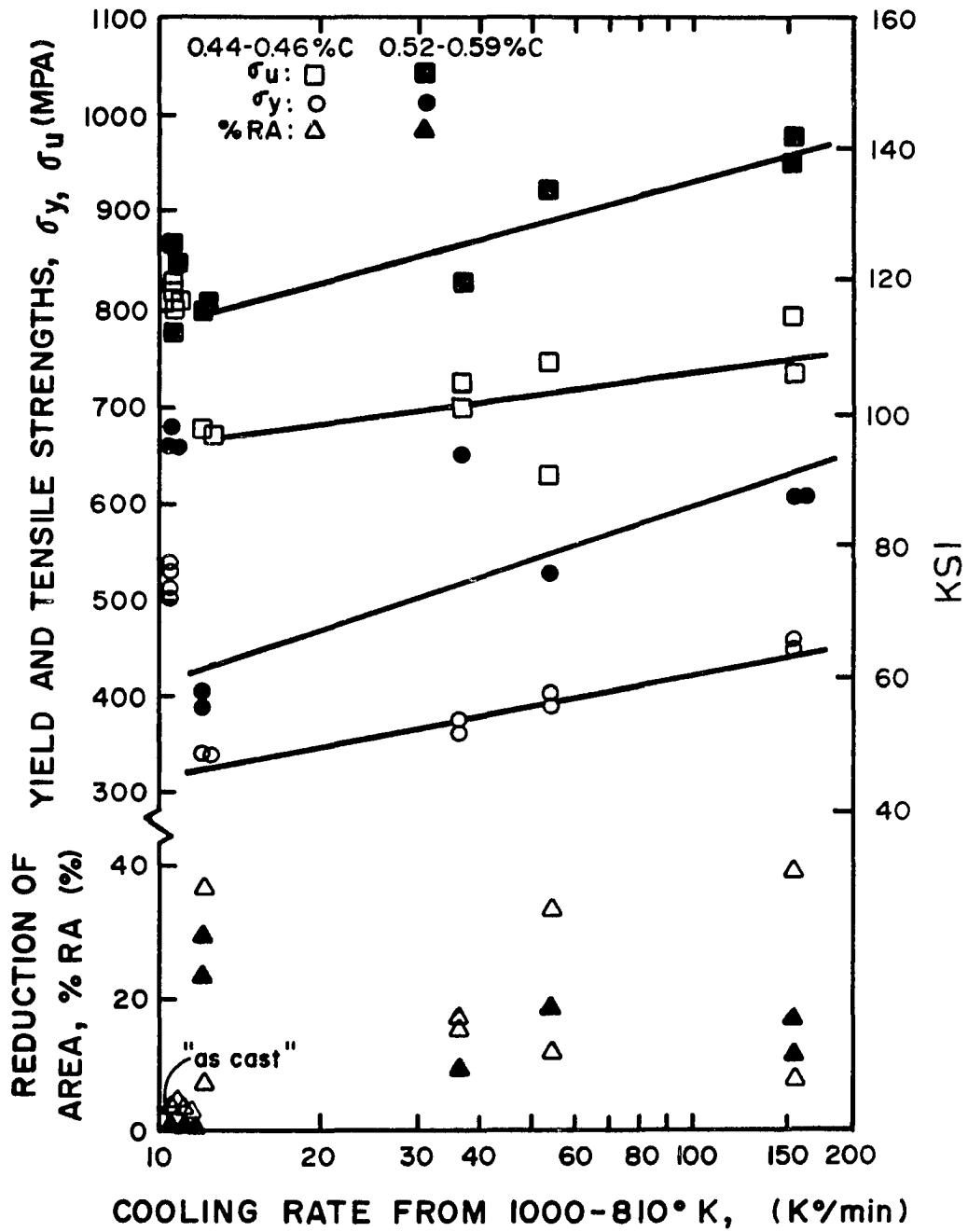


Figure 44: Tensile properties of plate weld metal in the as-cast and heat treated conditions.

percent vanadium could produce an additional increase of 30 MPa (4.4 ksi) or more.

In Figure 44, the effect of normalizing with various cooling rates through the transformation range on tensile properties is evident. For cooling rates of 37°K/min. and greater, the tensile properties of the weld metal with 0.52-0.59 wt. pct. carbon exceed those standard rail weld and approach the alloy rail weld levels with the important exception that the reduction of area exceeds ten percent. Thus, by proper control of composition and of cooling rate during normalizing heat treatment, thermite weld metal with strength comparable to the alloy rail welds but with significantly greater ductility can be produced.

Figures 45 and 46 give the tensile properties of weld metal for all rail welds and plate welds as a function of hardness. The lines in Figure 45 were established by linear regression (Appendix A) for the purposes of showing that (1) the as-cast properties of the rail welds and of the plate welds are clearly comparable, (2) by normalizing, adequate yield strength can be achieved in weld metal (provided composition is controlled) and (3) by normalizing, the ultimate strength is improved. Figure 46 clearly shows the major advantage gained by normalizing, that is, ductility can be improved significantly.

5.2.3 Fractography of Tensile Specimens. Representative tensile fractures are shown in Figures 47 and 48. The as-cast tensile specimens displayed fractures of essentially all cleavage, with traces of quasi-cleavage, regardless of composition, Figure 47; these fractures typify those observed for specimens removed from the weld metal of rail welds. By normalizing, fracture morphology ranged from all fibrous

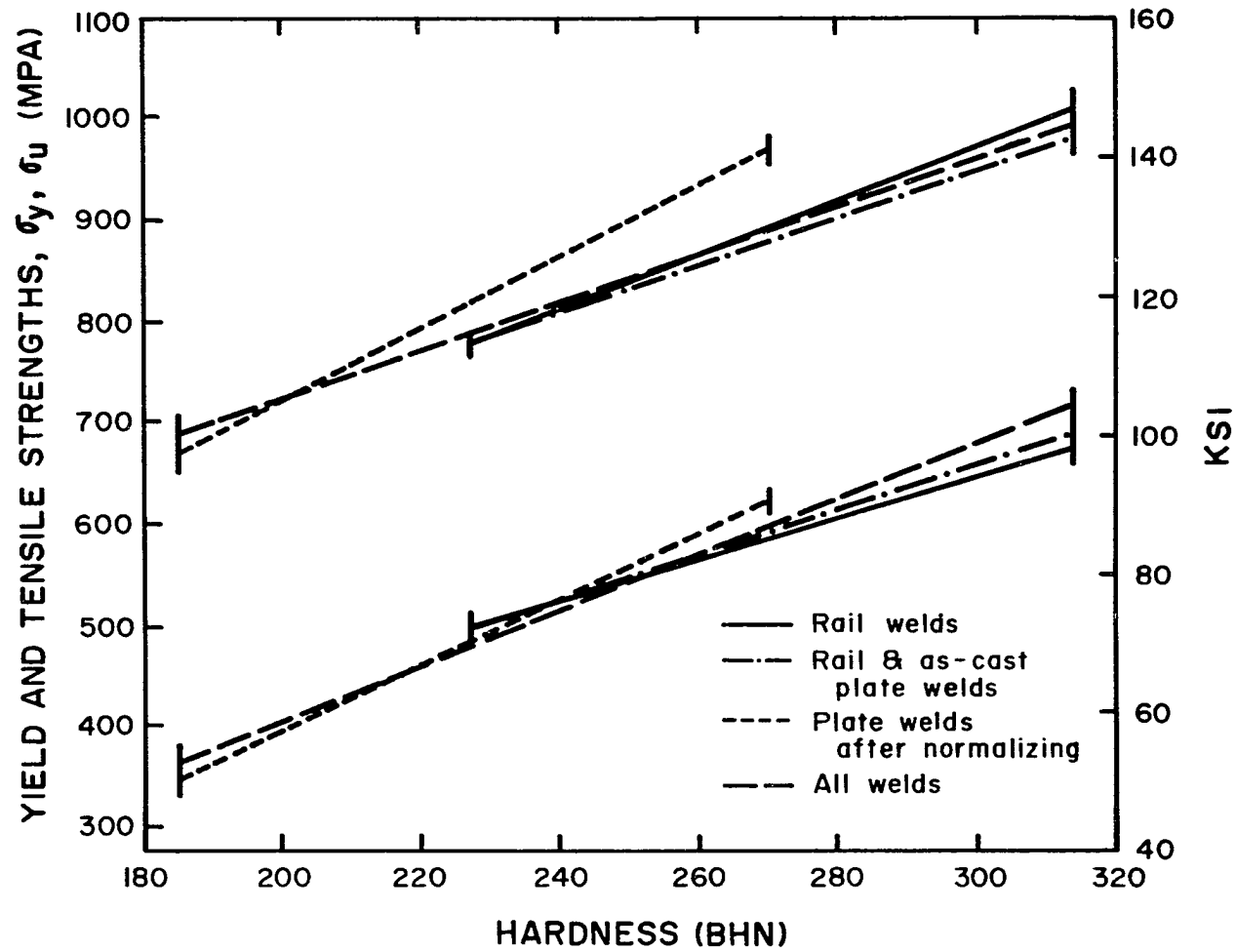


Figure 45: Tensile properties as a function of hardness for various groups of welds.

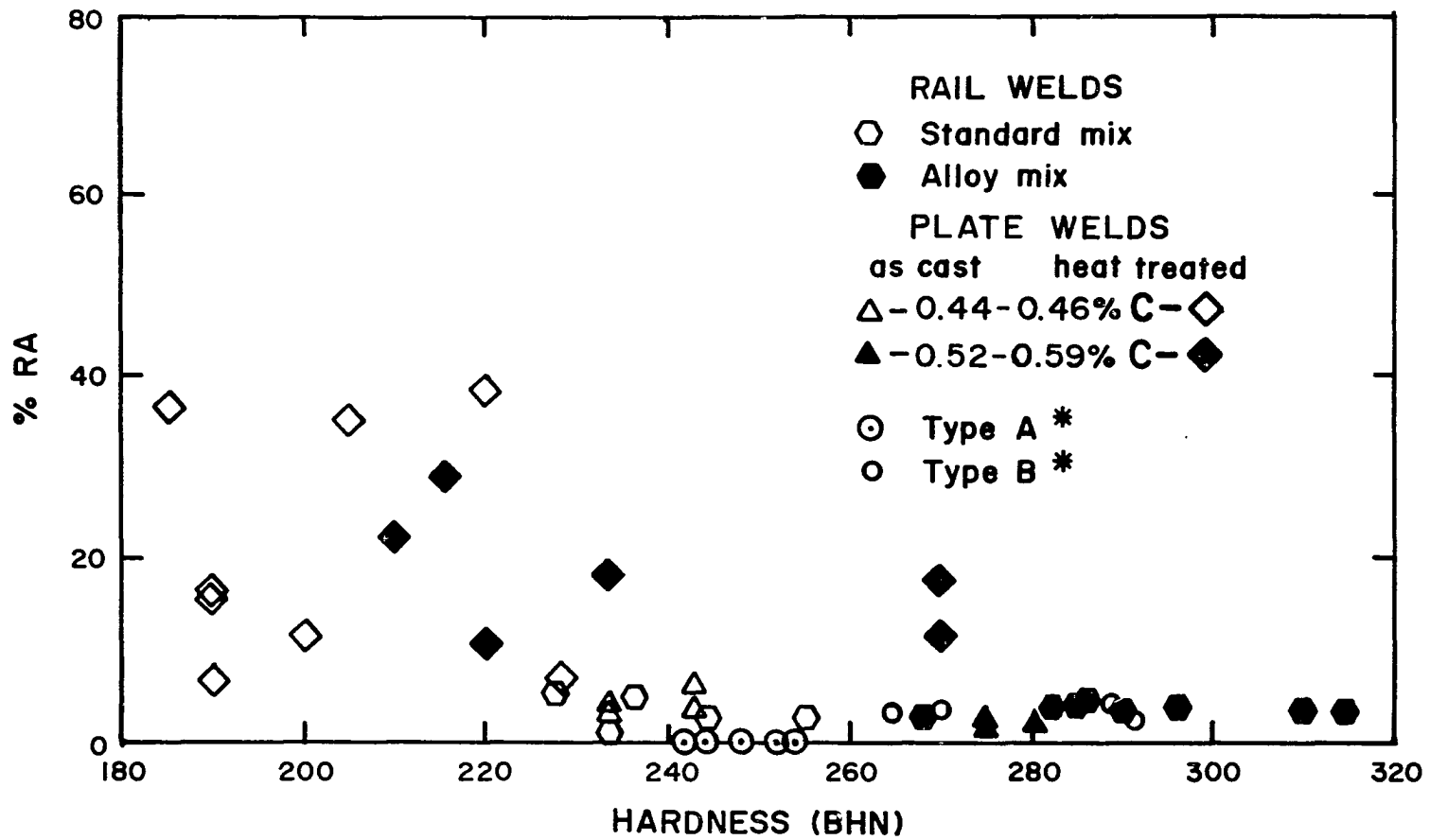
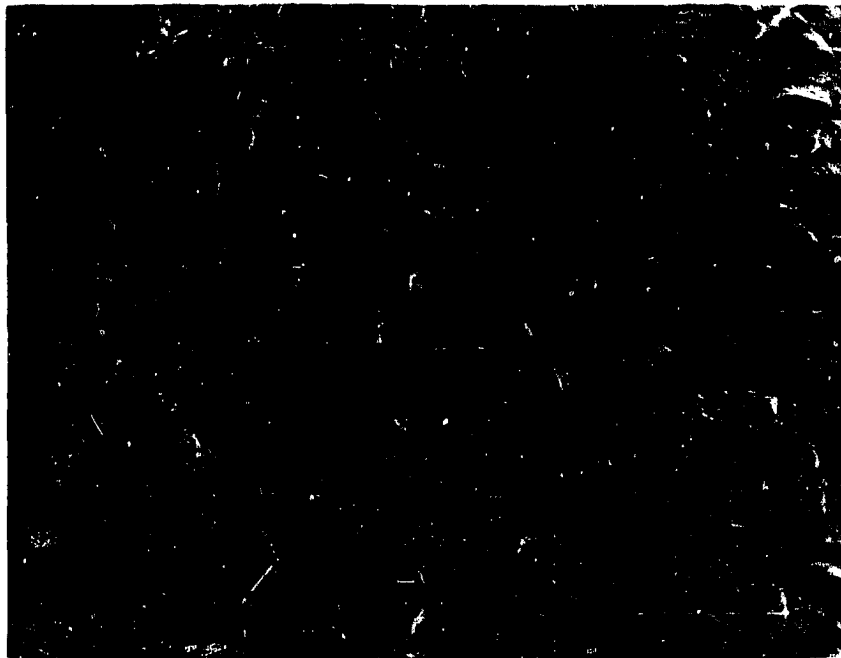
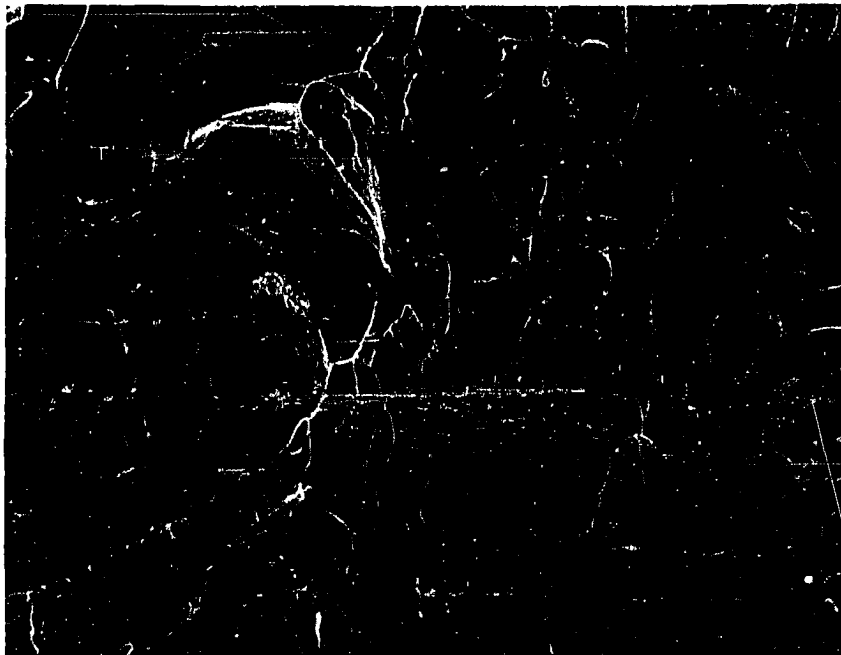


Figure 46: Reduction of area as a function of hardness for all welds. *From Ref. (24).

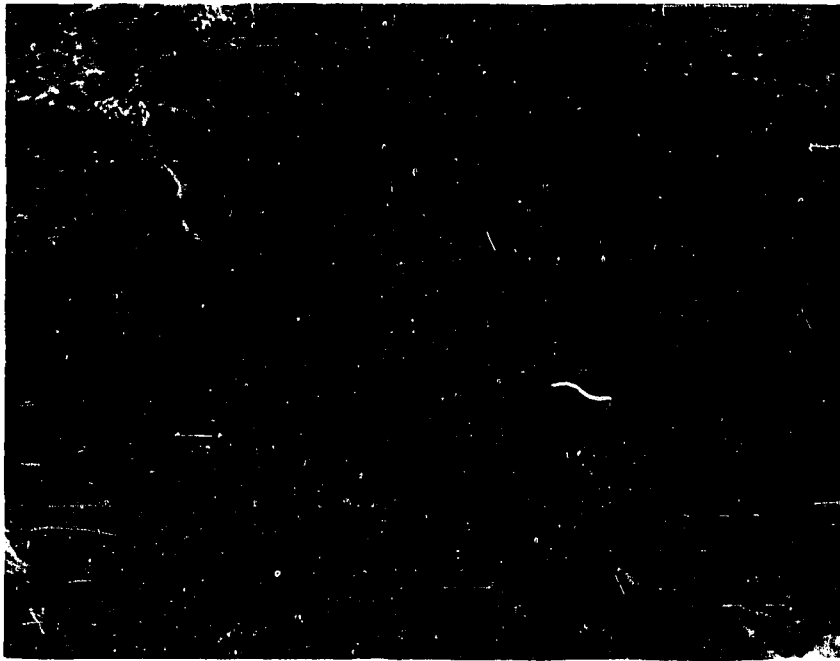


(a)

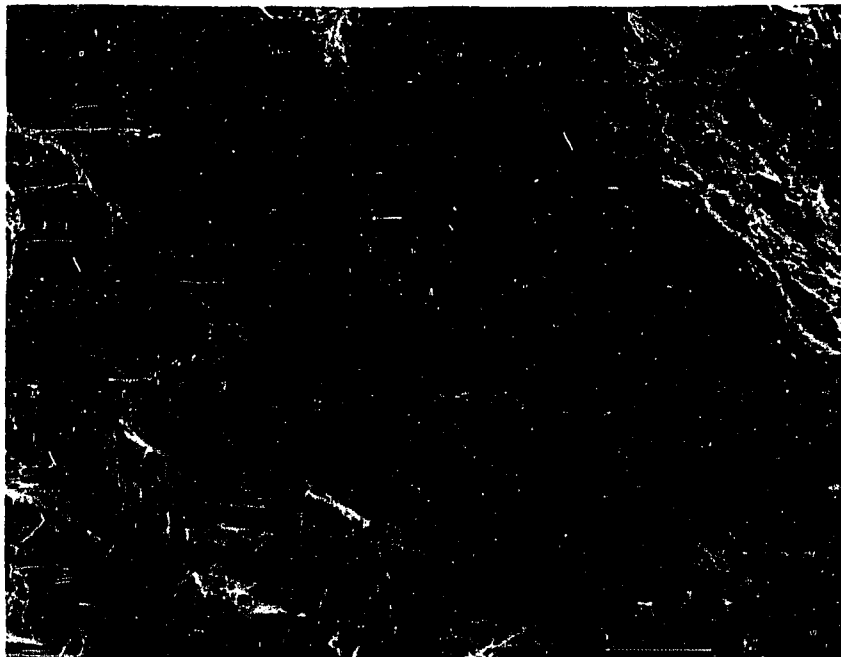


(b)

Figure 47: Fracture of the tensile specimen from weld 7-X. (a) 30X; (b) 310X.



(a)



(b)

Figure 48: Fracture of the heat treated weld tensile specimen 9-X.5.
(a) 23X; (b) 240X.

ductile fractures, for reduction of areas of over 20 percent, to mixed fractures of primarily fibrous with some cleavage for reduction of areas of 10-20 percent; these fractures can be seen in Figure 48. The ductility of the heat treated specimens is particularly sensitive to the effects of microporosity. In cases where reduction of area was less than ten percent for heat treated specimens, excessive microporosity was evident on the fracture surface.

5.3 Structural Analyses of the Plate Welds

5.3.1 Macrostructures. All of the macrostructures of the as-cast plate welds appeared essentially the same; a representative structure is shown in Figure 49. The effect of taper was evident as a slightly wider weld metal width at the bottom of welds with upward tapers. However, this was not a pronounced effect and appeared to have no effect on tensile properties. Porosity was evident along the centerline of most of the welds. Dendritic structure was similar to the rail welds; primary dendrite arms were essentially perpendicular to the fusion line. However, the dendrites were significantly finer in the plate welds, indicating a faster solidification rate.

5.3.2 Microstructures. Microstructures of the plate welds, both in the as-cast and heat treated states, are shown in Figures 50 to 53. Figure 50a typifies the as-cast structure of weld metal with 0.44-0.46 percent carbon (i.e., the "low-C" welds), and Figure 50b typifies the as-cast structure of weld metal with 0.52-0.59 percent carbon and 0.06 percent vanadium (i.e., the "C-V" welds). The "low-C" welds exhibit proeutectoid ferrite with Widmanstätten sideplates at the prior



Figure 49: Macrostructure of weld 4-X. 0.96X.



(a)



(b)

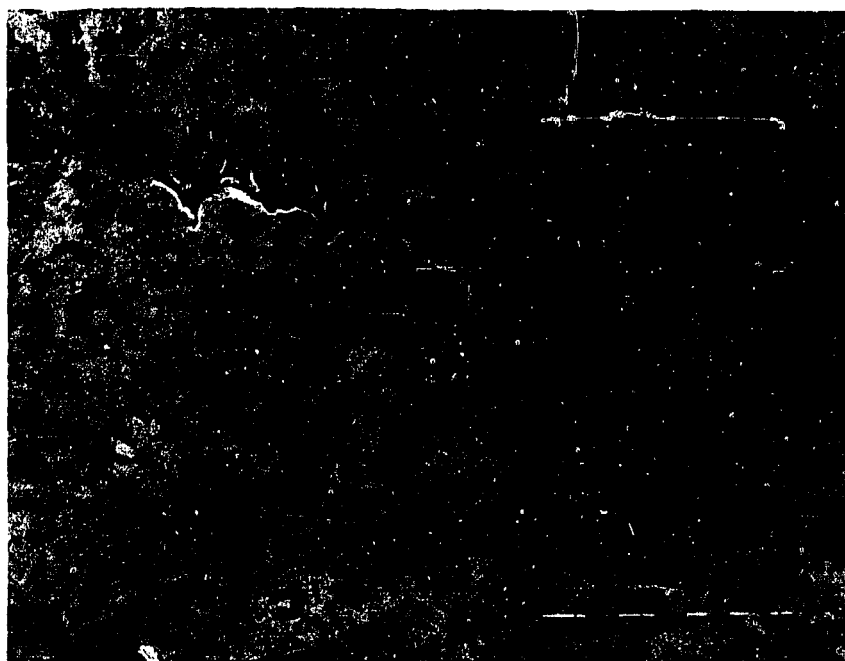
Figure 50: Proeutectoid ferrite in as-cast plate welds. (a) 1-X, 0.44 percent carbon; (b) 7-X, 0.59 percent carbon. 150X.

austenitic grain boundaries. On the other hand, there is less proeutectoid ferrite and no sideplates in the "C-V" welds, and these welds have many more islands of intragranular ferrite. In the rail welds, no ferrite sideplates were observed in any microstructures of weld metal. That they are present in the "low-C" plate welds indicates that these welds cooled faster than the rail welds.

Figure 51 shows the microstructure of weld metal after normalizing. When this figure is compared to Figure 50, it is obvious that the austenite grains have been refined. In the "low-C" welds, Figure 51a, there is about 15-20 volume percent of interconnected ferrite, whereas in the "C-V" welds there is less than 5 volume percent of islands of ferrite, Figure 51b. As expected, the refinement of the austenite grains is not affected by cooling rate; however, the amount of proeutectoid ferrite decreases noticeably from the slowest cooling rate, 12 K°/min, to the fastest, 154 K°/min.

The major constituents of the microstructures in the weld metal of plate welds are pearlite, transitional pearlite and bainite, which are also the major constituents observed in the rail welds. Figures 52 and 53 are examples of microstructures which show these constituents.

It was observed that the "C-V" welds contain more transitional pearlite and bainite than do the "low-C" welds, although no quantitative measurements were made to verify this observation. It was also seen in the normalized weld metal that the amounts of transitional pearlite and bainite increase with an increase in the cooling rate from the austenitizing temperature. The significant decrease in the amount of proeutectoid ferrite and the increase in the amount of transitional

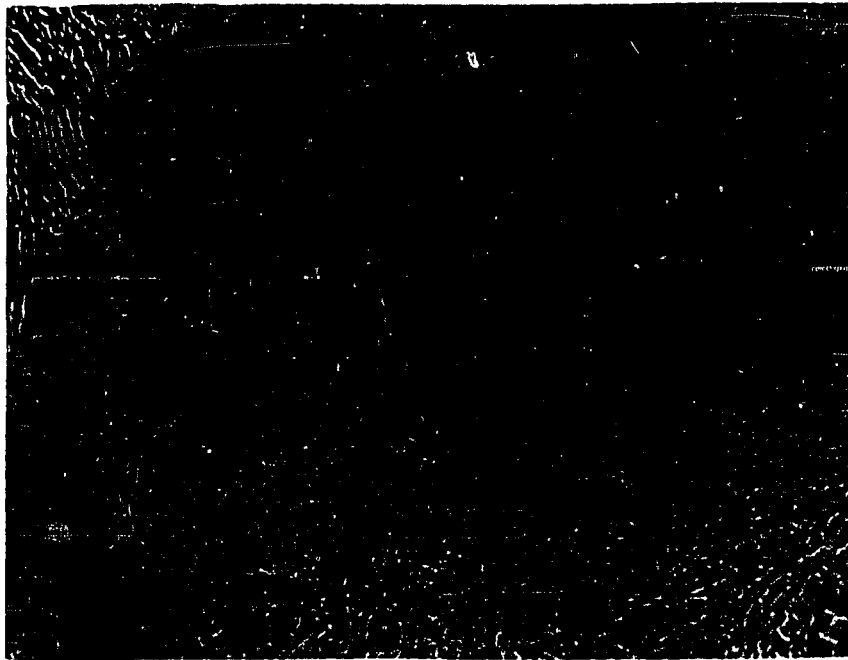


(a)



(b)

Figure 51: Effects of heat treatment on (a) 0.46 percent carbon weld, 4-X.4; (b) 0.59 percent carbon weld, 7-X.4. 150X.



(a)

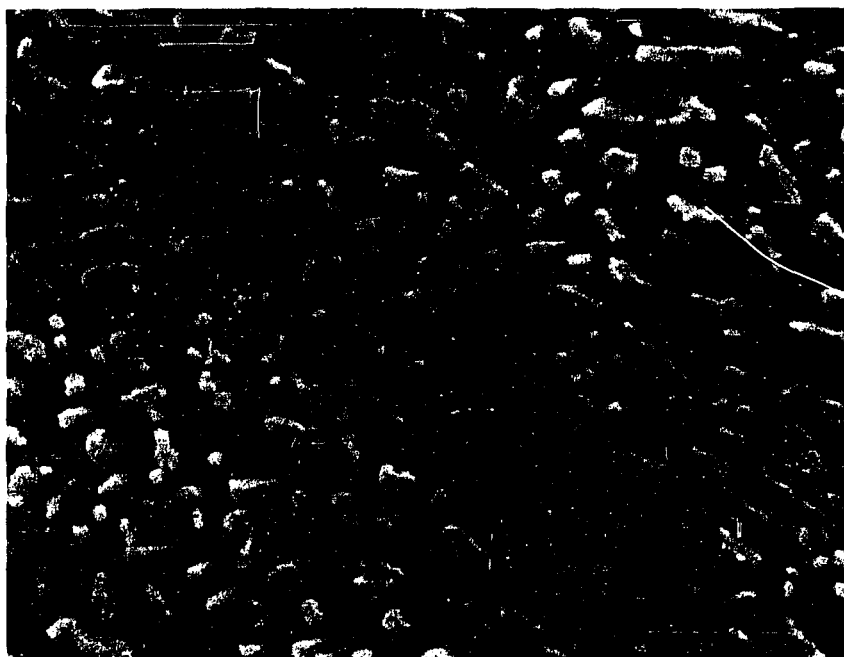


(b)

Figure 52: Pearlite and transitional pearlite in weld 9-X. (a) 4500X; (b) 22,000X.



(a)



(b)

Figure 53: Bainite in weld 3-X. (a) 4500X; (b) 22,000X.

pearlite and bainite accounts for, at least in part, the higher strength of the "C-V" welds and their desirable properties after an appropriate heat treatment.

CONCLUSIONS

Standard rails (i.e., AREA CC rails) and head-hardened rails can be welded to alloy rails (including Cr, CrV and CrMo rails) by the thermite process, using either "standard" kits or "alloy" kits for the weld metal. The welding process, however, produces changes in the mechanical properties among these metals; in addition, the properties of alloy weld metal and standard weld metal differ.

The effects of filtration of the weld metal, higher carbon content, the presence of microalloying elements and normalizing on the properties of the standard weld metal were studied through the experimental thermite plate welds. Appreciable ductility and acceptable strength levels can both be obtained by the judicious use of microalloying elements and a post-weld normalizing heat treatment. It also appears that filtration, if improved, can lead to an increase in weld metal ductility.

The following summarizes the important conclusions regarding the hardness, tensile properties, impact energies and structure of the thermite welds in rails and plates, along with additional conclusions drawn from thermal measurements and residual stress measurements from the rail welds.

1. Alloy weld metal is harder and stronger than standard weld metal. Specifically, the hardness of alloy weld metal is approximately 28-34 R_c , whereas the hardness of standard weld metal is in the range of 20-27 R_c , depending on preheat time. Correspondingly, the yield strength and tensile strength of alloy weld metal are

about 100-150 MPa (15-20 ksi) greater than those of standard weld metal.

2. With an increase in hardness of weld metal, there are corresponding increases in the tensile strength and yield strength, and the data exhibit a good correlation between hardness and strength. Coincidentally, as hardness increases, tensile ductility decreases.
3. Since alloy weld metal is stronger than standard weld metal, it is not as ductile. However, it is more important to note that weld metal of both types exhibits ductility in the range of only two to six percent.
4. The tensile fractures of the weld metal show transgranular cleavage when examined by SEM. Features observed in the fractures of standard weld metal, but not in alloy weld metal, are as-cast boundaries of columnar grains which separated very easily. Microporosity in small amounts was also seen in the tensile fractures along with microinclusions rich in Al_2O_3 with SiO_2 and MnS also present. Phase identification was not carried out, but is likely that the inclusions are aluminates, silicates, oxysulfides and sulfides.
5. The impact properties of weld metal are very low. Using Charpy V-notch (CVN) specimens, the energy absorbed is only 1.5-2.8 J (1.1-2.1 ft-lb_f) at 20°C. Within that range of energy absorbed, standard weld metal is slightly better than alloy weld metal.
6. The fractures of the CVN specimens, removed from weld metal, predictably indicate brittle failures. The appearance is

similar to published fractographs of rail steel with transgranular cleavage. Microporosity and inclusions are also apparent in amounts equivalent to those in the tensile fractures.

7. Longitudinal tensile specimens, which straddled the region of minimum hardness along the outer edge of the HAZ, were removed from the welds and tested. The yield strength of such specimens varies widely (from 460-820 MPa) due to the steep gradient of hardness at that location. The ultimate tensile strength is more predictable; it is 850-880 MPa for the standard and head-hardened rails and 890-960 MPa for the alloy rails.
8. The broken tensile bars revealed four types of fractures which correlated with the tensile ductility. As a group, CrMo rail is the most ductile with a reduction in area typically in the range of 40-60 percent. The minimum ductility of all of these specimens is 17 percent, and some of the other rail is as ductile but not with the same consistency shown by CrMo rail.
9. When standard or alloy rail is welded with a standard thermite kit, the minimum hardness of the HAZ and of the weld metal are comparable, but the tensile strength of the weld metal is less than that of the outer edge of the HAZ.
10. In the case of welding alloy rails with an alloy thermite kit, the minimum hardness in the HAZ is less than the minimum hardness of the weld metal; even so, the tensile strengths compare closely.
11. The impact properties of CVN specimens, which straddle the region of minimum hardness along the outer edge of the HAZ, are

very low. The energy absorbed for all specimens is only in the range of 2.6-6.9 J. Most of these specimens reveal some delamination of the rail.

12. The microstructures of the heat-affected zone and of the weld metal were studied in detail. As expected, the region of minimum hardness in the HAZ has a partially spheroidized structure. All of the remaining structures contain varying amounts of pearlite and transitional pearlite with small amounts of bainite sometimes noted. In most instances, of course, the hardest material is within the HAZ, and the microstructure shows transitional pearlite.
13. Collectively as a group, alloy rail and alloy weld metal show an increase in hardness with an increase in transitional pearlite plus bainite as constituents in the microstructure. The same behavior also holds for standard and head-hardened rail when classified with standard weld metal. However, the hardness of the former group is approximately 9 R_c points harder than the latter for equivalent amounts of transitional pearlite plus bainite. It is proposed that the factors responsible for the added hardness are ferrite strengthening associated with very fine alloy precipitates and the absence of proeutectoid ferrite in alloy weld metal.
14. Nonmetallic macroinclusions were observed in the weld metal of three welds when they were sectioned, ground and etched to reveal the macrostructures. Such inclusions were isolated and not seen in the tensile bars or CVN specimens used in this study.

15. The microinclusion content in weld metal is 0.24-0.49 percent. This volume fraction is high enough to be a contributory factor to the low values of tensile ductility of 2-6 percent reduction in area.
16. In four welds, temperatures in the rail were recorded during preheating and welding. These data show that preheat temperature is primarily a function of preheat time and of distance from the weld gap but not of location in the vertical cross-section of the rail. Preheat times of two and three minutes made no important differences in properties or structures of the heat-affected zones. The only effects observed were an increase in the width of the zone of weld metal and a slight decrease in the hardness and strength of weld metal.
17. During the cooling of some welds, a "clamshell" type muffle was wrapped around the weld for the purpose of decreasing the cooling rate. Depending upon the location in the HAZ, the muffle did increase the time in the critical range (1000°K-810°K) by 15-17 percent. The retardation of cooling did not significantly alter the properties of the welds except to reduce the maximum hardness in the HAZs of alloy rails by about 1-3 R_c points.
18. In one weld, temperatures in the weld metal were measured. The molten thermite steel poured into the mold at a temperature of at least 2140°K (3400°F) and perhaps higher. Solidification of the weld metal proceeded in the order of web, base and head. In the critical range (1000°K-810°K), the base and web cooled at

rates comparable to those of the HAZs and the head cooled more slowly than the HAZ.

19. One weld was left intact so that residual stresses could be measured. In the weld metal, the principal stresses are compressive (-270 MPa) in the head and base and slightly tensile (+60 MPa) in the web. Principal stresses in the HAZ are both compressive and tensile with some tensile stresses as high as +110 to +150 MPa in locations where the ultimate tensile strength is 855-1000 MPa. Such residual stresses, when added to the stresses due to flexural loading encountered in service, are very significant and could be expected to deleteriously affect fatigue life.
20. Filtration of the thermite steel for the plate welds was partially successful. Inclusion levels in the unfiltered welds were on the order of 0.36 volume percent, whereas for welds with multiple filters, the level decreased to an average of about 0.17 volume percent. Mean inclusion size and the statistical dispersion of the sizes of the inclusions also decreased. However, for filtration to have a noticeable effect on mechanical properties, namely ductility, inclusion content would have to be reduced to half this level or less.
21. The mechanical properties of the unfiltered and once filtered weld metal matched those of the standard rail welds, whereas the multiple filtered welds displayed a 30 percent increase in yield strength and hardness. Initially, this strength increase was attributed to filtration, but subsequent chemical analyses

of the weld metal showed that the stronger material had about 0.1 percent more carbon and 0.06 percent vanadium than the lower strength material. The microalloying effects of vanadium and the additional carbon account for the higher property levels.

22. By austenitizing the higher strength weld metal at 870°C and cooling through the transformation range at rates greater than 38 K°/min, strength levels which exceed those of the standard rail weld and rival those of the alloy can be produced with a significant increase in tensile ductility. After heat treating, the reduction of area lies in the range of 10-20 percent, as compared to only 2-6 percent observed in current production welds.
23. The undesirable low ductility and impact properties of the as-cast welds are associated with a pearlitic structure and a coarse prior austenitic grain size and, in the case of the standard welds, a significant amount of proeutectoid ferrite. This ferrite also contributes to the lower strength levels of the standard weld metal.

APPENDIX A

LINEAR REGRESSION EQUATIONS FOR FIGURES

Appendix A. Linear Regression Equations for Figures

Equation Form: $y = mx + b$

Figure No.	Comments	y	x	m	b	\bar{y}	s_y	Correlation Coefficient, ρ
12 and 45	Rail welds only, ln%RA excludes weld 7	δ_u (MPa)	BHN	2.7	169	894	84	0.94
		δ_y (MPa)	BHN	2.1	22	590	74	0.84
		ln%RA	lnBHN	-1.74	10.9	1.137	0.284	-0.65
45	Rail and plate welds (all)	δ_u (MPa)	BHN	2.4	259	835	100	0.86
		δ_y (MPa)	BHN	2.8	-144	530	112	0.90
		ln%RA	lnBHN	-4.48	26.4	1.816	0.974	-0.69
45	Rail and plate as-cast welds	δ_u (MPa)	BHN	2.3	263	872	76	0.83
		δ_y (MPa)	BHN	2.3	-15	588	74	0.84
		ln%RA	lnBHN	-1.58	9.95	1.111	0.380	-0.43

Appendix A--Continued

Figure No.	Comments	y	x	m	b	\bar{y}	s_y	Correlation Coefficient, ρ	
45	Heat treated plate welds	δ_u (MPa)	BHN	2.5	17	783	108	0.89	
		δ_y (MPa)	BHN	3.3	-261	448	106	0.84	
		1n%RA	1nBHN	-0.56	5.84	2.824	0.582	-0.12	
44	Plate welds: 0.44-0.46%C	δ_u (MPa)	1n δ	31.4	590	709	51	0.60	
		δ_y (MPa)	1n δ	44.9	217	387	45	0.97	
	Cooling rate: δ (K°/min). Does not include as-cast.	Plate welds: 0.52-0.59%C	δ_u (MPa)	1n δ	65.5	634	882	79	0.95
			δ_y (MPa)	1n δ	80.0	227	529	113	0.82

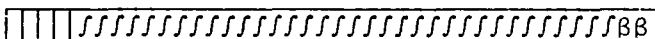
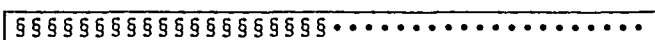
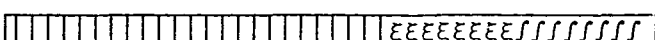
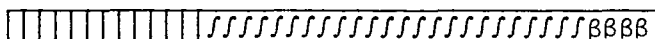
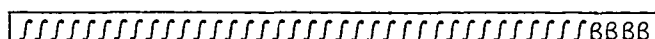
Appendix A--Continued

Figure No.	Comments	y	x	m	b	\bar{y}	s_y	Correlation Coefficient, ρ
Figure 28 and Appendix B	Rail welds: Standard rail and weld metal	R_C	(%)	0.06	22.6	25.9	3.2	0.58
	Alloy rail and weld metal	R_C	(%)	0.06	31.3	34.4	3.0	0.78
43	Plate welds: 0.44-0.46%C	R_C	δ	0.07	9.1	13.5	4.0	0.98
	Hardness vs Cooling rate							
	Plate welds 0.52-0.59%C	R_C	δ	0.08	15.9	21.5	5.3	0.99

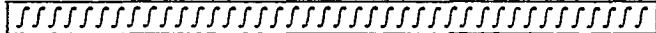
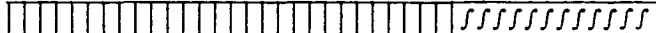
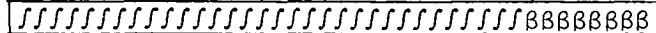
APPENDIX B

MICROSTRUCTURAL CHARACTERIZATION OF
THERMITE RAIL WELDS

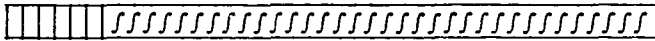
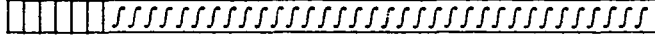
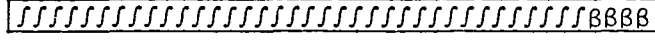
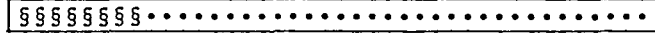
Appendix B. Microstructural Characterization of Thermite Rail Welds

Specimen (Weld No.- Rail Alloy)	Location wrt Weld Centerline (mm)	Microstructure* and Approximate Percentage	Average Hardness, R _C at Location	Interlamellar Spacing of Pearlite, d (μ)	Comments
1-A	0-20		34	0.12 < d < 0.21	Weld
	24		38	0.08 0.14	Fusion zone
	30-45		39	0.08	HAZ
	49-52		23		Outer edge HAZ
	70		34	0.08 0.12	Rail
1-B	0-20		33	0.12 0.19	Weld, SiO ₂ , Al ₂ O ₃ , MnS inclusions
	24		37	0.1 0.15	Fusion zone
	30-45		39		HAZ, MnS stringers

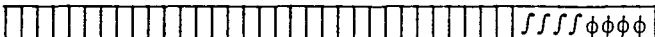
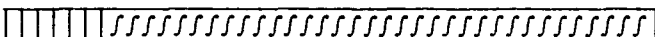
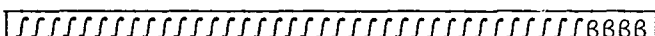
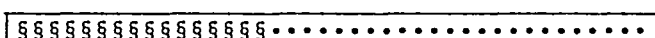
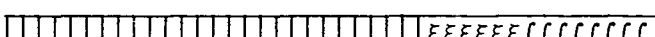
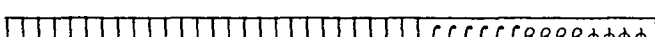
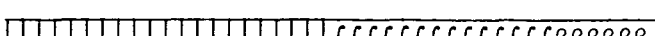
Appendix B--Continued Microstructural Characterization of Thermite Rail Welds

Specimen (Weld No.- Rail Alloy)	Location wrt Weld Centerline (mm)	Microstructure* and Approximate Percentage	Average Hardness, R _c at Location	Interlamellar Spacing of Pearlite, d (μ)	Comments
1-B	53-56		25		Outer edge HAZ
	70		34	0.08 < d < 0.17	Rail
2-A	0-15		31	0.14 0.17	Weld
	23-45		38		Fusion zone-23 mm and HAZ
	51-54		24		Outer edge HAZ
2-B	70		32	0.11 0.17	Rail
	0-20		32	0.17	Weld
	23-40		38		Fusion zone-23 mm and HAZ

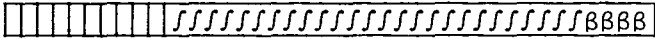
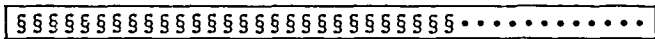
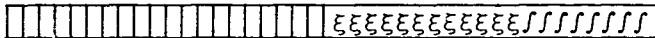
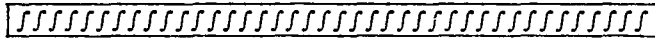
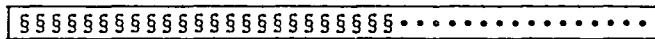
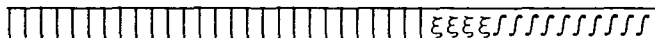
Appendix B--Continued Microstructural Characterization of Thermite Rail Welds

Specimen (Weld No.- Rail Alloy)	Location wrt Weld Centerline (mm)	Microstructure* and Approximate Percentage	Average Hardness, R _C at Location	Interlamellar Spacing of Pearlite, d (μ)	Comments
3-B	32		34	0.08	Fusion zone
	40-50		36	0.08	HAZ
	62-65		23		Outer edge HAZ
	75		33	0.13<d<0.21	Rail
4-A	0-20		22	0.11 0.19	Weld
	24		26	0.12	Fusion zone
	35-45		31		HAZ
	53-56		20		Outer edge HAZ

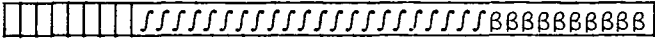
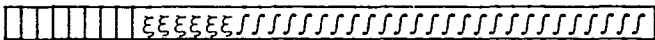
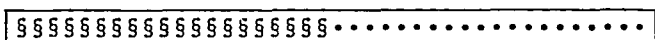
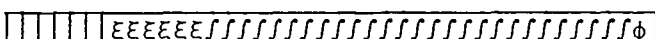
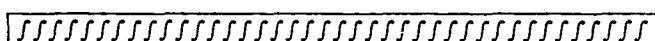
Appendix B--Continued Microstructural Characterization of Thermite Rail Welds

Specimen (Weld No.- Rail Alloy)	Location wrt Weld Centerline (mm)	Microstructure* and Approximate Percentage	Average Hardness, R _c at Location	Interlamellar Spacing of Pearlite, d (μ)	Comments	
4-A	65		25	0.21 < d < 0.3	Rail	
4-B	0-15		23	0.12	0.21	Weld
	20		27	0.12		Fusion zone
	30-40		39			HAZ
	51-54		23			Outer edge HAZ
	75		33	0.17	0.21	Rail
5-A	0-25		25	0.11	0.17	Weld
	28		27	0.09		Fusion zone

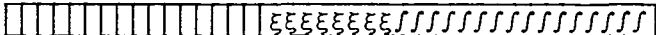
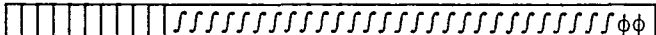
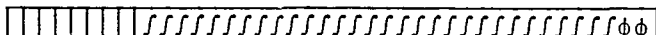
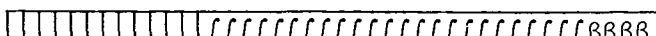
Appendix B--Continued Microstructural Characterization of Thermite Rail Welds

Specimen (Weld No.- Rail Alloy)	Location wrt Weld Centerline (mm)	Microstructure* and Approximate Percentage	Average Hardness, R _C at Location	Interlamellar Spacing of Pearlite, d (μ)	Comments
5-A	35-40		34	0.11 < d < 0.13	HAZ
	60-63		23		Outer edge HAZ
	75		28	0.13 0.19	Rail
5-B	0-20		25	0.11 0.22	Weld
	25		32		Fusion zone
	30-40		39		HAZ
	55-58		25		Outer edge HAZ
	75		32	0.1 0.13	Rail

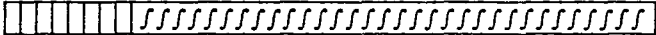
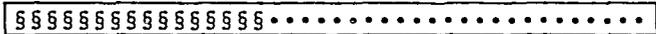
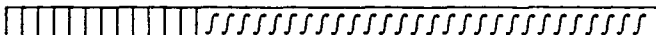
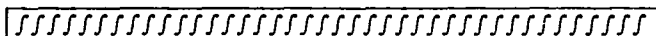
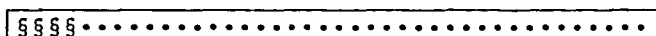
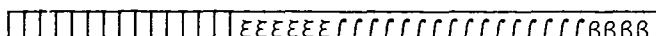
Appendix B--Continued Microstructural Characterization of Thermite Rail Welds

Specimen (Weld No.- Rail Alloy)	Location wrt Weld Centerline (mm)	Microstructure* and Approximate Percentage	Average Hardness, R _c at Location	Interlamellar Spacing of Pearlite, d (μ)	Comments	
7-B	24		25	0.14	Fusion zone	
	40-45		25	0.11 < d < 0.14	HAZ	
	61-64		20		Outer edge HAZ	
	75		29	0.08	Rail	
8-A	0-20		23	0.17	0.24	Weld
	24		26	0.09	Fusion zone	
	30-45		39		HAZ	
	54-57		23		Outer edge HAZ	

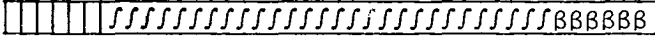
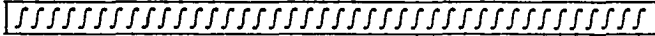
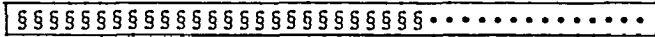
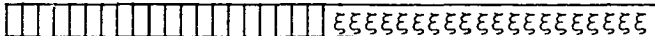
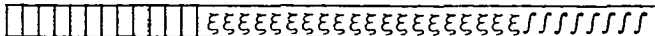
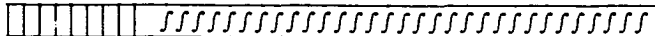
Appendix B--Continued Microstructural Characterization of Thermite Rail Welds

Specimen (Weld No.- Rail Alloy)	Location wrt Weld Centerline (mm)	Microstructure* and Approximate Percentage	Average Hardness, R _c at Location	Interlamellar Spacing of Pearlite, d (μ)	Comments
8-A	75		32	0.1 <d<0.17	Rail
8-B	0-20		26	0.13 0.19	Weld
	25		27	0.14 0.19	Fusion zone
	40-50		29	0.1 0.17	HAZ
	59-62		20		Outer edge HAZ
	75		30	0.09 0.12	Rail
9-A	0-25		30	0.12 0.24	Weld
	27		36	0.1 0.19	Fusion zone

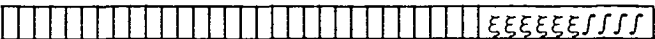
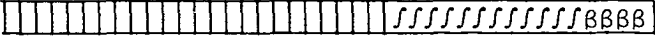
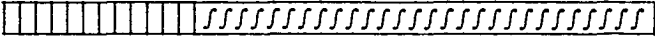
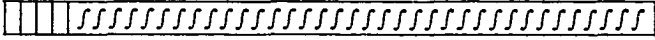
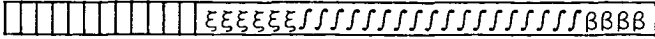
Appendix B--Continued Microstructural Characterization of Thermite Rail Welds

Specimen (Weld No.- Rail Alloy)	Location wrt Weld Centerline (mm)	Microstructure* and Approximate Percentage	Average Hardness, R _C at Location	Interlamellar Spacing of Pearlite, d (μ)	Comments
9-A	35-45		37	0.08 < d < 0.14	HAZ
	55-58		22		Outer edge HAZ
	75		33	0.11 0.19	Rail
9-B	0-25		30	0.12 0.24	Weld
	28		32	0.12 0.22	Fusion zone
	35-45		37		HAZ
	59-62		22		Outer edge HAZ
	75		32	0.14 0.24	Rail

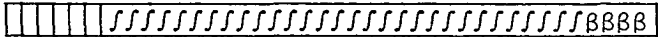
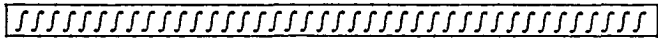
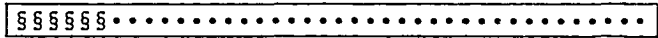
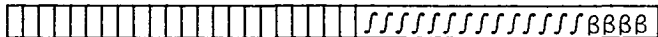
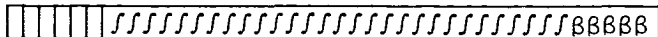
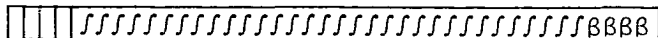
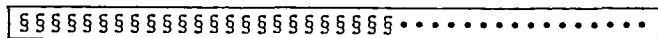
Appendix B--Continued Microstructural Characterization of Thermite Rail Welds

Specimen (Weld No.- Rail Alloy)	Location wrt Weld Centerline (mm)	Microstructure* and Approximate Percentage	Average Hardness, R _c at Location	Interlamellar Spacing of Pearlite, d (μ)	Comments
10-A	0-30		31	0.14 < d < 0.22	Weld
	37		36	0.09 0.14	Fusion zone, Al ₂ O ₃ , SiO ₂ of 420μ dia.
	40-55		39		HAZ
	64-67		26		Outer edge HAZ
	75		32	0.1 0.2	Rail
10-B	0-30		30	0.12 0.21	Weld
	37		35	0.08 0.12	Fusion zone
	45-55		39	0.08	HAZ

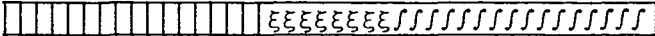
Appendix B--Continued Microstructural Characterization of Thermite Rail Welds

Specimen (Weld No.- Rail Alloy)	Location wrt Weld Centerline (mm)	Microstructure* and Approximate Percentage	Average Hardness, R _c at Location	Interlamellar Spacing of Pearlite, d (μ)	Comments
10-B	64-67		23		Outer edge HAZ
	75		33	0.14 < d < 0.21	Rail
12-A	0-20		33	0.12 0.19	Weld
	29		36	0.1 0.12	Fusion zone
	35-50		38	0.12	HAZ
	59-62		23		Outer edge HAZ
	75		33	0.12 0.21	Rail
13-A	0-20		34	0.14 0.22	Weld

Appendix B--Continued Microstructural Characterization of Thermite Rail Welds

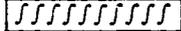
Specimen (Weld No.- Rail Alloy)	Location wrt Weld Centerline (mm)	Microstructure* and Approximate Percentage	Average Hardness, R _c at Location	Interlamellar Spacing of Pearlite, d (μ)	Comments
13-A	25		35	0.1	Fusion zone
	35-45		39		HAZ
	55-58		23		Outer edge HAZ
	70		33	0.12 < d < 0.22	Rail
14-B	0-25		32	0.13 0.21	Weld
	32		36	0.11	Fusion zone
	35-50		37	0.12	HAZ
	59-62		24		Outer edge HAZ

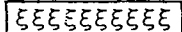
Appendix B--Continued Microstructural Characterization of Thermite Rail Welds

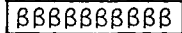
Specimen (Weld No.- Rail Alloy)	Location wrt Weld Centerline (mm)	Microstructure* and Approximate Percentage	Average Hardness, R _c at Location	Interlamellar Spacing of Pearlite, d (μ)	Comments
14-B	75		33	0.11<d<0.24	Rail

*

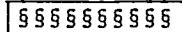
 -----Pearlite

 -----Transitional pearlite

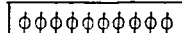
 -----Distorted pearlite

 -----Bainite

(Each symbol represents 2.5%)

 -----Degenerative pearlite

 -----Spheroidite

 -----Proeutectoid ferrite

REFERENCES

1. Mehra, O.K., D.K. Bose and C.K. Gupta, "Reduction of Calcium Molybdate", Metallurgical Transactions, Vol. 4, March 1973, pp. 691-694.
2. Applied Science in the Casting of Metals, K. Strauss, editor; Pergamon Press, Oxford, England, 1970, pp. 443-466.
3. Houldcroft, P.T., Welding Process Technology, Cambridge University Press, London, England, 1977, pp. 188-190.
4. Goldschmidt, H., "Neue Thermitreaktionen (New Thermite Reactions)", Zeitschrift fur Elektrochemie, Vol. 14, No. 35, 1908, pp. 558-564.
5. Hauser, D., "Methods for Joining of Rails: Survey Report", Report No. FRA/ORD-77/16, prepared for the U.S. Department of Transportation, July 1977.
6. Hauser, D., "Welding of Railroad Rails - A Literature and Industry Survey", ASTM Special Technical Publication STP 644, ASTM, Philadelphia, PA, 1978, pp. 118-141.
7. Myers, J., "Evaluation of Thermite-Type Railroad Rail Welds", M.S. Thesis, Department of Metallurgical Engineering, The University of Arizona, Tucson, Arizona, 1979.
8. Gupta, C.K., P.K. Jena, "Reduction of Molybdenum Trioxide by Aluminum", Journal of the Less Common Metals, Vol. 14, January 1968, pp. 148-150.
9. Belitskus, D., "Aluminothermic Production of Ferroalloys", Journal of Metals, Vol. 25, May 1973, pp. 39-44.
10. "High Temperature Reactions and Processes", Proceedings of the National Symposium, March 1976, Surathkal, India, pp. 89-97.
11. Ibid., pp. 217-222.
12. Belitkus, D., "Aluminothermic Production of Metals and Alloys", Journal of Metals, Vol. 24, January 1972, pp. 30-34.
13. Viswanath, R.P., B. Viswanathan, V. Srinivasan and M.V.C. Sastri, "A Differential Thermal Analysis Study of the Reduction of Ferric Oxide by Hydrogen", Indian Journal of Technology, Vol. 9, November 1971, pp. 439-440.

14. Welding Handbook, 7th edition, Vol. 1, American Welding Society, Miami, Florida, 1978, pp. 43-44.
15. Delachaux, P., "Soudage Aluminothermique de Pieces D'acier Moule et de Fonte (Aluminothermic Welding of Cast Steel and Cast Iron Parts)", Soud Techn Connexes, Vol. 25, No. 1, 2, January-February 1971, pp. 26-31.
16. Kubaschewski, O., and C.B. Alcock, Metallurgical Thermochemistry, 5th edition, Pergamon Press, Oxford, England, 1979, pp. 267-384.
17. The Making, Shaping and Treating of Steel, 9th edition, United States Steel Corporation, Pittsburg, PA, 1971, pp. 288-299.
18. JANAF Thermochemical Tables, 2nd edition, National Bureau of Standards, June 1971, Sections: Al_2O_3 , Fe.
19. Khalil, S.E., and M.W. Abdel-Salam, "Studies on Some Factors Affecting the Production of Extra Low-Carbon Ferrochrome from Baramiya Chromite Ore by Alumino-Thermic Process", Egyptian Journal of Chemistry, Vol. 15, No. 4, 1972, pp. 347-359.
20. Ashton, M.E., "Thermite Welding of Rail Steels", Railway Engineer, Vol. 2, No. 3, May-June 1977, pp. 40-45.
21. Sonon, D.E., J.V. Pellegrino and J.M. Wandrisco, "A Metallurgical Examination of Control-Cooled, Carbon-Steel Rails with Service Developed Defects", ASTM Special Technical Publication STP 644, ASTM, Philadelphia, PA, 1978, pp. 99-117.
22. Geiger, G., "Structure and Properties of Thermite Welds", Report No. TS-11958-1, prepared for the Transportation Systems Center, U.S. Department of Transportation, Cambridge, MA, February 1977.
23. Private Communication, Department of Technical Research and Development, A.T. & S.F. Ry. Co., 1001 N.E. Atchison St., Topeka, KS, 66616, 1981.
24. Myers, J., G.H. Geiger and D.R. Poirier, "Structure and Properties of Thermite Rail Welds", submitted for publication to AWS, 1980.
25. Ezhov, A.A., "The Development of Cracks in Welded Steel Castings of Unequal Thickness", Welding Production, Vol. 23, No. 10, October 1976, pp. 38-41.
26. Heller, W., and G. Beck, "Umwandlungsverhalten der Schienenstahle und Folgerungen fur das Schweißen und Brennschneiden (Transformation Characteristics of Rail Steels and Consequences for Welding and Flame Cutting)", Archiv fur das Eisenhüttenwesen, Vol. 39, No. 5, May 1968, pp. 375-386.

27. De Oliveira, E.Q., "Rail Specifications and Testing", M.S. Thesis, Department of Metallurgy, Sheffield University, Sheffield, England, September 1977.
28. Tetelman, A.S., "Fundamental Aspects of Fracture, with Reference to the Cracking of Weldments", Weld Imperfections, proceedings of a symposium at Lockheed Palo Alto Research Laboratory, Palo Alto, CA, September 19-21, 1966, Addison-Wesley, pp. 249-275.
29. Makara, A.M. and V.A. Sarihevskii, "Influence of Grain Boundary Fusion in the Heat-Affected Zone on the Susceptibility to Brittle Fracture of Welded Joints in Medium Alloy Steels", Automatic Welding, Vol. 27, No. 3, March 1974, pp. 1-5.
30. Borland, J.C., "Fundamentals of Solidification Cracking in Welds. Part 1", Welding and Metal Fabrication, Vol. 47, No. 1, January-February 1979, pp. 19-29.
31. Borland, J.C., "Ibid. Part 2", Welding and Metal Fabrication, Vol. 47, No. 2, March 1979, pp. 99-107.
32. Lebedev, B.D., "Effect of Solidification Rate on the Character of Distribution of Sulphur and Phosphorus in Welded Joints in Low Carbon Steels", Welding Production, Vol. 20, No. 11, November 1973, pp. 12-15.
33. Makarov, E.L., "Influence of Alloying Elements on the Resistance of High-Strength Weld Metal to Cold Cracking", Welding Production, Vol. 22, No. 4, April 1975, pp. 13-16.
34. Boniszewski, T., "Metallurgical Aspects of Reheat Cracking of Weldments in Ferritic Steels", proceedings of the Biennial Conference organized by the Heat Treatment Committee of the Iron and Steel Institute, December 8-9, 1971, London, I.S.I., 1972, pp. 29-41.
35. McPherson, R., "Research on Stress Relief Heat Treatment of Weldments", Australian Welding Journal, Vol. 18, No. 4 July-August 1974, pp. 25-29.
36. Joshi, A. and D.F. Stein, "Temper Embrittlement of Low Alloy Steels", ASTM Special Technical Publication STP 499, ASTM, Philadelphia, PA, 1972, pp. 59-89.
37. Marcus, H.L., L.H. Hackett, Jr. and P.W. Palmberg, "Effect of Solute Elements on Temper Embrittlement of Low Alloy Steels", Ibid., pp. 90-103.
38. Joshi, A., "Segregation at Selective Grain Boundaries and Its Role in Temper Embrittlement of Low Alloy Steels", Scripta Metallurgica, Vol. 9, 1975, pp. 251-260.

39. Kiessling, R. and N. Lange, Non-metallic Inclusions in Steel, 2nd edition, The Metals Society, London, England, 1978, pp. 74-100, Part III.
40. Farrar, J.C.M. and R.E. Dolby, Lamellar Tearing in Welded Steel Fabrication, The Welding Institute, Cambridge, England, 1972.
41. Aydincer, A. and V. Kondic, "Effect of Sulphide Inclusions on Impact and Tensile Properties of Cast Carbon-Steel", Foundry Trade Journal, Vol. 127, No. 2752, September 4, 1969, pp. 345-350.
42. Norring, K., H. Harvig and B. Lindwall, "Improvements in Thick-Plate Steel for Heavy Structures", Microalloying 75, proceedings of the 1975 Microalloying Conference, October 1-3, 1975, Washington D.C., Union Carbide Corporation, 1977, pp. 684-691.
43. Rittinger, J. and A. Fehervari, "The Influence of Microalloying Elements on the Toughness of Steels in Welded Structures", Microalloying 75, proceedings of the 1975 Microalloying Conference, October 1-3, 1975, Washington D.C., Union Carbide Corporation, 1977, pp. 593-598.
44. Sulfide Inclusions in Steel, J. de Barbadillo and E. Snape, editors; proceedings of an Internal Symposium, November 7-8, 1974, Port Chester, NY, ASM, Metals Park, OH, 1975, pp. 273-357.
45. Oono, Y., S. Yano and Y. Okamura, "Improvement in Steel Properties by Sulphide Shape Control", proceedings of the Welding Institute Conference on Trends in Steel and Consumables for Welding, November 13-16, 1978, London, The Welding Institute, Cambridge, England, 1979, pp. 55-68.
46. Hauser, J.J. and M.G.H. Wells, Inclusions in High-Strength Steels-Their Dependence on Processing Variables and Their Effect on Engineering Properties, Crucible Steel Corp., Pittsburg, PA, 1968.
47. Blake, P.D., "Oxygen in Steel Weld Metals", Metal Construction, Vol. 11, No. 3, March 1979, pp. 118-120.
48. Volchok, I.P., Yu.A. Shul'te and E.I. Pinchuk, "Role of Non-metallic Inclusions in the Failure of Cast Steel", Russian Castings Production, No. 9, September 1972, pp. 368-369.
49. Gladman, T., I.D. McIvor and F.B. Pickering, "Some Aspects of the Structure-Property Relationships in High-Carbon Ferrite-Pearlite Steels", Journal of the Iron and Steel Institute, December 1972, pp. 916-929.

50. Nolan, C.J., T.V. Brassard and R.F. Defries, "How Microstructure Influences Mechanical Properties of Forgings", Metals Engineering Quarterly, May 1973, pp. 30-34.
51. Krauss, G. Principles of Heat Treatment in Steel, American Society for Metals, Metals Park, OH, 1980, pp. 118-123.
52. Manning, R.D., H.M. Reichold and J.M. Hodge, "A Pearlite Hardenability Concept as a Basis for Alloy Development", Transformation and Hardenability in Steels, proceedings of a symposium sponsored by the Climax Molybdenum Company and the University of Michigan, February 27-28, 1967, pp. 169-175.
53. Leslie, W.C., The Physical Metallurgy of Steels, McGraw-Hill, New York, 1981, pp. 216-220.
54. Sato, T., "The Effect of Microstructure on the Fatigue and Impact Properties of Welded Zone in High Carbon Steels", Transactions of the Iron and Steel Institute of Japan, Vol. 21, No. 4, 1981, pp. 260-269.
55. Houin, J.P., A. Simon and G. Beck, "Relationship Between Structure and Mechanical Properties of Pearlite Between 0.2% and 0.8% C", Ibid., No. 10, 1981, pp. 726-731.
56. George, T.J., G. Bashford and J.K. MacDonald, "Grain-Size Control in Structural Steels", Journal of the Australian Institute of Metals, Vol. 16, No. 1, February 1971, pp. 36-48.
57. Pickering, F.B., "The Optimization of Microstructures in Steel and Their Relationship to Mechanical Properties", Hardenability Concepts with Applications to Steel, proceedings of a symposium sponsored by the Metallurgical Society of AIME, Chicago, IL, October 24-26, 1977, pp. 179-228.
58. Pickering, F.B., "The Effect of Composition and Microstructure on Ductility and Toughness", Toward Improved Ductility and Toughness, Climax Molybdenum Corp. Conference in Kyoto, Japan, October 25-26, 1971, pp. 9-31.
59. Giamei, A.F. and F.L. VerSnyder, "Control of Grain Boundaries for Structural Applications", Grain Boundaries in Engineering Materials, proceedings of the Fourth Bolton Landing Conference, June 9-12, 1974, Lake George, NY, Claitor's Publishing Division, Baton Rouge, LA, 1975, pp. 3-25.
60. Abrahamson, E.P., II, and V. Ramachandran, "Processing and Properties of Three Ultrafine Grain Alloy Systems", Ibid., pp. 139-148.

61. Smith, J.F., "Effect of Second-phase Particles on the Fracture Characteristics of Mild Steels", Effect of Second-phase Particles on the Mechanical Properties of Steel, proceedings of a conference by British Steel Corporation and the Iron and Steel Institute, March 24-25, 1971, ISI, London, England, 1971, pp. 37-43.
62. Knott, J.F., "Second-phase Particles and the Toughness of Structural Steels", Ibid., pp. 44-53.
63. Delage, L., A. Galibois and M.R. Krishnadev, "An In-depth Study of Grain Goundary Phenomena in the Temper Embrittling Process of a Ni-Cr Commercial Steel", Grain Boundaries in Engineering Materials proceedings of the Fourth Bolton Landing Conference, June 9-12, 1974, Lake George, NY, Claitor's Publishing Division, Baton Rouge, LA, 1975, pp. 561-572.
64. Lui, M.W. and I. LeMay, "Effects of Grain Boundary Carbids on the Fatigue Fracture of an AISI 4140 Steel", Ibid., pp. 397-408.
65. Abson, J., R.E. Dolby and P.H.M. Hart, "The Role of Non-metallic Inclusions in Ferrite Nucleation in Carbon Steel Weld Metals", proceedings of the Welding Institute Conference and Trends in Steel and Consumables for Welding, November 13-16, 1978, London, The Welding Institute, Cambridge, England, 1979, pp. 75-101.
66. Smith, J.E., A.P. Coldren and R.L. Cryderman, "Manganese-Molybdenum-Niobium Acicular Ferrite Steels with High Strength and Toughness", Toward Improved Ductility and Toughness, Climax Molybdenum Corp., Conference in Kyoto, Japan, October 25-26, 1971, pp. 119-142.
67. Baker, T.J. and R. Johnson, "Overheating and Fracture Toughness", Journal of the Iron and Steel Institute, November 1973. pp. 783-391.
68. Karitonov, A.S., Yu.N. Udovichenko and I.I. Zgur'ev, "Improving the Low-Temperature Toughness of Steel by Treatment with Sodium Chloride", Russian Castings Production, No. 8, August 1975, pp. 328-329.
69. Titarenka, V.A. and A.A. Shalomeev, "Low Carbon Steel for Castings of Superior Quality", Russian Castings Productions, No. 5, May 1975, pp. 206-207.
70. Aleksandrov, A.G., "The Effects of Calcium, Yttrium and Cerium on the Structure and Properties of Deposited Metal", Automatic Welding, Vol. 30, No. 1, January 1977, pp. 32-34.

71. Ershov, G.S., A.A. Kasatkin and I.K. Kalliopin, "Influences of Cooling Rate in the Molten State on Nitride Inclusion Sizes in Steel 35L and 38KhMYuAl Castings", Russian Castings Production, No. 5, May 1975, pp. 198.
72. Apelian, D. and R. Mutharasan, "Filtration: A Melt Refining Method", Drexel University, Philadelphia, PA, a paper submitted for publication in Journal of Metals, September or October, 1980.
73. Gray, T.G.F., J. Spence and R.H. North, Rational Welding Design, Butterworth and Co., London, England, 1975.
74. Hall, W.J., H. Khara, W. Soete and A.A. Wells, Brittle Fracture of Welded Plate, Prentice-Hall, Inc., Englewood Cliffs, NJ, 1967.
75. Kapadia, B.M. and E.J. Imhoff, Jr., "Fatigue-Crack Propagation in Electroslag Weldments", ASTM Special Technical Publication STP 631 ASTM, Philadelphia, PA, 1977, pp. 159-173.
76. Kapadia, B.M., "Influence of Residual Stresses on Fatigue Crack Propagation in Electroslag Welds", ASTM Special Technical Publication STP 648, ASTM, Philadelphia, PA, 1978, pp. 244-260.
77. Dohse, R., "Ermittlung von Eigenspannungen in Aluminothermisch Geschweissten Schienen (The Investigation of Residual Stresses in Alumino-Thermally Welded Rails)", Schweissen und Schneiden, Vol. 19, No. 10, October 1967, pp. 471-476.
78. Krauss, G., "Residual Stresses in the Weld Area of Head-hardened Rail", Colorado School of Mines, Golden, CO, a report prepared for the Transportation Systems Center, U.S. Department of Transportation, Cambridge, MA, April 21, 1980.
79. "General Instructions-Orgotherm Welding; Standard SOW, Quick Preheat SKV", Chemetron Railway Products, 111 E. Wacker Drive, Chicago, IL, 60601, 1976.
80. Steel, R.K., "A Perspectival Review of Rail Behavior at the Facility for Accelerated Service Testing", prepared for the 19th Annual Conference of Metallurgists, Halifax, Nova Scotia, August 24-28, 1980.
81. Manual for Railway Engineering, American Railway Engineering Association, Chapter 4, 1975.
82. Private communication, Chemetron Railway Products, 111 E. Wacker Drive, Chicago, IL, 60601, 1980.

83. "Measurement of Residual Stresses by the Blind Hole Drilling Method", Technical Data Bulletin T-403, Photolastic, Inc., Malvern, PA, 1977.
84. Steel Castings Handbook, P.F. Wieser, editor; Steel Founder's Society of America, 1980, pp. 21-17, 21-18.
85. Hertzberg, R.W., Deformation and Fracture Mechanics of Engineering Materials, John Wiley, New York, 1976, p. 334.
86. Park, Y.J. and I.M. Bernstein, "Mechanisms of Cleavage Fracture in Fully Pearlitic 1080 Rail Steel", ASTM Special Technical Publication STP 644, ASTM, Philadelphia, PA, 1978, pp. 287-302.
87. Metals Handbook, 8th edition, Vol. 9, American Society of Metals, Metals Park, OH, 1974.
88. Feddersen, C.E. and D. Broek, "Fatigue Crack Propagation in Rail Steels", ASTM Special Technical Publication STP 644, ASTM, Philadelphia, PA, 1978, pp. 414-429.
89. Smith, Y.E. and F.B. Fletcher, "Alloy Steels for High-Strength As-Rolled Rails", Ibid., pp. 212-232.
90. Meyer, P.L., Introductory Probability and Statistical Applications 2nd edition, Addison-Wesley, 1970, pp. 303-311.
91. Geiger, G.H. and D.R. Poirier, Transport Phenomena in Metallurgy, Addison-Wesley, Reading, MA, 1973, pp. 319-321.
92. Schneider, P.J., Conduction Heat Transfer, Addison-Wesley, Reading, MA, 1955, p. 266.